



Barium Titanate at the Nanoscale: Controlled Synthesis and Dielectric and Ferroelectric Properties

Journal:	<i>Chemical Society Reviews</i>
Manuscript ID	CS-SYN-07-2018-000583.R3
Article Type:	Review Article
Date Submitted by the Author:	20-Dec-2018
Complete List of Authors:	Jiang, Beibei; Georgia Institute of Technology, Materials Science and Engineering Iocozzia, James; Georgia Institute of Technology, Materials Science and Engineering Zhao, Lei; Georgia Institute of Technology, Materials Science and Engineering Zhang, Hefeng; Georgia Institute of Technology, Materials Science and Engineering Harn, Yeu-Wei; Georgia Institute of Technology, Materials Science and Engineering Chen, Yihuang; Georgia Institute of Technology, School of Materials Science and Engineering Lin, Zhiqun; Georgia Institute of Technology, Materials Science and Engineering

Barium Titanate at the Nanoscale: Controlled Synthesis and Dielectric and Ferroelectric Properties

Beibei Jiang, James Iocozzia, Lei Zhao, Hefeng Zhang, Yeu-Wei Harn, Yihuang Chen,
and Zhiqun Lin*

School of Materials Science and Engineering; Georgia Institute of Technology, Atlanta, GA
30332, USA

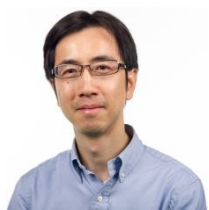
* To whom correspondence should be addressed. E-mail: zhiqun.lin@mse.gatech.edu

Keywords:

Barium titanate; nanostructures; ferroelectricity; size effects; surface effects; soft
chemical synthesis; organic-inorganic nanocomposites; functional polymers

Abstract

The current trend in the miniaturization of electronic devices has driven the investigation into many nanostructured materials. The ferroelectric material barium titanate (BaTiO_3) has garnered considerable attention over the past decade owing to its excellent dielectric and ferroelectric properties. This has led to significant progress in synthetic techniques that yield high quality BaTiO_3 nanocrystals (NCs) with well-defined morphologies (e.g., nanoparticles, nanorods, nanocubes and nanowires) and controlled crystal phases (e.g., cubic, tetragonal and multi-phase). The ability to produce nanoscale BaTiO_3 with controlled properties enables theoretical and experimental studies on the intriguing yet complex dielectric properties of individual BaTiO_3 NCs as well as BaTiO_3 /polymer nanocomposites. Compared with polymer-free individual BaTiO_3 NCs, BaTiO_3 /polymer nanocomposites possess several advantages. The polymeric component enables simple solution processibility, high breakdown strength and light weight for device scalability. The BaTiO_3 component enables a high dielectric constant. In this review, we highlight recent advances in the synthesis of high-quality BaTiO_3 NCs via a variety of chemical approaches including organometallic, solvothermal/hydrothermal, templating, molten salt, and sol-gel methods. We also summarize the dielectric and ferroelectric properties of individual BaTiO_3 NCs and devices based on BaTiO_3 NCs via theoretical modeling and experimental piezoresponse force microscopy (PFM) studies. In addition, viable synthetic strategies for novel BaTiO_3 /polymer nanocomposites and their structure-composition-performance relationship are discussed. Lastly, a perspective on the future direction of nanostructured BaTiO_3 -based materials is presented.

Bios of all authors

Zhiquan Lin is a Professor in the School of Materials Science and Engineering at the Georgia Institute of Technology. He received his Ph.D. in Polymer Science and Engineering from the University of Massachusetts, Amherst in 2002. His research interests include polymer-based nanocomposites, block copolymers, polymer blends, conjugated polymers, quantum dots (rods, tetrapods and wires), functional nanocrystals (metallic, magnetic, semiconducting, ferroelectric, multiferroic, upconversion and thermoelectric) of different architectures (plain, core/shell, hollow and Janus), solar cells, LEDs, batteries, photocatalysis, electrocatalysis, thermoelectrics, hierarchically structured and assembled materials, and surface and interfacial properties.



Dr. Beibei Jiang received her Ph.D. in Materials Science and Engineering from the Georgia Institute of Technology in December 2016 under the guidance of Professor Zhiquan Lin. Her dissertation research at Georgia Tech is focused on designing polymer-enabled functional polymer-inorganic nanocomposites for improving the performance of Li-ion batteries, capacitors, and ferroelectric devices. Her research interest is focused on analyzing the failure mechanisms of various types of devices including Li-ion batteries, capacitors and thin film transistors as well as designing and synthesizing new materials and new structures for improving the stability of material structure, interface, and overall device

structure. These efforts aim to improve the overall performance and prevent the failure of energy devices.



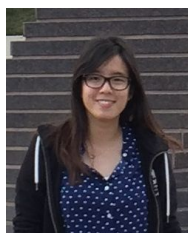
Dr. James Icozzia received his Ph.D in Materials Science and Engineering from the Georgia Institute of Technology in August 2018 under the guidance of Professor Zhiqun Lin. His research interests include nanocomposites, block copolymers and hyperbranched polymer systems for the development of functional hard and soft organic/inorganic nanomaterials in the areas of drug delivery, electronics, energy and stimuli-responsive materials. James has author or co-authored more than 30 papers in the fields of polymers and energy materials.



Dr. Lei Zhao is a senior scientist in Baker Hughes, Inc., specialized in advanced composite materials for oil and gas industry application. He holds a PhD degree in material science and engineering from Iowa State University. Lei has published over 20 papers on material science journals in area of polymer science and nanostructured material, and filed 20 patents on carbon composite material and metallic composite used in downhole seal and joining. Before joining Baker Hughes in 2013, he worked in Argonne National laboratory as post-doc in developing metallic nanocomposite materials for next generation electric vehicles.



Dr. Hefeng Zhang received his Ph.D in Polymer Chemistry and Physics under the supervision of Professor Junpo He at Fudan University in 2012 where he worked on the precision synthesis and characterization of non-linear polymers. He pursued postdoctoral work on polyethylene molecular engineering under direction of Professor Nikos Hadjichristidis at King Abdullah University of Science and Technology (2012-2015) and uniform nanomaterial synthesis under the guidance of Professor Zhiqun Lin at the Georgia Institute of Technology (2015 – 2016). In 2017, Hefeng Zhang joined Shantou University as a professor. His research interests include well-defined complex polymer synthesis, inorganic nanomaterial-polymer hybrid fabrication, natural polymer modification and organocatalysis.



Yeu-Wei Harn received her bachelor's degree in a double specialty program of Management and Technology with double specialties in materials science and engineering as well as quantitative finance in 2013 and her master degree in materials science and engineering in 2015, both from the National Tsing Hua University, Taiwan. She joined the Georgia Institute of Technology to pursue her Ph.D in materials science and is currently working as a graduate researcher under Professor Zhiqun Lin. Her work focuses on using soft star-like block copolymers as templates to synthesize nanoparticles and the subsequent investigation of their properties.



Dr. Yihuang Chen is a postdoctoral fellow in Professor Zhiqun Lin's group at the Georgia Institute of Technology. He received his Ph.D in Materials Science and Engineering from the South China University of Technology in 2017. Previously, he was a visiting graduate student in Professor Zhiqun Lin's group from 2014. His research interests center on the synthesis of responsive polymers, functional polymer brushes and polymer/inorganic nanocrystal hybrids.

1. Introduction

Owing to its excellent dielectric and ferroelectric properties, BaTiO₃ is one of the most extensively studied ferroelectric materials and is currently utilized in a wide variety of fields including multilayer capacitors,¹⁻³ transducers,⁴⁻⁸, actuators,⁸⁻¹⁰ electro-optical devices,¹¹⁻¹³ electromechanical devices,¹⁴⁻¹⁷ dynamic random-access memory,¹⁸⁻²¹ field-effect transistors,²²⁻²⁵ and thermistors,²⁶⁻²⁹ among others. Since the discovery of BaTiO₃ ferroelectricity by Wul and Goldman in 1945, the bulk physical properties and crystal structure of BaTiO₃ have been intensely investigated.³⁰⁻³³ Bulk BaTiO₃ primarily exists in four crystal phases including cubic, tetragonal, orthorhombic, and rhombohedral (**Figure 1**).³⁰ At high temperatures ($T > 120$ °C), it possesses the classic perovskite structure (*i.e.*, cubic phase), in which Ba²⁺ and O²⁻ ions together form the FCC lattice while the smaller Ti⁴⁺ cation resides in the octahedral interstitial sites, forming [TiO₆] in the FCC array. Such cubic phase structure is highly symmetric with the cation and anion centers coincide with each other, leading to no polarization in the crystal structure and thus no ferroelectricity (*i.e.*, paraelectric). When T is lowered to below 120 °C, the cubic symmetric structure turns to nonsymmetric structure, accompanied with the deviation of the cation center from the anion center, resulting in a net spontaneous polarization in the crystal structure and the transition from paraelectric to ferroelectric phase (**Figure 1**). When T is between 120 °C and 5 °C, BaTiO₃ exhibits the tetragonal structure where Ti⁴⁺ cation deviates from the center of [TiO₆] octahedron, leading to a net polarization along the [001] edge direction due to the displacement of the cation center from the anion center. With further cooling to between 5 °C and -90 °C, the structure transits to the orthorhombic phase, which can be regarded as the elongation of the cubic unit cell along the [011] face diagonal direction. Lastly, onset of the rhombohedral phase occurs at $T < -90$ °C, which corresponds to the elongation of the cubic unit cell along the [111] body diagonal direction. Distortions along these directions result in nonsymmetry in the crystal structure with the cation center deviating from the anion center, leading to ferroelectric phases with a

net spontaneous polarization. Research on nanoscopic ferroelectric BaTiO₃ synthesis and property investigation has received much attention. The ability to manipulate the properties of nanostructured ferroelectric materials is essential to developing molecular electronics such as random access memory³⁴ and logic circuitry.^{35, 36} Similar to many well-established nanocrystals (NCs) systems (e.g., quantum dots,³⁷⁻⁴⁰ and magnetic NCs⁴¹⁻⁴³), BaTiO₃ NCs behave differently from both their bulk counterparts and their dielectric and ferroelectric properties exhibit heavy dependency on the crystal size (*i.e.*, size effect).⁴⁴⁻⁴⁷ Owing to the rapid progress in advanced synthetic techniques for producing myriad high-quality NCs with controllable structures and dimension, both theoretical and experimental studies are made possible for studying the effect of structure and dimension on dielectric and ferroelectric properties. To date, a diverse group of BaTiO₃ nanostructures (e.g., nanodots,^{48, 49} nanoparticles,⁵⁰ nanobowls,⁵¹ nanorods,⁵² nanocubes,⁵³ and nanowires⁵⁴) with different crystalline phases (*e.g.*, cubic,^{55, 56} tetragonal,²⁸ or multi-crystalline⁵⁷) have been produced through various chemical approaches (*e.g.* organo-metallic,^{49, 54} solvothermal/hydrothermal,^{48, 51-53} templating,⁵⁵⁻⁵⁷ molten salt,^{55, 58} and sol-gel methods^{59, 60}). In addition, a lot of developments have been made in the exploration of the effects of the size, shape, microstructure, and surface conditions (*e.g.* surface defects and capping ligands) of BaTiO₃ NCs on their dielectric and ferroelectric properties with the utilization of many advanced characterization methods such as piezoresponse force microscopy (PFM),⁶¹⁻⁶³ neutron scattering,⁶⁴⁻⁶⁷ and electron microscopy.⁶⁸⁻⁷¹ To further elucidate the underlying mechanism of the dielectric and ferroelectric behavior of BaTiO₃ at the nanoscale, several models have been proposed.⁷²⁻⁷⁴ Moreover, the practical application of BaTiO₃/polymer nanocomposites requires that the BaTiO₃ NCs can be homogeneously dispersed within the polymer matrix without phase separation or particle agglomeration. This has triggered recent significant research efforts into the development of surface modification techniques that enable high-

quality BaTiO₃/polymer nanocomposites with uniform dispersion and favorable morphology as compared to traditional simple mixing approaches.

This review aims to summarize the recent achievements in the following aspects of BaTiO₃ nanomaterial research: chemical synthesis of individual BaTiO₃ NCs, ferroelectric properties of individual BaTiO₃ NCs by PFM characterization, BaTiO₃ thin film preparation and characterization, BaTiO₃-based organic/inorganic nanocomposites and their dielectric performance. Within each part, a representative sampling of examples are provided to illustrate (1) BaTiO₃ NCs with well-defined morphologies and chemical compositions enabled by controlled synthesis; (2) the structure-property relationship (*i.e.*, how the crystal structure, shape, and processing history affect the dielectric and ferroelectric properties); (3) chemical strategies to disperse BaTiO₃ NCs in polymer matrices for use in electronic devices. An outlook on how to further optimize the morphology of BaTiO₃ NCs and improve the dielectric performance of BaTiO₃ NCs and BaTiO₃/polymer nanocomposites is also presented.

2. The Structure-Property Relationship of Nanoscale BaTiO₃

A reduction of system size into the nanoscale regime typically enhances the effect of microstructure, composition, stress, defect concentration and surface composition on the type and intensity of ferroelectric dipoles. This is due primarily to the fact that these dipoles have a length scale of only a few angstroms (*i.e.*, the separation distance between the positive and negative charges of an elementary dipole), leading to unique dielectric and ferroelectric properties in BaTiO₃ NCs.^{28, 75, 76} In this context, understanding and ultimately manipulating the dielectric properties through structure or phase design at the nanoscale is of prime importance for the practical application of this interesting material in various types of next generation micro and nano devices that rely on dielectric materials. Various strategies for obtaining desirable dielectric properties have been investigated. Among them, changing the

size, shape and surface modification of BaTiO₃ NCs stand out as the most effective and widely studied strategies. Strategies of these types are the focus of this section.

2.1 BaTiO₃ Nanocrystals of Different Shapes

BaTiO₃ nanostructures have attracted much attention because of their dielectric and ferroelectric properties can be modified by controlling their size and shape.⁷⁷ Among them, isotropic zero-dimensional (0D) BaTiO₃ nanoparticles of different sizes stands out as the most common form for practical applications because of the simplicity in their synthesis. In the case of one-dimensional BaTiO₃ (1D) nanostructures, there exist some difficulties in achieving simultaneous control for both their nanostructures and compositions because of the complexity in achieving stoichiometric ternary compound.⁷⁸⁻⁸⁰ However, 1D BaTiO₃ nanostructures exhibit unique dielectric and ferroelectric properties attributed by their confinement in the radical direction, which win them wide research interest.⁸¹⁻⁸⁵ In addition, 1D BaTiO₃ nanostructures, which retain wire-like connectivity promising for efficient transport of electrons and photons, are promising building blocks for realizing miniaturizing devices.^{54, 86, 87}

2.2 Size and Shape Effects

Size effects of the dielectric properties indicate a strong correlation between particle size and dielectric properties. As particle size decreases in the micrometer range, dielectric constant first increases significantly, reaching to a maximum value (~6000) at some particle size, and finally decreases when further decreasing particle size to below the micrometer range, as shown in **Figure 2a**.^{88,89} The particle size, where dielectric constant reaches maximum, depends heavily on the synthesis methods and process histories. For example, maximum dielectric constant (ϵ') of 6079 were achieved for BaTiO₃ ceramics prepared by two-step sintering method with the particle size of approximately 1 μm .⁹⁰ Another change

accompanying the grain/particle size decrease is a reduction in the Curie temperature (T_C), which is the transition temperature between tetragonal and cubic phases (**Figure 2b**). As a result, the room-temperature tetragonal distortion and hence ferroelectricity is gradually reduced with decreasing particle size. The critical size below which the room-temperature ferroelectricity of BaTiO₃ nanoparticles disappears varies greatly with the synthesis methods and is normally in the range of 10-100 nm.⁴⁶ Other factors, such as microstructure, composition, stress, defect concentration and interfacial effects, can also affect the critical size of ferroelectricity in BaTiO₃ nanocrystals.^{44-47, 91} However, many of these factors are likely interrelated with each other, which make it difficult to isolate their individual effects or separate with the intrinsic size effect. As a result, various models have been developed to explain the size effect,^{92, 93} though no agreement on accepted models exists. The only widely accepted point is that the size effect not only originates from the intrinsic atomic-scale polarization, but is also determined by the extrinsic nature of the material which is strongly related to processing history and the crystallinity of the NCs.⁴⁶ As most of these models are reviewed extensively in other literature,⁹⁴⁻⁹⁶ here we focus primarily on the most recent and popular model, the “*core-shell*” model, with the goal of providing a clear illustration on the complex ferroelectric phase transition and dielectric properties which will be covered in the Materials Synthesis (Section 3) and Single-crystal Characterization (Section 4) parts. This model, evidenced by various structure characterization techniques, was initially proposed by Tsurumi *et al.*,^{75, 76} and is found to match well to the experimentally observed dielectric properties.

This model divides the BaTiO₃ particle into three regions: an inner core in tetragonal phase, an intermediate gradient lattice strain layer (GLSL), and a surface layer in cubic phase. In stark contrast to the conventional *two layer model* that contains only an inner core (tetragonal phase) and surface layer (cubic phase),^{75, 76} the extra GLSL layer, whose lattice parameters and atomic positions can change continuously, was introduced to account for the

lattice mismatch between the inner tetragonal phase and the surface cubic phase.^{75, 76} In this model, the surface cubic layer remains a constant thickness of 10 -15 nm, independent of particle size, while the other regions change their thickness with particle size.^{75, 76} When the BaTiO₃ particle size drops to a critical size where the tetragonal core doesn't exist, the ferroelectricity of BaTiO₃ disappears as well. This model can also be used to explain the size effect of dielectric permittivity. It is widely believed that the permittivity of ferroelectric BaTiO₃ (tetragonal core) is higher than that of paraelectric BaTiO₃ (surface cubic layer).⁷⁶ The transition GLSL layer exhibits the similar permittivity with the tetragonal phase.^{75, 76} As a consequence of the size-dependent volume fraction of ferroelectric phase and paraelectric phase, the dielectric constant displays strong size-dependence as well (see example in **Figure 2a**). Many reports have supported this model and it agrees well with experimental measurements.^{73, 97, 98}

Theoretically, the size-dependent ferroelectricity and the disappearance of ferroelectricity at lower dimensions can be well-explained by the depolarization effect. Depolarization fields in ferroelectric materials arise from incomplete compensation for the ferroelectric polarization charges.^{99,100} As shown in **Figure 3a**, for a ferroelectric material with polarization P , a total surface charge density (σ) of $\sigma=p \cdot n$ is induced (where p is the polarization vector and n is the unit normal to the surface) due to the discontinuities of polarization near the vicinity of the surface.¹⁰¹ As a result, a depolarization field oriented in the opposite direction of the spontaneous polarization is produced inside the ferroelectric material, which reduce the ferroelectricity of the material. (**Figure 3b**)¹⁰² However, the surface charges are unstable if they are not compensated by external screening electrodes, as a result, a net depolarization field (E_d) develops and can be described by the following

equation:⁹⁹ $E_{dep} = -\frac{P}{\epsilon_F} \left(\frac{2\epsilon_F/l}{2\epsilon_F/l + \epsilon_e/l_s} \right)$, where ϵ_F and ϵ_e represent the dielectric constant of the

ferroelectric material and the screening electrode, respectively; l_s and l denote the screening

length and the thickness of the ferroelectric film, respectively. In the case where the ferroelectric material is sandwiched between two perfect metallic electrodes, *i.e.* $\epsilon_e \rightarrow \infty$, the surface charges can be completely compensated, so no net depolarization field will be introduced ($E_d \rightarrow 0$). On the other hand, when partially compensated, the depolarization field is not fully cancelled, as described by the above equation. It is clear from the equation that, only in the limit when $l \rightarrow \infty$ or $l_s \rightarrow 0$, the depolarization field vanishes. However, for extremely small dimension when $l \rightarrow 0$ and at relatively large screening lengths, a significant depolarization field will build up, resulting in the disappearance of ferroelectricity at small dimensions.

In addition to size, the shape of BaTiO₃ NCs can also influence their dielectric and ferroelectric properties. (*i.e.* shape effect).¹⁰³ For example, 10 nm diameter BaTiO₃ nanoparticles tend to have suppressed ferroelectricity at room temperature due to the decreased Curie temperature, while 1D BaTiO₃ nanowires with 10 nm diameter retain their ferroelectric properties.⁷⁷ In contrary to 0D nanostructures, 1D nanostructures tend to be influenced by extrinsic strains which are generated during the fabrication process. Depending on the types of strain produced in BaTiO₃ nanostructures, they can either enhance the polarization or suppress it.¹⁰³

2.3. Surface Effects

Depending on the preparation method, the surface of as-prepared BaTiO₃ NCs can be covered with different molecular adsorbates, such as hydroxyl groups (OH) if prepared by sol-gel or hydrothermal techniques, or carbonaceous species if synthesized from various precursor routes.¹⁰⁴ More importantly, most of these atomic or molecular adsorbates can better stabilize the ferroelectricity of nanoscale BaTiO₃.¹⁰⁵ In this regard, many efforts have been made to tailor the surface of BaTiO₃ NCs for manipulating their dielectric and ferroelectric properties. To date, surface modification has been widely achieved through

chemical bonding with surface ligands^{104, 106} and coatings.¹⁰⁷ In one study, the n-hexylphosphonic acid (HPA)-functionalized BaTiO₃ NCs possess improved dielectric constant but displayed decreased sensitivity to temperature and frequency in comparison to unmodified BaTiO₃ NCs.¹⁰⁴ Another study involving coating of a manganese (Mn) layer on 40 nm BaTiO₃ nanoparticles demonstrates that surface coating can preserve the ferroelectricity of extremely small particles, enabling them to adopt a pure tetragonal ferroelectric phase.¹⁰⁷ Transmission electron microscopy (TEM) observations show that the Mn coating produces an amorphous phase and hence cause some strain near the grain boundary of the samples, which is believed to be the main cause of the increased tetragonality and the preservation of ferroelectricity below the critical size of unmodified particles.^{75, 76}

3. Synthesis of BaTiO₃ NC via Chemical Methods

Currently, most BaTiO₃ materials used in industrial applications are still prepared by conventional solid-state reactions which require high temperatures (above 1000 °C), and the resulting BaTiO₃ materials are normally polycrystalline with uncontrolled morphologies that are not suitable for advanced applications.¹⁰⁸⁻¹¹³ Alternatively, a controlled synthetic scheme could produce highly crystalline nanoparticles with a monodisperse size distribution for targeted performance properties and applications. It would also enable systematic variation of their size and shape, make it possible to study the size-dependent and shape-dependent properties. Finally, controlling the crystalline phase so that BaTiO₃ can readily switch between the paraelectric and ferroelectric phases is also important for designing advanced materials for devices.¹¹⁴ Satisfying all the requirements noted above, chemical approaches are an accepted alternative to the traditional solid-state approach. Owing to the more uniform mixing between barium and titanium cations, chemical methods are able to yield stoichiometric NCs with well-controlled size, morphology and crystallinity. This preserves the dielectric properties while maintaining a low reaction temperature and reduced energy

consumption.^{115, 116} The elimination of high temperature processes cuts the cost of fabrication and makes it much easier to scale up.^{117, 118} A large number of synthetic methods fall into the category of chemical approaches, including organo-metallic,³⁹ solvothermal/hydrothermal,^{51, 53} and template methods.^{55, 56} Thus, chemical methods offer the most flexible approach to obtain high quality BaTiO₃ NCs with well controlled morphology (e.g., nanodots, nanorods, nanocubes, and nanowires) and crystal structure (e.g., cubic or tetragonal). All of these methods are covered in subsequent sections. Within each category, representative examples are provided to illustrate the general synthetic strategy and NC growth mechanism.

3.1 Formation Mechanism of BaTiO₃

The controlled growth of BaTiO₃ with desired morphology requires a good understanding of the nucleation and crystallization mechanism. A lot of factors, including the rate of nuclei formation, the rate of crystalline growth, and agglomeration of crystals can contribute to the overall particle growth process and the size distribution of BaTiO₃ particles.¹¹⁹ Both classical and nonclassical crystal nucleation and growth processes have been used to describe the nucleation of many chemical systems.¹²⁰ In a classical crystal nucleation and growth process, ions and molecules firstly aggregate together to reach a supersaturated state which triggers the nucleation process. Once the nucleus reaches some critical size, crystal growth can occur.¹²¹ The nonclassical theory differs from the classical theory in that the crystals may grow from mesoscale solid species instead of nuclei.

In general, several different theories have been proposed to describe the nucleation and growth process, including the Lamer burst nucleation mechanism,^{122, 123} Ostwald ripening,¹²⁴ Finke-Watzky two step mechanism, coalescence and oriented attachment and intraparticle growth. The Lamer mechanism proposes that a “burst-nucleation” process takes place instantly once there is a large amount of free monomers in the solution, which leads to

the quick consumption of free monomers and stops the nucleation process. The remaining free monomers in solution then diffuse to the nucleus leading to crystal growth.¹²⁰ The Ostwald ripening mechanism describes the growth of particles by dissolving smaller particles since they have higher surface energy and hence higher solution solubility.^{120, 124} The dissolved particles diffuse and redeposit on the surface of larger particles, making them into much bigger ones.

The dominating nucleation and growth mechanism of BaTiO₃ varies a lot for different growth methods. Even for the same growth method, no agreement has been reached regarding the growth mechanism.¹²¹ In following sections 3.2-3.6, various soft chemical growth methods of BaTiO₃ NCs are discussed, with growth mechanisms for some growth methods also covered.

3.2 Organometallic Methods

Organometallic methods (also known as the hot injection methods) use organometallic precursors possessing a fixed stoichiometric ratio of the metal cations dissolved in some organic solvent. It provides an ideal environment for controlling NCs growth because the nucleation process and the subsequent growth processes are separated. In a typical organometallic process, as depicted in **Figure 4**, the organometallic precursors are quickly injected into the reaction system at a high temperature, leading to rapid nucleation. The temperature drops after injection of precursors and the growth process starts to occur. Surfactants or stabilizing agents are usually present in this crystal growth process for controlling the morphology of the resulting NCs.³⁸ So far, this method has achieved great success in synthesizing a rich variety of NCs, including semiconductor³⁷⁻³⁹ and metal oxide¹²⁵⁻¹²⁷ types, and is widely regarded as the best approach for controlling both the size and morphology of the resulting NCs.¹²⁸

In a typical procedure for synthesizing BaTiO₃ NCs, a moisture-sensitive bimetallic alkoxide, for example, barium titanium ethyl hexano-isopropoxide (BaTi(OR)₆), is injected into mixed solvents of diphenyl ether and oleic acid at 140 °C under argon or nitrogen atmosphere. Diphenyl ether is the solvent while oleic acid serves as the stabilizing agent for enabling the transfer of particles to nonpolar solvents and preventing their aggregation. The bimetallic alkoxide precursors with equal amounts of Ba and Ti ions provide the correct stoichiometry (*i.e.*, Ba to Ti ratio) in the resulting product.⁴⁹ Hydrogen peroxide is further injected into the system once it is cooled to 100 °C to trigger the hydrolysis of the precursor and the formation of uniform BaTiO₃ nanoparticles with a diameter of 8 nm. By increasing the precursor/oleic acid ratio or adding more peroxide solution to the system, larger nanoparticles (9-12 nm) can be created. Lowering the ratio reduces the particle diameter to 4-6 nm. In addition, the resulting BaTiO₃ nanoparticles self-assembled into regular superlattice structures owing to the strong van der Waals or dipolar interactions between particles.

Since the first successful reports of nearly monodisperse NCs produced by this hydrolysis method, it has been limited to the preparation of isotropic 0D sphere-like morphologies. However, anisotropic 1D nanostructures (*e.g.* nanowires, nanorods, nanotubes) are more promising building-blocks for realizing advanced devices because of their wire-like connectivity which enables efficient transfer of heat, stress, and charge.⁵⁴ The first report of preparing BaTiO₃ nanorods by this method is quite similar to that of forming isotropic BaTiO₃ nanoparticles, with similar mixed solution of diphenyl ether and oleic acid containing the bimetallic alkoxide precursor (BaTi[OCH(CH₃)₂]₆) as precursor, and the hydrolysis were triggered by the injection of hydrogen peroxide. Anisotropic growth of resulting nuclei into nanorods is achieved through slow precursor decomposition and crystallization at a high temperature (280 °C) within a micelle structure formed by the precursor and oleic acid. Furthermore, the resulting nanorods are of cubic phase, according to the XRD pattern shown in the inset of **Figure 5**, and each nanorod is a single crystal.

Although the organo-metallic approach is successful at producing NCs of the highest quality, its broad utilization in industry is limited largely owing to scale-up issues, the exotic reagents, and the use of expensive and highly toxic organometallic precursors. In addition, the consumption of large amounts of organic solvent further complicates its use due to environmental concerns.¹²⁹ Therefore, more environmentally-friendly and more cost-effective methods are desirable for industrial applications.

3.3 Solvothermal/Hydrothermal Growth

Solvothermal/hydrothermal methods are also powerful tools for the controlled syntheses of various nanomaterials.¹³⁰⁻¹³⁶ They have received the most interest because they can produce high quality crystalline powders at low temperatures in one-step reactions.^{119, 121, 137} The solvothermal/hydrothermal reactions occur by sealing organic or aqueous solutions in an autoclave and increasing the solvent temperature to a desired reaction temperature higher than the normal boiling point of the solvent due to the pressure buildup during heating within the autoclave. As a result, crystalline powders with nanoscopic morphologies can be formed, accompanied by some unexpected reactions.¹³⁸ Normally, these nanoscopic morphologies formed during the solvothermal/hydrothermal reactions can be easily controlled by varying the reaction parameters, solvents, precursors,¹³⁹⁻¹⁴² capping reagents/surfactants,¹⁴³⁻¹⁴⁵ reaction temperature,^{146, 147} pH,¹⁴⁸⁻¹⁵⁰ and the Ba/Ti ratio. Furthermore, these NCs are difficult to form by many other conventional methods .

3.3.1 Hydrothermal Methods

The hydrothermal synthesis of BaTiO₃ is a low cost, one-step reaction process involving an aqueous medium under strong alkaline conditions. In the early period of producing BaTiO₃ for pigment applications, BaTiO₃ was widely prepared by reacting Ba(OH)₂ with TiO₂ at the boiling point of water under hydrothermal conditions.¹³⁷ Later,

other groups extended this method to producing BaTiO₃ NCs or thin films for electronic applications.^{151, 152}

Various titanium precursors including titanium oxide (TiO₂), titanium tetrachloride (TiCl₄), titanium alkoxide or titanium oxide gel, and barium precursors have been used to produce BaTiO₃ NCs with desired sizes and shapes. In a study of hydrothermally producing BaTiO₃ NCs by two different sets of starting materials,¹⁵³ the BaTiO₃ NCs (sample A) produced using titanium hydroxide (Ti(OH)₄) and barium hydroxide (Ba(OH)₂·8H₂O) as precursors exhibited uniform size (D~ 65 nm) and shape with narrow size distribution (**Figure 6a**), while sample B prepared using titanium dioxide (TiO₂) and barium hydroxide are less uniform. (**Figure 6b**). The comparison also indicated that the internal strain in the as-prepared BaTiO₃ NCs was higher in particles of sample B than sample A. However, in neither case were the stresses sufficient enough to induce the cubic-to-tetragonal phase transition, leaving both sample A and B to exhibit a metastable cubic phase.^{154, 155} In addition, the as-prepared BaTiO₃ powders prepared from this hydrothermal method exhibited a high concentration of lattice defects of OH⁻ and cation vacancies. These induce some strain within the the metastable cubic phase and caused some tetragonality.^{154 155} By varying the concentrations of the lattice OH⁻ through changing the reaction parameters, properties such as stoichiometry (Ba/Ti ratio), defects, size and shape can be varied.¹⁵⁴

The hydrothermal growth of anisotropic 1D BaTiO₃ nanostructures can be achieved by varying the reaction parameters or adding surfactants. For example, a seed-induced hydrothermal reaction between equimolar Ba(OH)₂ and TiO₂ particles was utilized to synthesize BaTiO₃ nanowires (**Figure 7a-7b**).⁴⁸ As shown in the graphical representation of growing BaTiO₃ nanowires from TiO₂ nanoparticles (**Figure 7c**), TiO₂ particles acted as seeds for the redeposition of dissolved Ba(OH)₂ particles and the subsequent growth of anisotropic BaTiO₃. By controlling the pH and temperature of the system, higher aspect ratio nanowires can be achieved.

The hydrothermal method is also capable of producing other intriguing nanostructures, owing to its unique reaction conditions. For example, novel bowl-like BaTiO₃ nanoparticles were obtained by hydrothermal reaction between Ba(OH)₂·8H₂O and TiO₂ at 180 °C for 72 hours. The Ba/Ti molar ratio in this reaction was altered to give a greater amount of Ba precursor.⁵¹ As shown in **Figure 8a-8c**, both scanning electron microscope (SEM) and TEM confirm the bowl-like morphology of the resulting BaTiO₃ nanoparticles (D = 100-200 nm) which had a concave center.

The growth mechanism of hydrothermally produced nanostructured BaTiO₃ varies greatly by using different starting materials. Recently, a novel ion-exchange reaction mechanism was utilized for producing BaTiO₃ nanowires.⁵² In this study, alkali-metal titanate precursors, such as Na₂Ti₃O₇ nanowires and K₂Ti₄O₉ nanowhiskers experienced ion-exchange and conversion with Ba(OH)₂, producing BaTiO₃ nanowires. Since the resulting BaTiO₃ nanowires preserve the relative size and shape of the Ti precursor (*i.e.* the K₂Ti₄O₉ nanowhiskers, Na₂Ti₃O₇ nanowires), BaTiO₃ nanowires produced from K₂Ti₄O₉ nanowhiskers (**Figure 9d**) are much longer than those obtained from Na₂Ti₃O₇ nanowires (**Figure 9c**).

In addition, different BaTiO₃ formation mechanisms due to the different titanium precursors also influence the number of defects in the resulting BaTiO₃ NCs.¹⁵⁶ It was found that BaTiO₃ nanopowders synthesized using TiO₂ nanoparticles have higher tetragonality (c/a=1.0081) than those synthesized using titanium isopropoxide (c/a=1.0070). Despite these differences, they exhibited similar sizes and shapes. This is because when using TiO₂ as the titanium precursor during the hydrothermal synthesis, the resulting BaTiO₃ specimens exhibited less OH⁻ or Ba vacancy defects, leading to higher tetragonality.¹⁵⁶

The size and shape of hydrothermally-produced BaTiO₃ NCs can be controlled by adding surfactants and controlling the preferred growth facets. In a study, oleic acid was used as a surfactant for producing cube-like BaTiO₃ NCs (**Figure 10a-10f**).⁵³ During the

hydrothermal reaction, oleic acid was adsorbed to the formed BaTiO₃ nanocrystals creating a hydrophobic surface which further leads to the growth of low index facets such as (100) planes in BaTiO₃ NCs. This is because these facets are nonpolar and thus more stable than higher index planes such as (110) and (111).^{53, 157}

In addition to 0D and 1D BaTiO₃ NCs, 2D conformal BaTiO₃ films can also be produced by scalable hydrothermal method. When hydrothermally growing conformal BaTiO₃ thin films, rutile TiO₂ is the most commonly used Ti precursor as rutile TiO₂ can be uniformly grown over all substrate surfaces regardless of their dimension or geometry.¹⁵⁸ Moreover, it also functions as template for controlling the morphology of the resulting BaTiO₃ films. **Figure 11a-11e** depict the strategy involving two hydrothermal reactions to grow conformal textured BaTiO₃ films and the corresponding SEM images. As illustrated, an array of TiO₂ nanowires (NWs) ranging in length from 2 to 8 μm were first grown on a FTO-coated silicon wafers by a hydrothermal process at 180°C. Afterwards, the conformal TiO₂ NW arrays were converted into conformal BaTiO₃ thin films during the second hydrothermal reaction at 240°C, where TiO₂ was first dissolved to form Ti(OH)₄ that reacts with Ba²⁺ ions and then deposited a layer of BaTiO₃ particles on the surface of TiO₂ NWs. As the process continued, BaTiO₃ crystals grew, converting the conformal TiO₂ arrays into continuous and crack-free BaTiO₃ films. The thickness of the resulting BaTiO₃ films is directly related to the thickness of the TiO₂ NWs.¹⁵⁸ Compared with most of the current methods for the conformal deposition of BaTiO₃ films, such as metal-organic chemical vapor deposition (MOCVD) and atomic layer deposition (ALD), hydrothermal methods possess the advantages of easy controllability, easy scalability, and cost-effectiveness. Moreover, hydrothermal approach with optimized reaction conditions described above is capable of improving the performance and storage capacity of the resulting electronic devices.

3.3.2 Solvothermal Methods

Similar to the hydrothermal method, the solvothermal method refers to reactions in a sealed autoclave using nonaqueous solvents. In a typical procedure of solvothermally producing BaTiO₃ nanoparticles in the presence of anhydrous benzyl alcohol as the solvent, the dissolved metallic barium reacts with titanium isopropoxide at temperatures between 200 and 220 °C via a mechanism involving C-C (carbon-carbon) bond formation.^{159, 160} The resulting BaTiO₃ nanoparticles are single crystals with diameters ranging from 4-5nm (**Figure 12a-12c**). Because of the elimination of halide precursors and other inorganics such as alkali metal ions, this method is capable of producing extremely high-purity samples.

Another facile solvothermal method of using barium hydroxide monohydrate (Ba(OH)₂·H₂O) and titanium butoxide (Ti[O(CH₂)₃·CH₃]₄) as starting materials has recently been developed.¹⁶¹ The particle size of solvothermally produced BaTiO₃ nanoparticles can be controlled by the mixed solvents of diethanolamine (DEA) and triethanolamine (TEA) since the organic amines increase the number of nucleation sites, leading to a reduction in particle size. In addition, the BaTiO₃ nanoparticles synthesized by this solvothermal method showed some tetragonality which could be potentially used for miniaturized devices that require ferroelectric response or large dielectric constants.

3.4 Template-assisted Methods

Template-assisted methods involve the directed crystallization of NCs within a specific area of a template. Such methods are simple and efficient for fabricating nanostructures with well-controlled morphologies.¹⁶²⁻¹⁶⁵ Templating methods are typically low cost, easily reproducible, large yields, environmentally benign, and flexible. To date, a large number of BaTiO₃ nanostructures including nanodots, nanotubes and nanotube arrays have been reported by this approach with either a “*hard template*” (e.g., anodic aluminum oxide (AAO) and TiO₂) or “*soft template*” (e.g., polymers, peptides and biomaterials).

3.4.1 Hard Templating

Nanofabrication of ordered structures using a negative template which has 1D holes or channels, such as porous anodic aluminium oxide (AAO) membranes or track-etched polycarbonate, have received much attention due to their ability to produce a large number of ordered structures without the need for expensive or extreme conditions.¹⁶⁶⁻¹⁶⁹ Typically, the porous templates are immersed in the precursor solutions, followed by the evaporation of solvents under high temperature, which triggers the growth of crystals along the surface of the porous template. The nanostructures are finally produced by selectively removing the template either by dissolution or calcination at elevated temperature.¹⁷⁰ The dimensions and array pattern of produced NCs can be easily tuned by varying the reaction conditions, such as precursor concentration, pH, immersion time, temperature, pore structure and surface properties.^{171, 172} In a study of growing 1D BaTiO₃ nanostructures with anodic aluminum oxide (AAO) as a structure-directing template from aqueous solutions, stoichiometric BaTiO₃ nanotubes over large areas were successfully produced under near-ambient conditions (**Figure 13**).¹⁷² In this study, the precursor solution with controlled concentration and pH was made by dissolving Ba(NO₃)₂ and (NH₄)₂TiF₆ in an aqueous acidic solution. Through the liquid-phase deposition and hydrolysis of cations, nanotubes with thinner tube walls were produced. The AAO template was modified by (octadecyl)trichlorosilane (OTS) to make it hydrophobic so as to decrease the overall deposition rate and suppress pore blocking. The obtained BaTiO₃ nanotubes were around 250 nm in diameter and 2.5 μm in length. Even longer and more stoichiometrically balanced BaTiO₃ nanotubes can be obtained by adjusting the dimensions of the AAO template. A similar method was also reported for growing BaTiO₃ nanoshell tubes with controllable wall thickness.¹⁷¹ An extra wetting process was introduced and driven by the reduced surface energy of the system under ambient conditions. This allowed the incoming polymeric precursor to form a thin layer on the wall and crystallize into BaTiO₃ nanoshell tubes with a shell thickness of 100 nm and controllable aspect ratio (over

50). After annealing at high temperature, the BaTiO₃ nanotubes displayed ferroelectric switching properties.

In addition to AAO templates, other templates have also been used to direct the growth of nanostructured BaTiO₃ NCs. For example, track-etched hydrophilic polycarbonates (PC) were proved to be effective templates for producing BaTiO₃ nanorods.¹⁷³ In this approach, a combination of sol-gel processing and electrophoretic deposition was utilized in which the Pt mesh anode was immersed in the precursor sol while the PC membrane was attached to the aluminum cathode and placed on top of the precursor sol. After applying a 5V potential between the electrodes, the BaTiO₃ nanorods begin to grow, yielding denser oxide nanorods with improved quality compared to other methods without the electrophoretic deposition process.

In contrast to negative templates which have voids or holes for precursor filling, positive templates (shape of desired structure to be templated) such as 1D TiO₂ nanostructures and their arrays can be directly convert into 1D BaTiO₃ nanostructures because they serve as both precursors and physical templates.^{93, 174} For example, Li *et al.*⁹³ produced single crystalline BaTiO₃ nanotube arrays using a hydrothermal method with TiO₂ nanotube array as templates. During the reaction process, the TiO₂ nanotube arrays reacted with the dissolved Ba ions in the solution while producing BaTiO₃ nanotubes that preserve the original shape of the TiO₂ template. TEM results (**Figure 14a-14b**) of randomly selected top-view of BaTiO₃ nanotubes confirmed the identical crystallographic orientations of the produced BaTiO₃, indicating that all BaTiO₃ nanotubes have identical crystallographic orientation during their growth. XRD pattern (**Figure 14c**) of BaTiO₃ nanotube arrays further indicated the high purity of BaTiO₃ nanotubes, suggesting that the TiO₂ nanotube templates had been completely converted into BaTiO₃ nanotubes.^{174, 175}

Besides 1D mesoporous structures (*i.e.*, AAO or TiO₂ tubes), 0D spherical nanoparticles can also be used as templates. A representative example reports the use of

colloidal arrays of polystyrene (PS) spheres as templates for producing macroporous BaTiO₃ structures.¹⁷⁶ In brief, the BaTiO₃ precursors were allowed to penetrate through the voids in a 3D ordered PS template formed by assembling 726 nm PS spheres into planar ordered arrays. Through solidification and subsequent calcination, an array of macroporous BaTiO₃ was formed while retaining the long-range order of the PS colloidal array template, exhibiting an ordered hexagonal close-packed structure (**Figure 15**). Another similar study of utilizing colloidal PMMA particles as templates produced hollow BaTiO₃ spheres.⁵⁶ In this example, multilayered colloidal titanate spheres were prepared by depositing the titanium precursors on the colloidal template, followed by dissolution of the PMMA template in tetrahydrofuran (THF) for producing hollow titanate spheres. Finally, the hollow titanate spheres served as the new template and were converted into hollow BaTiO₃ spheres by reaction with Ba(OH)₂ solution under hydrothermal conditions. The resulting hollow BaTiO₃ spheres displayed a well-defined size and shape conforming to the PMMA template (**Figure 16**). In addition, by controlling the number of layers deposited onto the PMMA template, the wall thickness of the hollow BaTiO₃ spheres can also be varied. The results indicate that they have a well-defined diameter dictated by the diameter of the template and uniform wall thickness controlled by the number of layers deposited.

3.4.2 Soft Templating

As discussed in Section 2, one of the main challenges is to produce high quality BaTiO₃ NCs of tetragonal crystalline structure (ferroelectric phase with high dielectric permittivity) at low temperature. Most of the BaTiO₃ NCs obtained so far, especially those below 10 nm, are in the cubic phase because it is the thermodynamically stable phase at room temperature due to size effects.^{75,76} To convert the cubic phase into the ferroelectric tetragonal phase, extra steps such as post-annealing at high temperature are usually required. These extra steps increase the complexity and cost of production and often lead to many other

problems, such as nanoparticle aggregation and coarsening.^{57, 177} The first example of tetragonal BaTiO₃ nanoparticles produced at room temperature was made by Yang *et. al.*⁵⁷ In this study, a peptide nanoring template self-assembled into a structure with some cavities in the center which can load the bimetallic precursor BaTi(O₂CC₇H₁₅)[OCH(CH₃)₂]₅ and allow the precursor to hydrolyze and crystallize into BaTiO₃ nanoparticles (**Figure 17a**). By adjusting the pH value, the cavity size of the nanorings varies between 6 and 12 nm. This enables a flexible tailoring of the diameter of the resulting BaTiO₃ nanoparticles. Surprisingly, the resulting BaTiO₃ nanoparticles exhibit some ferroelectricity which seems to contradict the *core-shell* model which states that the BaTiO₃ particles are supposed to be a pure cubic structure around 12 nm (Section 2).^{75, 76} Further analysis indicates that the high surface tension within the peptide cavities and the unique surface chemical features of the obtained BaTiO₃ nanoparticles due to the use of peptide template contribute to the observed unusual tetragonal phase at room temperature in such small BaTiO₃ nanoparticles. Therefore, it is possible to control the crystal structure of BaTiO₃ NCs by modifying their surface properties.

57

Other soft templates such as peptides isolated by bacteriophages (viruses) were also used to produce tetragonal BaTiO₃ NCs at room temperature.²⁸ In a typical approach, peptides carried by two unique phages were added to the aqueous precursor solution, they rapidly induce the formation of tetragonal BaTiO₃ nanoparticles after an incubation step at pH = 6.8 for 2 h (**Figure 18a-18c**). The resulting BaTiO₃ NCs (50-100nm) quickly precipitated and aggregated into larger clusters (0.3-0.5 μm in size). In a more recent work, researchers demonstrated that genetically engineered M13 virus can serve as a biotemplate for producing tetragonal BaTiO₃ nanoparticles at room temperature. More importantly, the resulting nanoparticles exhibit higher crystallinity and smaller sizes (10~30 nm in size).¹⁷⁸

Despite lots of progress in producing 0D and 1D BaTiO₃ NCs, it remains a challenge to produce well-controlled three-dimensional (3D) BaTiO₃ nanostructures.^{177, 179} Recently, a

bottom-up templating approach was developed for producing 3D BaTiO₃ nanostructures and other compounds with multiple components.¹⁷⁷ In a typical procedure, the 3D morpho helenor butterfly wing bio-organic template was coated with titania-bearing precursors in a computer-controlled layer-by-layer sol-gel process. The coated 3D templates were further heated to 450 °C to convert the precursor coating into nanocrystalline titania while preserved the 3D scales of the bio-organic wing template. In the following hydrothermal reaction, the pyrolyzed scales were converted into 3D nanocrystalline BaTiO₃ by the reaction between titania and barium acetate. As shown in the SEM images in **Figure 19**, the butterfly morphology was successfully preserved and transferred into the BaTiO₃ NCs.

In addition to natural bio-organic templates, rationally-designed polymers have also been explored as templates for controlling the morphology of nanocrystals. Recently, Lin *et al.* proposed a novel generalizable templating approach to synthesize monodisperse colloidal nanocrystals, such as BaTiO₃, with controllable sizes and shapes.^{50, 180} The templates used are a series of star-like block co-polymers prepared by sequential atom transfer radical polymerization (ATRP) and azide-alkyne (CuAAC) click reaction. The templates include star-like poly(acrylic acid)-block-polystyrene (PAA-*b*-PS) and poly(acrylic acid)-block-poly(vinylidene fluoride) (PAA-*b*-PVDF). The precursors preferentially incorporate into the space occupied by the PAA blocks in star-like PAA-*b*-PS and PAA-*b*-PVDF. The coordination bonding between the metal-containing precursors and the carboxylic acid functional groups of PAA at elevated temperatures (180 °C) led to the selective formation of BaTiO₃ nanocrystals capped by PS and PVDF, respectively. As shown in **Figure 20b**, the PVDF-capped BaTiO₃ nanoparticles are single crystals. They are highly uniform with diameters around 10 nm. The size of the BaTiO₃ nanoparticles can be easily tuned by changing the molecular weight of the inner PAA block where the crystal selectively grows. In addition, the covalently tethered polymer ligands on the surface of the BaTiO₃ nanoparticles (either PS or PVDF) facilitate easy dispersion of BaTiO₃ in organic solvents. The BaTiO₃

nanoparticles ($D = 10$ nm) prepared by this templating method exist in the ferroelectric tetragonal phase. This was further supported by piezoelectric force microscopy (PFM) (as shown in **Figure 20c** and **20d**). This flexible star-like copolymer templating approach can also be used to make nanocrystals of different structures (spherical, core@shell and hollow) by varying the type and number of polymer blocks. This approach has also proven effective in templating a wide assortment of functional nanocrystals for various applications.¹⁸⁰⁻¹⁸⁵

3.5 Molten Salt Methods

Nearly all of the methods discussed above are based on solution processes which yield relatively small quantities of materials and in many cases involve the use of extremely toxic and unstable precursors. In this context, developing gram-scale, environmentally-friendly methods with reproducible shape control is highly desirable for industrial and practical applications. The molten salt method utilizes molten salts as the solvent to grow NCs. It is one of the most efficient methods to address the issues of scalability and toxicity and has been shown to successfully grow various metal oxides.¹⁸⁶⁻¹⁸⁸ In this approach, molten salt plays a critical role in the whole process as a reaction medium in which reactants dissolve and precipitate to produce the NCs in large quantities. The surface and interfacial energy balance between the constituents and the molten salt influences the morphology and overall shape of the resulting nanocrystals.⁵⁸

In a seminal work, Wong *et. al* reported a simple, large-scale solid-state reaction for preparing single-crystal BaTiO_3 nanostructures in molten NaCl at 820°C in the presence of a nonionic surfactant.¹⁸⁹ The procedure is simple. Typically, barium oxalate (depending on the desired nanostructure), TiO_2 , NaCl, and NP-9 (nonylphenyl ether surfactant) are mixed. The mixture is then placed in a quartz crucible, inserted into a quartz tube, annealed at high temperature, and subsequently cooled to room temperature. BaTiO_3 NCs are obtained by simply washing away the salt with water. TEM images of the center region of one of the BaTiO_3 nanowires are shown in **Figure 21**. While a thin amorphous layer exists on the outer

nanowire surface, the images clearly show that the BaTiO₃ nanowires are uniform and homogeneous. The 2-D lattice fringes confirm that the nanowire is crystalline with no defects or dislocations. Energy-dispersive X-ray spectroscopy (EDS) analysis (**Figure 21c**) from different positions along the nanowires showed that the chemical composition of the nanowires is identical and the nanowires are essentially composed of Ba, Ti, and O. Moreover, the SAED patterns taken from different positions along the same nanowires are also identical. This indicates that the BaTiO₃ nanowires are single crystals. Due to its simplicity and generalizability, this method can likely be extended to the large-scale synthesis (gram quantity) of other important ferroelectric systems at the nanoscale such as PbTiO₃ and BaZrO₃.

The synthesis of other well-defined BaTiO₃ nanostructures, including spheres, cubes and rods, is also reported using a molten-salt synthesis method using BaO/BaCO₃ and TiO₂ in a NaCl-KCl molten salt mixture.⁵⁸ Three different morphologies were obtained with different barium precursors and shaped titanium precursors (spheres, rods and cubes). Spheres were synthesized by reacting BaCO₃ with spherical TiO₂. The cube and rod shapes were synthesized when BaO or BaCO₃ barium precursors reacted with rod-shaped TiO₂ as shown in the SEM images in **Figure 22**. XRD results show no impurity peaks in the tetragonal phase nanostructures. In addition, the products are found to have the same shapes as the starting TiO₂ nanostructures (*i.e.*, spherical TiO₂ resulted in spherical BaTiO₃ while rod-shaped TiO₂ formed rod-shaped BaTiO₃). The shape of the products can thus be modified by changing the shape of the precursors. The growth mechanism for the cube and rod shapes is proposed in **Figure 23**. (1) When the barium precursor dissolves faster than the titanium precursor (upper panel in **Figure 23**), BaCO₃ dissociates and dissolves in the molten salt upon further heating. It then coats the TiO₂ nanostructures forming the shell. The barium precursors then react with the TiO₂ to form BaTiO₃ rods. (2) When the barium precursor dissolves slower than the titanium precursor (lower panel in **Figure 23**), the rod shaped TiO₂ nanostructures can break

apart prior to BaO dissolution. The reaction continues to occur in these smaller pieces leading to the formation of BaTiO₃ cubes.⁵⁸

Recently, BaTiO₃ nanostrips were also synthesized in a surfactant-free molten salt process.¹⁹⁰ This surfactant-free approach is simple, general, and applicable to the growth of a number of 1D perovskite materials including BaTiO₃. In a typical procedure, barium oxalate is mixed with TiO₂ and NaCl-KCl. The mixture is then heated to the melting temperature of NaCl-KCl (657°C) which facilitates the formation of BaTiO₃. As the temperature increases, BaTiO₃ seeds start to nucleate and grow preferentially along one direction and grow into nanostrips. SEM and TEM images of the as-synthesized BaTiO₃ samples are shown in **Figure 24**. The resulting BaTiO₃ consists of well-defined, straight nanostrips with lengths from a few micrometers to tens of micrometers. As shown in the width-distribution histogram of the BaTiO₃ nanostrips in the inset of **Figure 24a**, the BaTiO₃ nanostrips are clearly faceted and have a rectangular cross section with widths and thicknesses in the range of tens of nanometers. High magnification SEM (**Figure 24b**) shows a rectangular end on the nanostrip with a width of approximately 120 nm and a thickness of 40 nm. High Resolution Transmission Electron Microscopy (**HRTEM**) of a single BaTiO₃ nanostrip shows lattice fringes, indicating their high crystallinity (**Figure 24d**). This study is the first to report on perovskite nanostrips produced by a molten salt process with no added surfactant. A novel mechanism was proposed to explain the crystal growth process (**Figure 25**). First, the barium oxalate, TiO₂ and NaCl-KCl powders are mixed together. Second, the molten salt is heated to melt (657 °C) and the reaction system forms a molten solution. At this point, chemical reactions can occur forming barium titanate seeds. Third, as the temperature further increases (950 °C), the seeds start to grow via the orientated attachment mechanism. Fourth, with continued growth the structures form into long nanostrips. Furthermore, it was suspected that the merging of the crystal seeds may lead to symmetry breaking along the axis because the

individual seeds spontaneously self-polarize along the growth axis through the displacement of Ti^{4+} and O^{2-} ions in different directions.¹⁹⁰

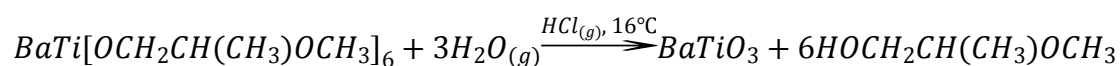
Compared to other soft chemical methods, the molten salt approach is advantageous due to its simplicity, low cost and high yield. It is the most promising method for industrial scale synthesis, but the resulting materials are usually of lower quality (*i.e.*, morphology and particle size are not well-defined). Moreover, the reaction process requires high temperatures, and the products generally cannot be well-dispersed in organic solvents (the organic ligand is usually decomposed at high temperatures) limiting its application in various areas including biomaterials, organic-inorganic hybrids, and film formation among others.

3.6 Sol-gel Methods

The sol-gel approach is an established method for fabricating well-defined inorganic crystals from small molecules. The sol-gel process typically involves the conversion of monomers into a colloidal particle solution (“sol”) through hydrolysis and polymerization of a metal alkoxide which acts as the precursor for the formation of a gel-like system containing liquid and solid phases. After a drying process to remove the liquid phase in the “sol” and further calcination, inorganic crystals are obtained.¹⁹¹⁻¹⁹³ Depending on the solvent evaporation rate, temperature, reaction conditions and solvent type, the microstructure of the final products can vary greatly. Compared to other soft-chemical methods, the sol-gel process costs less, and is compatible with continuous manufacturing techniques for the massive production of powders.

As previously shown, most nanocrystal synthesis reactions rely on elevated reaction temperatures for crystallization (>140 °C). The low-temperature synthesis of perovskite nanocrystals is inherently difficult as it requires more complex synthesis techniques involving temperature and spatial precision.⁶⁰ Sol-gel techniques enable the nanoscale mixing of reagents which significantly reduces the length scale for diffusion and nucleation of

crystalline materials. This enables the reaction temperature to be significantly reduced.¹⁹⁴ Recently, a vapor-diffusion sol-gel route has been presented for making high quality crystalline BaTiO₃ nanoparticles at lower temperatures without any templates. For example, BaTiO₃ nanoparticles were readily prepared by precisely controlling the H₂O(g)/HCl(g) vapor flowed into an organic solution of a bimetallic alkoxide (BaTi[OCH₂CH(CH₃)OCH₃]₆) at 16 °C. The controlled catalytic hydrolysis and condensation of the bimetallic alkoxide, as described by the following reaction, provides the required conditions for the nucleation and growth of small, high quality BaTiO₃ nanoparticles :



TEM images in **Figure 26a**, and **Figure 26c-26d** show an assembly of partially-aggregated quasispherical BaTiO₃ NCs due to the absence of surfactants. A selected area electron diffraction pattern (**Figure 26b**) supports the cubic structure of BaTiO₃ nanoparticles. This was the first to report on the synthesis of small, high quality BaTiO₃ nanoparticles at significantly lower temperatures (16 °C).

Other morphologies, such as thin films and fibers, have also been successfully prepared by sol-gel methods.^{195, 196} Compared with other deposition techniques for fabricating BaTiO₃ thin films, sol-gel methods are simpler and do not require high-vacuum levels.¹⁹⁵ It also enables better control of the composition and morphology of the resulting BaTiO₃ thin films. In one study, multiple BaTiO₃ thin films were deposited on different substrates via successive spin coating treatments of a 0.25M Ba-Ti sol in air. After each layer deposition, films were heated to 350 °C on a hot plate to remove residual organics. The gel films were then decomposed by a heat treatment (600 °C) to form an intermediate crystalline phase of BaTiO₂CO₃ with a 5-10 nm grain size. These films are subsequently transformed to polycrystalline thin films with a grain size of 20-60 nm. This work showed that the morphology and dielectric properties of the resulting BaTiO₃ films is greatly influenced by the interfacial reactions between BaTiO₃ films and different substrate materials. The

incorporation of high concentrations of water in the sols suppressed the formation of the intermediate phase enabling the film porosity to be significantly reduced.¹⁹⁵

It was found that the properties of BaTiO₃ films produced by sol-gel techniques showed a heavy dependence on their processing parameters.¹⁹⁷ In one study of fabricating BaTiO₃ thin films using titanium isopropoxide (Ti(OC₃H₇)₄) as the titanium source with two different barium precursors, the sols were prepared by adding the titanium precursor into the barium precursor and refluxed at 80 °C. The filtered sols were then spin-coated onto different substrates and cured at different temperatures in air. The BaTiO₃ thin films prepared from two different barium sources were transparent and crack-free below 600 °C. Films prepared from the barium 2-ethyl hexanoate precursor were found to crystallize around 550 °C into a tetragonal polycrystalline phase. In contrast, films prepared from the barium hydroxide precursor crystallized into the cubic phase at 600 °C. In addition, the films prepared from the ethyl hexanoate precursor had higher porosities due to greater size reduction (*i.e.* shrinking) during heat treatment.¹⁹⁶

Sol-gel synthesis methods are green and scalable growth techniques for the large production of perovskite nanoparticles (among nanoparticle compositions).¹⁹⁸ The solution-based sol-gel synthesis of BaTiO₃ typically relies on the hydrolysis of metal-organic precursors in alcohol-based solvents. It is essential that the concentration of water and metal-organic precursors be well controlled so that the hydrolysis and cross-linking of the metal-organic precursors is slow. This enables the production of uniform and aggregate-free colloidal perovskite nanoparticles that are highly crystalline and pure. This green process can realize a nearly quantitative yield of perovskite nanocrystals and demonstrates its great promise in the fabrication of high performance dielectric thin films potentially in industrial scale quantities.¹⁹⁸

Researchers have developed a rapid, low-temperature route for the synthesis of nanocrystalline BaTiO₃ based on a sol-gel approach.¹⁹⁹ The BaTiO₃ sols, BaTiO₃ gels, and

BaTiO₃ precipitates were synthesized via the controlled hydrolysis of metal-organic precursors in mixtures of different alcohols and ethylene glycol (EG), diethylene glycol (DEG), triethylene glycol (TEG), or tetraethylene glycol (TTEG) solvents. BaTiO₃ nanocrystals were produced with sizes of 2.8 and 5.1 nm in 15 min to 2 h. The small BaTiO₃ nanocrystalline sols are suitable for coating, spraying, and printing techniques, making them an economic material for quickly fabricating highly crystalline BaTiO₃ thin films.¹⁹⁹

In one study, the crystal structure of BaTiO₃ nanocrystals were converted from amorphous to crystalline morphologies.²⁰⁰ In the work, small BaTiO₃ nanocrystals (less than 10 nm) were grown via a vapor diffusion sol-gel method at room temperature. Mixed bimetallic alkoxide precursors dispersed in n-butanol/2-methoxypropanol were first transferred to a reaction flask. The flask was then bubbled with an HCl solution in nitrogen gas to produce a N₂/HCl/H₂O vapor across the precursor solution. During the vapor flow, the solution viscosity gradually increased, resulting in an amorphous metal-organic gel. The hydrolysis and condensation of the bimetallic alkoxide BaTi(OCH₂CHCH₃OCH₃)₆ caused the solution to gel after 8 h of reaction. After reaction for 12h, 3-6 nm diameter BaTiO₃ nuclei formed in an amorphous metal-organic matrix. These nuclei continued to grow, yielding individual 9 nm diameter BaTiO₃ nanocrystals after 30 h. After reaction for 72 h, the amorphous-to-crystalline phase transition was complete, and the resulting 9 nm BaTiO₃ nanocrystals possessed a cubic phase.²⁰¹ In **Table 1**, we summarized the results and experimental conditions for synthesizing BaTiO₃ nanocrystals by the various synthetic methods addressed herein.

Table 1. Experimental conditions for the synthesis of BaTiO₃ nanocrystals via various synthetic methods.

Synthesis Methods	Precursors	Reaction Conditions	Morphologies	Phases	References
Organo-metallic	BaTi(O ₂ CC ₇ H ₁₅)[OCH(CH ₃) ₂] ₅	Injected precursors at 140 °C under argon or nitrogen;	8 nm diameter BaTiO ₃ nanoparticle	Cubic	⁴⁹

		Reacted at 100 °C for over 48h			
Organo-metallic	BaTi[OCH(CH ₃) ₂] ₆	280 °C for 6 h	30-nm diameter BaTiO ₃ nanorod	Cubic	54
Hydrothermal	Ba(OH) ₂ ·8H ₂ O and anatase TiO ₂	1-72 h at 90 °C	Nanoparticle		138
Hydrothermal	Ba(OH) ₂ ·8H ₂ O and rutile TiO ₂ powder; Ba/Ti ratio varies from 1.2 to 1.8	160 °C for 3-24h	40-50 nm diameter nanoparticle	Cubic	152
Hydrothermal	TiCl ₄ /Ba(NO ₃) ₂	400 °C, 30 MPa, 8ms	90-260 nm nanoparticle	Cubic	153
Hydrothermal	Sample A: Ti(OH) ₄ and Ba(OH) ₂ ·8H ₂ O Sample B: TiO ₂ and Ba(OH) ₂ ·8H ₂ O	100 °C for 5 h.	Sample A: average 65 nm nanoparticle Sample B: 80 nm coarse-faceted nanoparticle	Cubic	154
Hydrothermal	Ba(OH) ₂ and TiO ₂ particles	170 °C for 3 days	Nanowires, with diameters of 50-200 nm and lengths from a few to tens of μm	Cubic with tetragonal symmetry	48
Hydrothermal	Ba(OH) ₂ ·8H ₂ O and TiO ₂	80°C for 12 h	Bowl-like structures with 100-200 nm in diameter	Tetragonal	51
Hydrothermal	Ba(NO ₃) ₂ and Ti(Bu) ₄	135 °C for 18h	22 nm cube-like BaTiO ₃	Cubic	53
Solvothermal	metallic barium and titanium isopropoxide	200 °C for 48 h	4-5 nm nanoparticles	Cubic	161
Solvothermal	Ba(OH) ₂ ·H ₂ O and Ti[O(CH ₂) ₃ ·CH ₃] ₄	200 °C for 48 h	106.69 nm diameter nanoparticles	Tetragonal	163
Hard templating	metal acetate Ba(OAc) ₂ Titanium isopropoxide Ti(OPri) ₄	700 °C for 6h	50-μm-long tubes with 200-nm outer diameters	Cubic	174
Hard templating	Ba(NO ₃) ₂ and (NH ₄) ₂ TiF ₆	Near-ambient conditions for 24 h	BaTiO ₃ nanotubes with diameter of 250 nm and length of 2.5 μm	Cubic	173
Hard templating	BATIO 9101 polymeric precursor	First anneal in air at 300 °C, then at 850 °C for 1 h for crystallization	BaTiO ₃ nanotubes with diameters from 50 nm to several micrometers	Tetragonal	201
Hard templating	titanium(IV) isopropoxide and barium acetate	700 °C for 15-30 min	nanorods of 125~200 nm in diameter and 10 μm in length		175
Hard templating &	Ba(OH) ₂ and TiO ₂	200 °C for 2 h	Well-ordered arrays of BaTiO ₃	Tetragonal	176

Hydrothermal			nanotubes		
Hard templating	Ba(AC) ₂ and Ti(C ₄ H ₉ O) ₄	Solidifying the composite in a vacuum desiccator for 24 h and subsequently calcining the sample at 700 °C	Macroporous BaTiO ₃ nanoparticles		178
Hard templating & hydrothermal	Ba(OH) ₂ , Titanium (IV) bis(ammonium lactate) dihydroxide (TALH)	120°C for 1 day.	Hollow BaTiO ₃ spheres; diameter dictated by the diameter of the template		56
Soft templating	BaTi(O ₂ CC ₇ H ₁₃)[OCH(CH ₃) ₂]	Irradiated by long-wave UV light (355 nm) for 10 h	6-12 nm diameter BaTiO ₃ nanoparticles	Tetragonal	57
Soft templating	titanium(IV) isopropoxide and barium acetate	heated to 220 °C in a microwave reaction system for 10 h	heated to 220 °C in a microwave reaction system BaTiO ₃ butterfly	Tetragonal	179
Soft templating	TiCl ₄ and BaCl ₄	180 °C for 2 h	10 nm BaTiO ₃ nanoparticles	Tetragonal	50
Molten salt	barium oxalate and anatase TiO ₂	Annealed at 820 °C for 3.5 h	BaTiO ₃ nanotubes	Cubic	117
Molten salt	BaCO ₃ and TiO ₂	700 °C for 1 h	Rod-shaped BaTiO ₃	Tetragonal	58
Molten salt	barium oxalate and TiO ₂	950 °C for 5 h	BaTiO ₃ nanostrips	Tetragonal	192
Sol-gel	BaTi[OCH ₂ CH(CH ₃)OCH ₃] ₆	16 °C for 15h	6nm BaTiO ₃ nanoparticles	Cubic	60
Sol-gel	Ba(OiPr) ₂ , Ti(OiPr) ₄	45–55 °C for 2–10 h	6.6 nm BaTiO ₃ nanoparticles	Cubic	199

4. Ferroelectric Properties of Individual BaTiO₃ Nanostructures

4.1 Ferroelectricity at the Nanoscale

Ferroelectricity describes a material possessing a spontaneous electrical polarization that can be switched under the application of an external electric field. This switchable polarization is ideal for use in devices for memory storage (writeable memory) and microelectronics.²⁰² Nanoscale ferroelectric materials make it possible to design ferroelectric devices that can operate at the atomic scale. However, nanoscale ferroelectric materials behave differently than their bulk ferroelectric counterparts. The characteristic properties of bulk ferroelectrics relate to the macroscopic polarization of domains to achieve energy minimization. In contrast, nanoscale ferroelectrics possess continuous uniform polarization

across the whole structure.²⁰² At the nanoscale, there is a large surface-to-volume ratio. This essentially means that the role of surface effects and surface interactions (i.e interfaces) becomes more important. Consequently, surface effects play an important role in nanoscale ferroelectricity.²⁰³ The direct probing of ferroelectricity in individual BaTiO₃ nanostructures is essential for developing their applications in nanoscale devices and understanding the effects of size and surface area on the nanoscale.

4.2. Probing the Ferroelectricity of Individual BaTiO₃ NCs by Piezoresponse Force Microscopy (PFM)

As previously described, the rapid development of electronic devices based on ferroelectric nanomaterials has necessitated the study of ferroelectric properties at the nanoscale. One of the most promising applications is data storage, where the polarization behavior of ferroelectrics is particularly important because the polarizations are both stable and switchable despite the small size. This high density of nanoscale, writable polarization is essential for storing greater amounts of information in smaller areas (*i.e.* high information storage density): a requirement of all electronic devices.¹¹⁴ The manipulation of ferroelectric polarization on individual BaTiO₃ NCs has been realized via piezoresponse force microscopy (PFM). This technique is based on the measurement of the local piezoelectric deformation (*i.e.* physical shape change) of a ferroelectric material caused by an applied external electric field.²⁰⁴ As shown in a typical PFM setup in **Figure 27a**, AC and DC voltages are applied to the sample under detection and the cantilever. The sample expands and contracts in response to the applied electric field, and the oscillation signal of the cantilever are read out as amplitude signal (**Figure 27b**) and phase signal (**Figure 27c**). The 180 degree phase change (**Figure 27c**) signifies the switching behavior of ferroelectric materials. PFM (**Figure 28**) can be operated in two modes: vertical PFM mode and lateral PFM mode. In the vertical PFM mode, the locally-induced vertical deformation is measured by the deflection of an AFM cantilever to measure polarization in the normal direction (**Figure 28a**). In the lateral PFM

mode, the locally-induced shear deformation of the sample is measured by the twisting of the AFM cantilever to measure polarization in the plane (**Figure 28b**). In addition to domain visualization, the conductive tip can also be used to modify the initial domain structures (*e.g.* read and write the polarization). By applying a DC voltage larger than the coercive voltage of the ferroelectric sample between the tip and the bottom electrode, a local polarization can be induced.²⁰⁴ The small size of the PFM probe tip allows local ferroelectric properties to be characterized with high resolution and precision.^{62, 63, 204, 205} In this section, a review of recent advances in PFM characterization and the manipulation of different BaTiO₃ nanostructures to demonstrate their unique ferroelectric behavior is presented.

In their seminal work, Park *et al.*^{86, 206} successfully induced and manipulated the electrical polarization of several nanoscale domains in a single crystalline BaTiO₃ nanowire by an external electric field. This work demonstrated the presence of ferroelectricity despite the small radial dimension of the nanostructures. The ferroelectric properties of individual BaTiO₃ nanowires were investigated using scanning probe microscopy (SPM) (**Figure 29**). A voltage (V_{tip}) was applied to the conductive tip in order to induce or “write” local electric polarization normal to the nanowire long axis. Next, the written polarization was probed or “read” by measuring the shift in the resonance frequency of the SPM cantilever while scanning with a small V_{tip} using electrostatic force microscopy (EFM). As shown in **Figure 29a**, the as-deposited nanowires show no obvious EFM contrast. This indicates that pristine nanowires do not exhibit polarization normal to the wire axis. After the writing procedure, a local electric polarization normal to the wire axis was induced. By changing V_{tip} from +10V to -10V, the polarization direction could be reversed (**Figure 29a**). The written polarizations could be retained for more than 5 days as shown in **Figure 29b**. The polarization reversal shown in **Figure 29c** indicated a clear memory effect (*i.e.* remanence-to-saturation ratio close to 1) in this ferroelectric nanowire. The EFM images in **Figure 30b-30f** show multiple polarization domains as small as 100 nm² can be induced and manipulated (*i.e.* written, read

and rewritten) on a single nanowire. These observations make ferroelectric nanowires an attractive material for future information storage as a memory component. Nanowires may be well-suited for applications in nonvolatile memory (NVM) devices.

Subsequently, Park *et al.* also explored the dependence of the ferroelectric phase transition temperature (T_C) on nanowire diameter (d_{nw}) through variable-temperature scanning probe microscopy.¹⁰⁵ The ferroelectric phase transitions were investigated by measuring the time variation of the EFM signal from individual nanowires as a function of T . As shown in **Figure 31a**, a series of EFM images were obtained from a 25-nm diameter nanowire at two different temperatures (below and above T_C). Below T_C , the signal remained stable for more than 7 days. This indicates that the nanowire retained its ferroelectric character. In contrast, above the T_C , the induced polarization was not stable and gradually decayed over time. The T_C obtained as a function of the nanowire diameter (d_{nw}) showed that the T_C in larger diameter nanowires approached that of the bulk material (400 K) but quickly reduced as d_{nw} decreased (**Figure 31b**). Based on these measurements, the diameter at which T_C falls below room temperature is roughly 3 nm. In other words, BaTiO₃ nanowires must have diameters less than 3 nm to have ferroelectric properties (*i.e.* read-write polarization domains) at room temperature. Extrapolation of the data indicates that nanowires with d_{nw} as small as 0.8 nm can support ferroelectricity, but at temperatures below room temperature. Moreover, the inset of **Figure 31b** clearly shows that the reduction of T_C is inversely proportional to d_{nw} . This suggests that the suppression of ferroelectricity is a consequence of a depolarizing field (*i.e.* a field caused by an incomplete balance of surface charges that opposes the induced polarization) as previously described.¹⁰⁵ When combined with density functional theory (DFT) results for naked and coated BaTiO₃ surfaces, it was found that the nanowire ferroelectricity is stabilized by the hydroxyl and carboxyl groups adsorbed to the surface in BaTiO₃ nanowire coatings. These adsorbed chemicals can balance the surface charges and

stabilize the ferroelectricity. This supports the observation of stable ferroelectric domains in small BaTiO₃ nanowires.

Recently, larger crystalline BaTiO₃ nanowires (50–80 nm in diameter and 10 μm in length) have also been characterized by piezoforce microscopy techniques.⁵² PFM images of BaTiO₃ nanowires before and after the poling process are shown in **Figure 32**. No obvious contrast can be observed before the poling process, indicating that the original BaTiO₃ nanowire shows no polarization (**Figure 32a**). After poling via application of an external electric field, the PFM readings show two different states with the as-grown state marked “1” and the single-poled state marked “2” (**Figure 32b**). The latter indicates the formation of a local polarization domain normal to the wire axis. However, due to presence of internal and external hydroxyl defects and oxygen vacancies (*i.e.* a depolarization field), the induced polarization decayed slowly in air over a day.⁵²

In addition to nanowire structures, ferroelectricity in lower dimensional nanostructures can also be detected by PFM probes. Itoh *et al.* directly observed ferroelectricity in BaTiO₃ nanoparticles with sizes as small as 25 nm using PFM technique.²⁰⁷ As shown in **Figure 33a-33b**, the nanoparticles are tightly aggregated with thickness on the order of a single-particle dimension in the majority of places measured. The hysteresis loops for BaTiO₃ nanoparticles with two different sizes (**Figure 33c-33d**) unambiguously confirm the ferroelectric component, coexisting with a more dominant paraelectric component. The remnant piezoresponse was smaller in 25 nm particles than that in 35 nm particles. However, the opposite trend was observed for the coercive voltage with the 25 nm particles having a larger value. This observation also supports a clear particle size effect on the ferroelectric properties.

The ferroelectric properties of ordered arrays of BaTiO₃ nanodots prepared by pulsed laser deposition (PLD) were also investigated using PFM.²⁰⁸ As shown in **Figure 34b**, the bright regions in the piezoresponse domain image show that the dots have a downward-oriented polarization. The polarization was weak because there was minimal ferroelectric

phase (tetragonal) present in the arrays. Despite the weak polarization, the arrays can still be switched by PFM (**Figure 34c-34d**). There are a few factors that remain to be investigated including improving the uniformity of the templated arrays, and understanding the relationship between polarization and size in these structures..²⁰⁸

Nanocrystals with unusual shapes can also be characterized with PFM. For example, the ferroelectricity of bowl-like BaTiO₃ nanoparticles synthesized by a hydrothermal method has been investigated by PFM (**Figure 35**). The well-defined bowl-like nanoparticles (**Figure 35a**) have a uniform size 100-200 nm in diameter including the particle rim (I) and the center depressed area (II) shown. Both the characteristic “butterfly” loops and piezoelectric hysteresis loops were shown in **Figure 35b**. The effective piezoelectric coefficient ($d_{33}^* = 28$ pm/V) is calculated based on the “butterfly” loop. These results clearly show that the polarization remains both switchable and spatially dependent in more unusually-shaped nanocrystals.⁵¹

In traditional PFM measurements, an oscillatory AC test signal is applied between the probe and a conductive sample substrate to induce a local oscillatory deformation due to the converse piezoelectric effect (**Figure 36a**). This setup has limitations whenever a high bias is required for in-plane polarization switching or a sample requires uniform polarization to avoid electric breakdown.²⁰⁹ To resolve this problem, a new experimental approach has been designed for the study of nanoscale piezoelectric properties in one-dimensional nanowires.²⁰⁹ As shown in **Figure 36b**, a DC bias is applied along the ferroelectric nanowire axis. This provides in-plane polarization control and allows for the investigation of ferroelectric hysteresis and piezoelectric response to shear in nanowires using PFM. Using this new PFM approach, Wang *et al.* successfully showed the ferroelectric and piezoelectric properties of BaTiO₃ by measuring the polarization saturation along the long axis of a one-dimensional nanowire.²⁰⁹ The 180 degree phase change in the square loop (**Figure 36c**) and the classical

butterfly amplitude loop (**Figure 36d**) indicated the existence of polarization along the axial direction of single BaTiO₃ nanowire.²⁰⁹

To further improve the performance of BaTiO₃ nanomaterials, hybrid nanocomposite materials integrating BaTiO₃ and polymers with complementary properties have been prepared. These nanocomposites offer the potential for superior performance, processability and scalability far beyond pure BaTiO₃ nanostructures. Ferroelectric nanocomposites are the focus of the following sections.

5. Dielectric Properties of BaTiO₃–Polymer Nanocomposites

5.1. Theoretical Models for the Dielectric Properties of Polymer-Ceramic Nanocomposites

In a two-phase composite material made of high dielectric constant ceramic fillers and a polymer matrix with a high breakdown strength, the filler provides the dielectric properties while the matrix provides mechanical properties. A number of models have been proposed for predicting the dielectric properties of polymer-ceramic composites of various compositions. Depending on the ceramic filler loading and the polymer and ceramic components interaction, three generally accepted models have been developed for explaining the observed properties. These models are the Maxwell-Garnett formulation, the Bruggeman self-consistent effective medium approximation, and the Jaysundere-Smith formulation.²¹⁰

5.1.1 Maxwell-Garnett Equation

Consider the mixing condition when ceramic particles of permittivity k_f (where the volume fraction is ϕ_f) are mixed into an isotropic polymer matrix of dielectric permittivity k_m (where the volume fraction is ϕ_m , $\phi_m=1-\phi_f$). In this model, the permittivity of the two-component composite (k_c) lies between a lower permittivity ($k_{c,min}$) and an upper permittivity

($k_{c,max}$) value ($k_{c,min} \leq k_c \leq k_{c,max}$) with the two limiting values described by the following equations:²¹¹

$$k_{c,min} = \frac{k_m k_f}{k_m \phi_f + k_f \phi_m} \quad (1)$$

$$k_{c,max} = k_m \phi_m + k_f \phi_f \quad (2)$$

The lower bound ($k_{c,min}$) is described by a series model in which both the polymer and ceramic components are connected in two dimensional layers to form layers parallel to the electrode films (equation 1). The upper permittivity ($k_{c,max}$) corresponds to a parallel model in which each phase is connected in two dimensions where the layers formed are perpendicular to the electrode film.²¹¹ Practical two-phase composites are described by this mixing model in which some average between the two pure arrangements exists. This model is the simplest to understand, however it tends to deviate for larger concentrations of filler. It also doesn't account for the possibility of aggregation of the various components as well as not considering the impact of particle shape on composite permittivity.

Further efforts to model the dielectric properties of two-phase composites have led to a more accurate equation (the Maxwell-Garnett equation) for predicting the dielectric properties of composites. The Maxwell-Garnett equation is valid for low spherical ceramic filler concentrations and is described by the following equation:^{211, 212}

$$k_c = k_m \left[1 + \frac{3\phi_f(k_f - k_m)}{(1 - \phi_f)(k_f - k_m) + 3k_m} \right] \quad (3)$$

For more general situations when the ceramic particles are not a uniform spherical shape, a modified version of the Maxwell-Garnett equation has been developed. This equation takes into account the geometry of the dispersed filler particles in the polymer matrix and is more accurate in predicting the dielectric properties of two-phase composites. The more general Maxwell-Garnett equation considering the geometry of dispersed particles is described by equation 4,²¹¹ where the parameter A is the shape-dependent depolarization

factor ($A = 1/3$ for spherical particles, $A > 1/3$ for oblate ellipsoid particles limiting to disc shapes, and $A < 1/3$ for prolate ellipsoid particles limiting to rods).

$$k_c = k_m \left[1 + \frac{\phi_f(k_f - k_m)}{A(1 - \phi_f)(k_f - k_m) + k_m} \right], \quad \text{for } \phi_f < 0.1 \quad (4)$$

The more accurate Maxwell-Garnett equation is also reasonable for composites consisting of a continuum polymer matrix with low concentrations of ferroelectric particle filler ($\phi_f < 0.1$).²¹³

5.1.2 Bruggeman Self-consistent Effective Medium Approximation

In contrast to the Maxwell-Garnett equation, the Bruggeman self-consistent effective medium approximation treats each phase equally and assumes that all components are randomly mixed together with no requirement for uniformity of the filler particle dispersion within the polymer matrix.^{213, 214} This theory has been widely used to predict the dielectric and optical properties of composite materials. It provides more accurate property prediction at higher spherical filler content (ϕ_f up to 0.5). Bruggeman's formula is described by equation 5:

211

$$\frac{k_f - k_c}{k_c^{1/3}} = \frac{(1 - \phi_f)(k_f - k_m)}{k_m^{1/3}} \quad (\phi_f < 0.5) \quad (5)$$

5.1.3 Jaysundere-Smith Equation

In the situation where a low concentration of filler is present in the composite, the interaction between filler particles is too weak due to a large separation distance between neighbors. Thus, this interaction is neglected. However, at higher filler concentrations when the particles are more closely located to one another, neighboring filler particles have the potential to interact with one another and produce internal electrical fields due to local dipole

moment formation. Taking into consideration the interaction of local particle dipole interactions, the Jaysundere-Smith equation is described as follows:²¹¹

$$k_c = \frac{k_m \phi_m + k_f \phi_f \frac{3k_m}{(2k_m + k_f)} [1 + 3\phi_f \frac{k_f - k_m}{2k_m + k_f}]}{\phi_m + \phi_f \frac{3k_m}{(2k_m + k_f)} [1 + 3\phi_f \frac{k_f - k_m}{2k_m + k_f}]} \quad (6)$$

5.2. Common Strategies for Preparing BaTiO₃-Polymer Nanocomposites and Their Dielectric Properties

As the size of electrical devices becomes increasingly smaller, it still necessitates the incorporation of many different components including resistors, capacitors and inductors which are quite large and take up a large area on device substrates. To break this size reduction dilemma while still improving the device performance, much efforts have been made to develop high dielectric constant materials and utilize them in the form of thin films or directly use nanostructured materials to shrink the device size.²¹⁵ Because of its high dielectric constant (over a range of 50~6000),⁹⁰ BaTiO₃ becomes one of the most popular candidate materials for capacitor applications, especially for nanostructured BaTiO₃ as their utilization in capacitors can shrink device size while still maintaining a high energy storage capability.^{88,}
²¹⁶ As the device size reduction demands more from key materials, BaTiO₃-polymer nanocomposites have received more attention than pure BaTiO₃. This is because the BaTiO₃-polymer nanocomposites combine the advantages from each constituent, such as easy processibility and higher breakdown strength from polymer matrices and high dielectric constant from BaTiO₃ fillers. As a result of the synergy effect in the nanocomposites, a significant increase in the energy storage density can be achieved.²¹⁷

The choice for polymer matrices is quite broad. However, there are several principles to follow when selecting polymer component, such as high breakdown strength, high dielectric constant, low cost, environmentally friendly, to name a few. In this regard, poly(vinylidene difluoride) (PVDF) stands out as the most commonly used one, owing to its

high breakdown strength of 590 kV mm^{-1} and high dielectric constant of $8.4@1\text{MHz}$ (a high value among polymers).^{106, 217} Realizing a high dielectric constant, high breakdown field strength, and low dielectric loss at the same time is not trivial in BaTiO_3 -polymer composites. Therefore the best approach is a compromise of these three desired properties by adjusting the volume ratio of each component, the size and shape of the BaTiO_3 particles, the crystalline phase of each component, the material interfaces, and the uniformity of the nanocomposites.^{210, 216} Traditionally, BaTiO_3 -polymer composite films are prepared via physical mixing of a dielectric polymer solution with submicron or micron-sized ferroelectric particles followed by solvent evaporation.²¹⁸ This simple, direct mixing method often results in significant aggregation of filler particles due to no compatibilization between the filler and the polymer matrix. This leads to problems in the resulting devices including higher dielectric losses and reduced breakdown strengths as a result of aggregation-induced local depolarization caused by filler exclusion from the matrix.²¹⁹

In order to achieve high dispersion and increased loading of BaTiO_3 nanocrystals in polymer matrices, surface functionalization of nanocrystals with surface modifiers (small molecules and polymers) has been investigated.²²⁰ As a result, well-controlled nanocrystal/polymer interfaces can be realized leading to improved dispersions of nanocrystals within polymer matrices. New structures with ultra-small BaTiO_3 nanocrystals carried by various inorganic nanostructures have also been developed, for the purpose of further enhancing the dielectric performance of the nanocomposites.^{221, 222, 223} In addition, polydopamine has been widely utilized as a coating layer onto the nanofiller in order to improve the compatibility and homogeneity of the nanofiller within the matrix.^{224, 225} It is generally believed that an ideal and controlled BaTiO_3 nanocrystal/polymer interface is required to achieve high permittivity and large dielectric constants while also minimizing the leakage current and improving the energy density. Ideal interfaces should possess a tough insulating layer that prevents direct contact between the dielectric materials of neighboring

particles as well as proper surface modification of the particle surfaces to enable their dispersion in a polymer matrix.²²⁶ It has been demonstrated that a tailored interface formed by surface-grafted polymers can significantly reduce dielectric loss because the grafted polymer layer can hinder interfacial transport and effectively restrict particle-particle hot spots.²²⁷

In this section, we will discuss recent progress in the design and characterization of BaTiO₃-polymer nanocomposites that satisfy the above standards with a focus on “grafting-to” and “grafting-from” strategies. In “grafting-to” strategies, the polymer chains are first polymerized by various methods and then attached to the surface of various nanocrystals.¹⁰⁶ In “grafting-from” strategies, polymer chains are grown from the surface of nanocrystals functionalized in such a way to initiate polymerization (commonly some form of controlled radical polymerization).^{228, 229} For each strategy, several representative examples are discussed to summarize the common synthetic routes to nanocomposites and their improved dielectric performance.

5.2.1 “Grafting-to” Methods

In the “grafting-to” method, a polymer is tethered to the surface of a nanocrystal via a physical or chemical interaction. This surface modification can increase the dispersion of BaTiO₃ NCs in a polymer matrix. Marder, Perry *et al.* performed a systematic investigation of the binding affinity of a variety of functional groups to the surface of BaTiO₃ nanoparticles and the compatibilization of the surface-modified BaTiO₃ nanoparticles with polymer hosts such as polycarbonate (PC) and poly(vinylidene difluoride-co-hexafluoropropylene) (P(VDF-HFP)).¹⁰⁶ Their results indicated that ligands bearing phosphonic acid functional groups can form a strong, and stable organic shell on BaTiO₃ nanoparticles that can improve their dispersion in various polymer matrices. The nanocomposites formed from phosphonic acid-modified BaTiO₃ nanoparticles and polymers exhibited high energy-storage capacities as well as high dielectric permittivities and improved dielectric constants. Specifically, (2-[2-(2-

methoxyethoxy)ethoxy]ethyl)phosphonic acid (PEGPA) was coated on BaTiO₃ nanoparticles to enable their dispersion in a polycarbonate (PC) matrix. Since PEGPA has a tail composed of ether linkages and an alcohol, it can improve the dispersion of BaTiO₃ nanoparticles in polar hydrophilic solutions (**Figure 37a**, left). Similarly, pentafluorobenzyl phosphonic acid (PFBPA) was also investigated as it possesses a fluorinated benzyl group that provides improved dispersion in fluorinated elastomers and organic solvents (**Figure 37a**, right). Such chemical functionalization of BaTiO₃ reduced nanoparticle aggregation. This was supported by the significant reduction in nanoparticle aggregate size which ultimately lead to more uniform films with homogeneous nanoparticle dispersions. The frequency-dependent capacitance and loss tangent measurements indicated that the nanocomposites retained a high dielectric constant ($\epsilon_r = 37 \pm 2$ at 1 kHz for 50 vol% PFBPA-BaTiO₃ in P(VDF-HFP)) and a large dielectric strength (210 ± 50 kVmm⁻¹) suggesting these materials have a high energy-storage capacity.¹⁰⁶

In the above work, it was found that the volume fraction of BaTiO₃ nanoparticles (the high permittivity component) must be increased beyond 30% in order to increase the nanocomposite permittivity. However, the tradeoff with increasing the BaTiO₃ content is that it reduces the dielectric strength of the nanocomposite. Therefore, the BaTiO₃ volume fraction in a nanocomposite needs to be optimized to realize the best performance and energy storage density.²³⁰ In this study, phosphonic acid-modified BaTiO₃ and poly(vinylidene fluoride-cohexafluoropropylene) (P(VDF-HFP)) were used to investigate the role of high permittivity BaTiO₃ nanoparticles on the various dielectric properties of the formed nanocomposites including dielectric loss, permittivity, and breakdown strength (**Figure 37b**).²³⁰ The results showed that at lower BaTiO₃ volume fractions, measured effective permittivity of the nanocomposites matched well with self-consistent effective medium field (SC-EMT) modeling calculations with a peak relative permittivity of 35. Interestingly, when the volume fraction is greater than 50%, a reduction in the effective permittivity was observed with

increasing particle loading. This behavior was found to relate heavily to the porosity of the resulting films. Similarly, the breakdown strength of the films decreased rapidly with 10% BaTiO₃ loading and subsequently reduced more with additional nanoparticle loading. These results, in conjunction with model calculations, suggest that the nanoparticle connectivity and path structure within the nanocomposites, as well as the porosity, greatly influence their properties.²³⁰

As previously discussed, dispersants (*i.e.*, surfactants and capping ligands) can be used to better incorporate fillers (BaTiO₃ NCs) into polymer matrices by improving their dispersion. However, most dispersants reported to date react only with the surface of the fillers and are unresponsive to the presence of the polymer matrix (*i.e.* minimal favorable interaction and/or chemical reactivity). Recently, a silane coupling agent was reported to act as a bridge between the fillers and the polymer matrix thus enabling improved compatibility between the two components.²¹⁹ The BaTiO₃ nanoparticles are functionalized with the coupling agent, γ -aminopropyltriethoxy silane (KH550), in ethanol solution (**Figure 38a**). Next they were dispersed in N,N-dimethylformamide (DMF) which contains the polymer matrix material, *i.e.*, polyvinylidene fluoride (PVDF). The mixture is subsequently formed into nanocomposite films with good dispersion and uniformity, due to the good bonding effect of KH550. In addition, an optimized coupling agent content (\sim 1.0 wt%) was found to increase the compatibility bringing the dielectric loss of the composite below 10⁵ Hz, as shown in **Figure 38b-38c**, the dielectric loss of the nanocomposites is less than 0.05 below 10⁵ Hz, making such nanocomposites applicable as a dielectric in capacitors.²¹⁹

In addition to surface modification and physical mixing, a photopolymerization technique has also proven effective in making ceramic/polymer nanocomposites with improved dispersion and uniformity.²³¹ In a typical experiment, BaTiO₃ fillers are added into liquid monomers to form suspensions which are then subjected to UV radiation at ambient temperatures. The photocurable monomers form highly cross-linked polymer networks with

integrated particles once photocured. This photopolymerization method has several advantages. First, liquid monomers can readily penetrate into and around the BaTiO₃ particles to ensure a highly integrated suspension and subsequent cured matrix. Second, there are a large variety of monomers that can be photocured thus enabling excellent control over the mechanical properties of the composites. The mechanical properties of such materials are typically essential for their practical incorporation into more complex devices.²³¹ This work used three different photocurable monomers possessing different polarities for use as polymer matrices. These monomers include trimethylolpropane triacrylate (TMPTA), poly(ethylene glycol) diacrylate (PEGDA), and 1,14-tetradecanediol dimethacrylate (TDDMA). The results showed that polar polymers not only increase the dielectric constant of the composites at low frequencies but also increase the dielectric loss. Moreover, the thermal dependence of the dielectric constant is also heavily dependant on both the polymer polarity and their mobility at low frequencies.

Besides traditional solution-based processes for nanocomposite fabrication, electron beam vapor deposition has also been reported.²³² This approach has the advantage of requiring no solvents and offers rapid fabrication times. The composites are formed on Al-coated Si substrates under high-vacuum using a co-deposition system to produce BaTiO₃ nanoparticles dispersed within high dielectric constant polyaniline-polyurethane (PANI-PU) copolymer networks. Capacitor performance (frequency-independent capacitance density ~ 10 nF/cm², loss tangent = 0.1, at 200 MHz) of the as-deposited and annealed nanocomposites was found to be promising for applications in radio frequency (RF) technologies.

In addition to BaTiO₃/polymer binary systems, ternary nanocomposites containing two inorganic materials (BaTiO₃ and SiO₂) coated with polymers (*e.g.* polyimide (PI)) have also been reported.²³³ Silica-coated BaTiO₃ was prepared by a sol-gel method to improve the stability of BaTiO₃ nanoparticles as well as enable coupling via a difunctional amino-silane molecule. The polymer was coated on the surface of BaTiO₃-SiO₂ by a dispersion

polymerization method where 3-aminopropyltriethoxysilane (APTES) was added as a coupling agent to provide a connection between the inorganic domains and the polymer matrix. FTIR analysis supported the covalent connection between the silica-coated BaTiO₃ and the polyimide matrix. As a result of the coupling between the polyimide matrix and the silica-coated BaTiO₃, the nanocomposites showed an enhanced thermal stability when compared to simpler binary systems.

In addition to silica, titanate NDZ101 has also been used to modify BaTiO₃ nanoparticles to establish cross-linking between BaTiO₃ nanoparticles and polymers.²³⁴ NDZ101 is one kind of coupling agent possessing both alkoxy and alkyl chains. In this study, the alkoxy chains are believed to react with surface hydroxyl groups on BaTiO₃. Simultaneously, the long alkyl chains of the cross-linker entangle with the polymer component. It was found that the titanate-coated BaTiO₃ nanoparticles dispersed well in polyvinylidene difluoride matrices. It was further verified by FT-IR that coupling occurred at both the particle-titanate interface and the titanate-polymer interface. The coated BaTiO₃/PVDF nanocomposites showed improved dielectric performance with increased breakdown strengths as high as 250 kVmm⁻¹, peak energy densities of 4 J/cm.²³⁴ It is clear that titanate plays a role in improving the connectivity between the inorganic and organic components of the nanocomposite.

5.2.2 “Grafting-from” Methods

In the previous section, surfactant polymers/oligomers or small molecules formed the organic layer on the surface of inorganic particles via charged or polar interactions to facilitate the dispersion of BaTiO₃ in various polymer matrices. However, the adsorption/desorption equilibrium of the organic molecules at the inorganic surface usually prevents the formation of a robust and permanent polymer shell and leads to increased current leakage and lowered breakdown voltage when the ratio of inorganic particles in the polymer

matrix is high as well as gradually over time.²²⁶ The stability of such approaches is also generally limited as the particles gradually aggregate over time. One way to alleviate this problem is to perform *in-situ* polymerizations which afford simple, low-cost and more stable means of dispersing particles within polymer matrices.²²⁹ To further improve the inorganic-organic interfacial stability, core@shell-structured nanoparticles dispersed in polymer nanocomposites have been widely investigated using different grafting-from polymerization techniques.²²⁰

Recently, a novel strategy known as surface-initiated reversible addition-fragmentation chain transfer polymerization (SI-RAFT) was used to improve the interface between the ferroelectric polymer poly(vinylidene difluoride-co-hexafluoro propylene (P(VDF-HFP))) and BaTiO₃ nanoparticles.²²⁸ In this work, the surface of BaTiO₃ was functionalized with a fluoropolymer called 1H,1H,2H,2H-heptafluorodecyl acrylate (PHFDA) to form a core-shell BaTiO₃-PHFDA nanocomposite (**Figure 39**). Subsequently, the core@shell nanoparticles were mixed with the ferroelectric polymer P(VDF-HFP) to achieve a high dielectric permittivity nanocomposite. Owing to the favorable interaction between the PHFDA surface polymers and the P(VDF-HFP) polymer matrix (*i.e.* both fluoropolymers), the BaTiO₃ nanoparticles exhibited good dispersion and high quality interfaces with the polymer matrix. Using this approach, both high energy densities and low dielectric losses were observed. In the case of 50% volume fraction of BaTiO₃-PTFEA, the breakdown strength of the nanocomposites was found to be 182 kV mm⁻¹ with a maximum energy density of 6.23 J cm⁻³ (a 50% increase relative to pure P(VDF-HFP)). The breakdown strength does decrease with increased particle loading. However, the decrease levels off at around 182 kV mm⁻¹ whereas the maximum energy density continues to rise. The advantage of this SI-RAFT technique is that it makes tuning the shell thickness and grafting density very simple as all this requires is longer reaction times and higher ratios of polymer surface initiator. Consequently, this allows performance properties to be easily adjusted.²²⁸

Marks *et al.* reported an *in-situ* polymerization technique to synthesize BaTiO₃/polypropylene nanocomposites.²²⁹ To build a perfect interfacial region between BaTiO₃ nanoparticles and the polymer matrix, a shell of Al₂O₃ was first coated on the surface of the BaTiO₃ nanoparticles to accommodate the large permittivity contrast between the BaTiO₃ nanoparticles ($\epsilon_r \sim 50-6000$) and the polypropylene ($\epsilon_r \sim 2.25$). Next, a metallocene catalyst ([*rac*-ethylenebisindenyl]zirconium dichloride (EBIZrCl₂)) was adhered to the Al₂O₃-coated BaTiO₃ nanoparticles and in the process activated. *In-situ* polymerization of isotactic polypropylene from the nanoparticle surfaces effectively prevented aggregation to yield well-dispersed nanoparticles in the nanocomposite. The nanocomposites showed leakage currents on the order of 10⁻⁷ to 10⁻⁹ A/cm² at a field strength of 10 kVmm⁻¹. They also showed low dielectric losses over the 100 Hz to 1 MHz frequency range. These performance properties, coupled with the inexpensive materials makes propylene-grafted Al₂O₃-coated BaTiO₃ nanocomposites highly attractive for energy storage devices.

Due to its high thermal and chemical stability, ease of film casting, high mechanical strength and high electrical breakdown strength, polyimide (PI) has been widely investigated as a dielectric material. The synthesis of BaTiO₃-PI nanocomposites has drawn considerable attention in recent years. In contrast to conventional mixing techniques, such as melt mixing and solution mixing, BaTiO₃-PI nanocomposites are prepared by the *in-situ* polymerization of poly(amic acid) (PAmA) followed by the *in-situ* imidization of PAmA to yield BaTiO₃-PI with improved performance.²³⁵ More specifically, this approach can be broken down into four steps. First, the BaTiO₃ nanoparticles are dispersed in a solvent to form a suspension. Second, PAmA is formed by polymerization in the suspension. At this time, PAmA is adsorbed onto the BaTiO₃ nanoparticle surfaces forming core@shell structures that do not aggregate within the PI matrix (**Figure 40a-b**). Third, films are cast on clear glass plates. Lastly, the PAmA is converted to PI by thermal imidization. The solvent is also driven off at this step to yield the final PI matrix containing well-dispersed BaTiO₃. Results show a fairly high breakdown

strength for the composites (67 kVmm^{-1}). This is likely a result of the formation of the core@shell-like structure which supports the homogeneous dispersion of BaTiO_3 particles in the matrix as well as minimized the presence of voids in the nanocomposite. **Table 2** summarizes the examples listed above.

Table 2. Summary of BaTiO_3 -polymer nanocomposites : preparation method and their dielectric properties

BaTiO ₃	Polymer Matrix	Method	Dielectric constant	Breakdown Strength	References
PFBPA-BaTiO ₃ nanoparticle, 30-50 nm	P(VDF-HFP)	<i>Grafting-to</i>	$\epsilon_r = 37 \pm 2$ at 1 kHz (50% filler)	$210 \pm 50 \text{ kVmm}^{-1}$	106
BaTiO ₃ nanoparticles	PVDF	<i>Grafting-to</i> : a silane coupling agent act as a bridge between the filler and the polymer matrix	$\epsilon_r = 50$ at 100 kHz (40% filler), loss tangent < 0.05 below 100 kHz	-	219
BaTiO ₃ particles	TEGDA TMPTA TDDMA	<i>Grafting-to</i> : photopolymerization	dielectric losses of the composites increases in the order of TDDMA $<$ TMPTA $<$ PEGDA	-	231
Silica-coated BaTiO ₃ nanoparticles, 30-40 nm	Polyimide	<i>Grafting-to</i> : dispersion polymerization method	-	-	233
Titanate-coated BaTiO ₃ nanoparticles	PVDF	<i>Grafting-to</i> :	$\epsilon_r = 30$ at 1 kHz (22% filler)	250 kVmm^{-1}	234
BaTiO ₃ nanoparticles	P(VDF-HFP)	<i>Grafting-from</i> : SI-RAFT	$\epsilon_r = 45$ at 1 kHz (50% filler)	182 kV mm^{-1}	228
Al ₂ O ₃ -coated BaTiO ₃ nanoparticles, Al ₂ O ₃ coating ~ 10nm,	polypropylene	<i>Grafting-from</i> : <i>In-situ</i> polymerization	$\epsilon_r = 18$ at 1 kHz (40% filler)	10 kVmm^{-1}	229
BaTiO ₃ nanoparticles	polyimide	<i>Grafting-from</i> : <i>In-situ</i> polymerization	$\epsilon_r = 20$ at 10^3 – 10^6 Hz (40% filler)	67 kVmm^{-1}	235

6. General Observations and Future Outlook

The controlled synthesis and characterization of BaTiO_3 at low dimensions, including BaTiO_3 -containing composites, has had a profound influence on the current trend toward the greater miniaturization of BaTiO_3 -based electronic devices. This review summarizes the most recent progress in three key aspects of BaTiO_3 nanomaterials. First, chemical synthesis methods for producing high-quality BaTiO_3 nanocrystals are presented. Second, the dielectric and ferroelectric properties of BaTiO_3 nanocrystal clusters and individual BaTiO_3

nanocrystals are investigated using both theoretical modeling and piezoresponse force microscopy (PFM). Lastly, viable BaTiO₃ surface functionalization strategies for realizing BaTiO₃/polymer nanocomposites with high energy storage densities are presented.

Despite the significant progress made so far in the controlled synthesis of BaTiO₃ nanocrystals with well-defined morphologies (e.g, nanodots, nanorods, nanocubes and nanowires) and crystal structures (e.g., cubic, tetragonal), they are still of lower quality in comparison to other well-established nanomaterials such as metals and semiconductors. For example, one-dimensional BaTiO₃ nanostructures (e.g., nanowires and nanorods) still have large size distributions and poorly controlled morphologies (Section 3). As discussed previously, these one-dimensional structures are more promising building blocks for realizing nanoscale electronic,⁸⁷ optical,²³⁶ and mechanical²³⁷ devices as they retain wire-like connectivity and efficiently transfer the stress, charge and heat throughout the system. It is clearly challenging to realize one-dimensional BaTiO₃ nanostructures. However, certain crystal growth mechanisms, such as orientated attachment,²³⁸⁻²⁴⁰ and catalyst-assisted growth,^{241, 242} are promising for producing high-quality one-dimensional nanostructures. This has yet to be explored. Moreover, other interesting anisotropic nanostructures are of great scientific and technological interest including tetrapods^{243, 244} and hyperbranched nanocrystals.²⁴⁵ These have also not yet been reported. With continued progress in soft chemical techniques, more high quality one dimensional nanostructures may be produced.

Another important area requiring extensive research is the tailoring of the crystal structure of BaTiO₃ to push its critical size to even smaller values. The critical size of BaTiO₃ currently reported is 50 nm, below which BaTiO₃ nanocrystals are in the cubic phase that lacks ferroelectric properties. The size effect thus limits the utilization of BaTiO₃ in high-density energy/information storage. Based on the core-shell model (Section 2),^{75, 76} the surface chemistry and structure can also influence the ferroelectric behavior of the nanocrystals.⁵⁷ Thus, it is feasible to convert the cubic structure into the tetragonal phase at low dimensions

through surface engineering such as ligand modification and second phase coating. Various techniques, including ligand modification,¹⁰⁴ metal coating,¹⁰⁷ and template confinement,⁵⁷ have proven effective for suppressing the presence of the cubic phase. However, these strategies are still far from seeing use in practical applications and a clear understanding of the basic mechanisms remains unclear. With progress in characterization techniques, especially those capable of probing the local structure and properties such as scanning probe techniques,²⁴⁶⁻²⁴⁸ near-field Raman spectra,²⁴⁹⁻²⁵² and atomic probe microscopy,^{253, 254} it is likely that a systematic understanding of the effects of surface modification on ultimate crystal structure and dielectric properties can be realized. This in turn will provide the guidance to develop new strategies for improving device performance by preserving the ferroelectric properties at smaller sizes (5–15 nm based on theoretical predictions).²⁵⁵

In addition, current work on BaTiO₃-polymer nanocomposite systems mainly uses strongly binding modifiers to improve the dispersion of BaTiO₃ nanocrystals within polymer matrices. While there are limited works reporting on directly grafting high molecular weight polymers onto the BaTiO₃ surface, it is the most efficient approach to date to obtain dispersions of nanocrystals in polymer matrices. With advances in polymeric grafting techniques, we anticipate rapidly evolving research in this field. Various types of interesting dielectric polymers, such as PVDF and PI, can be directly grafted onto the BaTiO₃ surface. Different kinds of grafting chemistry will also be developed to enable strong chemical bonding for improved performance (*i.e.*, reduced leakage current and higher breakdown voltage). Additionally, the interaction between polymers and BaTiO₃ nanocrystals in nanocomposites is usually weak, particularly in the solution state. Owing largely to the adsorption-desorption dynamics of surface grafting,²⁵⁶ large-scale phase separation can occur after long-time storage or with various post treatments. One way to address these concerns is the template approach. This technique employs amphiphilic block copolymers to guide the growth of nanocrystals. We envision that microphase-separated structures and/or micelles of

amphiphilic diblock copolymers composed of a hydrophilic block and hydrophobic dielectric block (e.g., poly(acrylic acid)-*b*-Polyvinylidene fluoride (PAA-*b*-PVDF)) may be exploited as templates to synthesize nanocrystals that are intimately and permanently connected with dielectric polymers due to the strong affinity of inorganic precursors to the hydrophilic block (e.g., PAA).⁵⁰ Importantly, since the two blocks in the amphiphilic block copolymer templates are covalently linked, the resulting nanocomposites⁵⁰ are expected to be much more stable than those prepared by direct grafting strategies that rely on the coordination interaction between nanocrystals and ligand functional groups.

Acknowledgements

We gratefully acknowledge the support from the National Science Foundation (NSF CMMI 1562075 and DMR 1709420) and the Airforce Office of Scientific Research (AFOSR; FA9550-16-1-0187).

Figures and Figure Captions

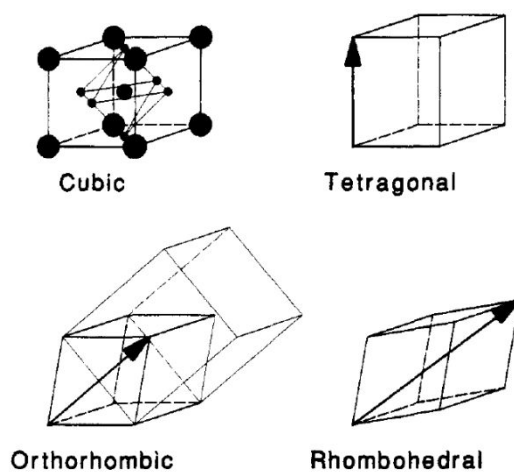


Figure 1. Schematic representation of the four different crystalline structures of BaTiO₃. Among them, the cubic phase is paraelectric, while the tetragonal, orthorhombic and rhombohedral phases are ferroelectric. Reproduced with permission.³⁰ Copyright 1993, American Chemical Society.

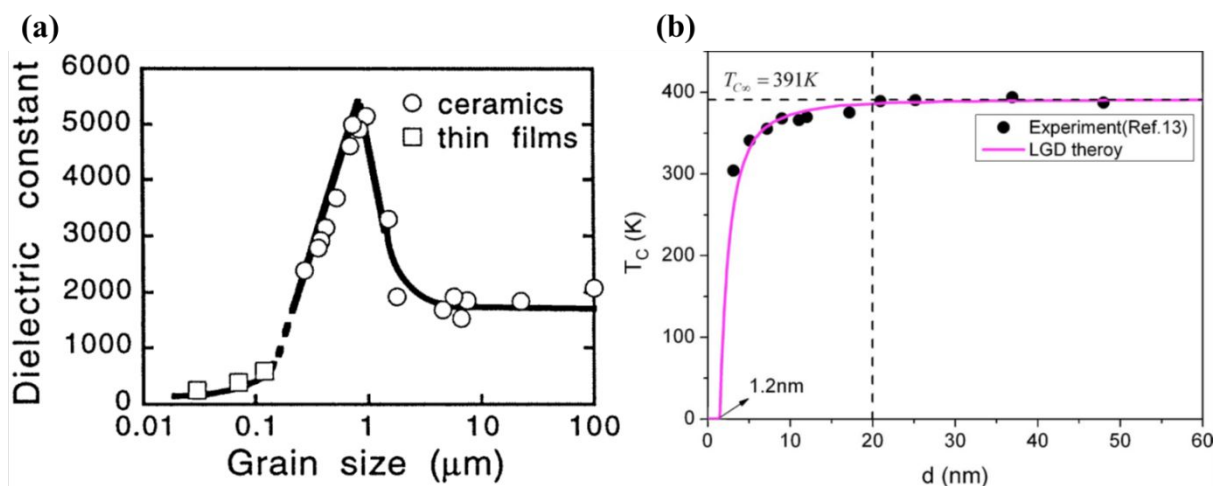


Figure 2. (a) Dielectric constant of BaTiO₃ ceramics and thin films for samples with different grain size. Reproduced with permission.⁸⁸ Copyright 1998, IOP Publishing Ltd; (b) Size effect of the Curie temperature. Reproduced with permission.⁸⁹ Copyright 2008, American Institute of Physics.

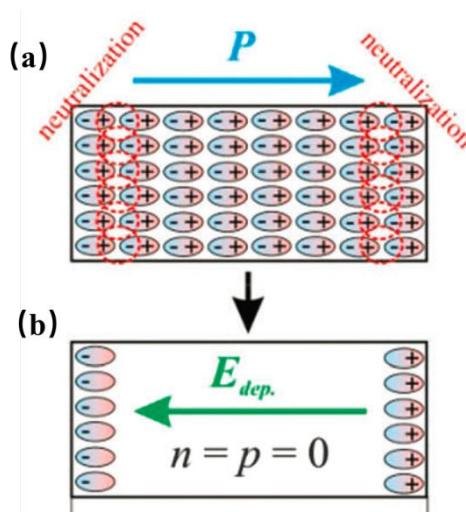


Figure 3. (a) Schematic representation of an uncompensated ferroelectric material with fixed surface charges. (b) Schematic representation of the depolarization field inside the ferroelectric material induced by the surface charge with the depolarization field pointing against the direction of self-polarization P . Reproduced with permission.¹⁰² Copyright 2015, the Owner Societies.

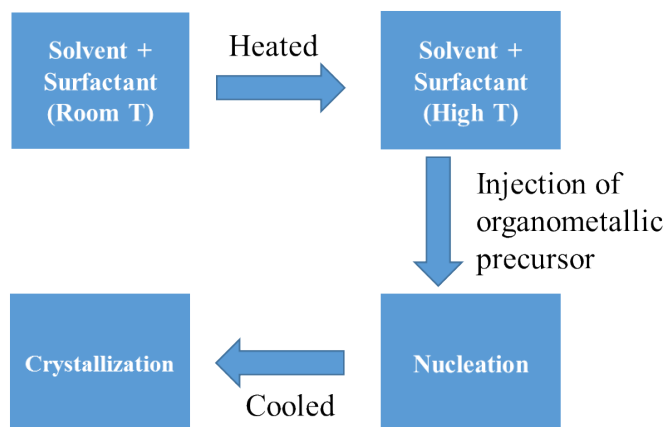


Figure 4. Simply graphical representation of typical organometallic method, which separates the nucleation process and growth process.

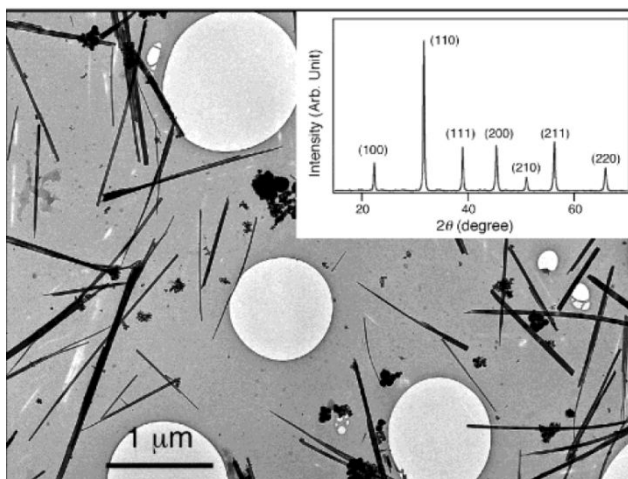


Figure 5. TEM image of BaTiO₃ nanorods synthesized by a thermal decomposition method. Inset: Powder XRD pattern of the randomly-oriented BaTiO₃ nanorods. Reproduced with permission.⁵⁴ Copyright 2002, American Chemical Society.

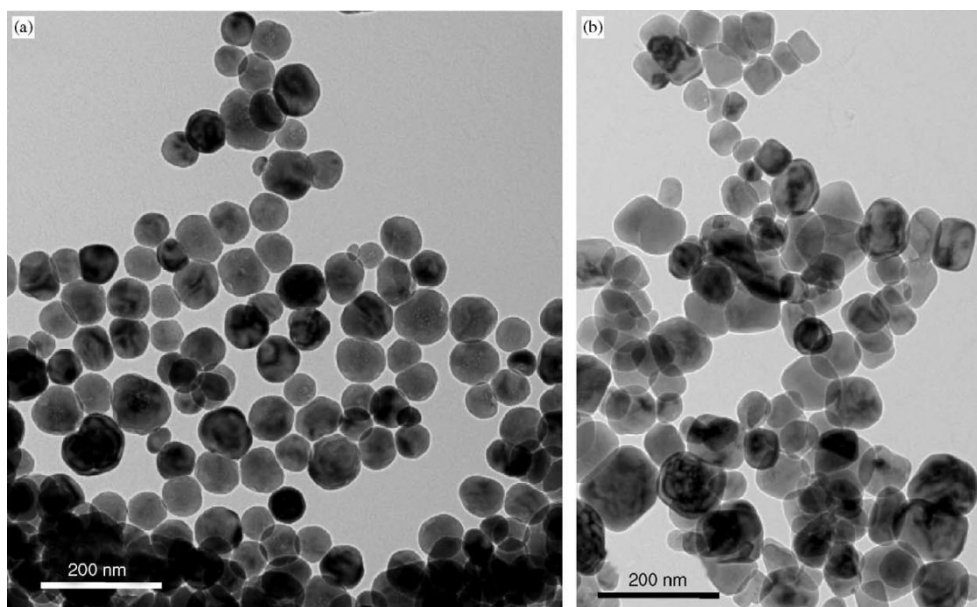


Figure 6. TEM images of BaTiO₃ nanocrystals with different morphologies synthesized under the same hydrothermal conditions but with different starting materials. (a) Sample A produced with titanium hydroxide (Ti(OH)₄) and barium hydroxide (Ba(OH)₂)·8H₂O as starting materials. (b) Sample B produced from titanium dioxide (TiO₂) and barium hydroxide (Ba(OH)₂)·8H₂O. Reproduced with permission.¹⁵³ Copyright 2005, Elsevier.

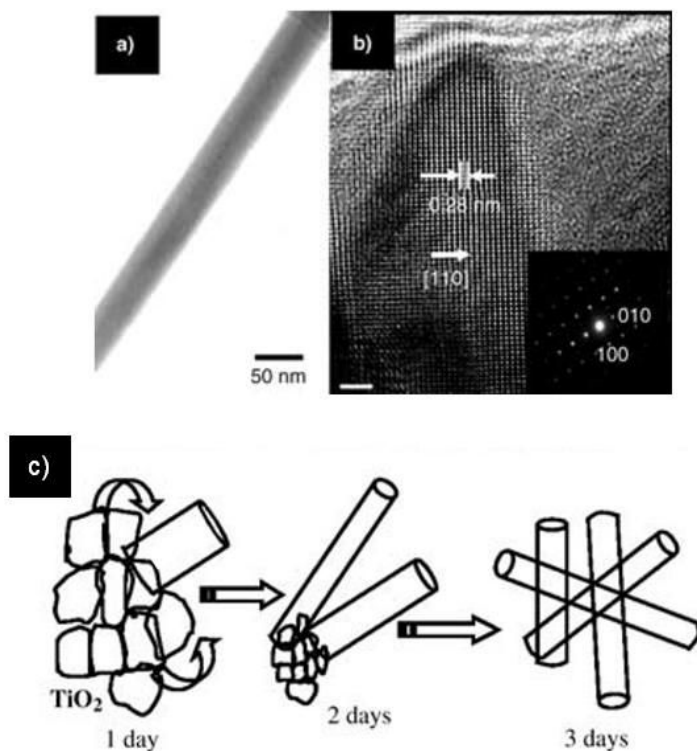


Figure 7. (a) Typical TEM image of a BaTiO₃ nanowire; (b) HRTEM image of the tip of a BaTiO₃ nanowire, the clear lattice fringes indicate that the entire BaTiO₃ nanowire is a single crystal. Scale bar equals 2 nm. (c) A graphical representation of the growth mechanism of BaTiO₃ nanowires produced from TiO₂ nanoparticles via a hydrothermal method. Reproduced with permission.⁴⁸ Copyright 2005, Wiley.

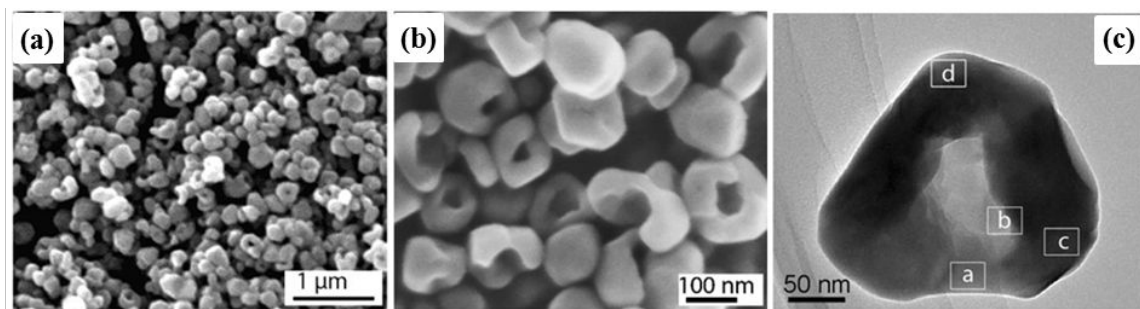


Figure 8. (a) and (b) SEM images of bowl-like BaTiO₃ nanoparticles with concave centers; (c) HRTEM image of a bowl-like BaTiO₃ nanoparticle which shows an empty center. Reproduced with permission.⁵¹ Copyright 2010, Springer.

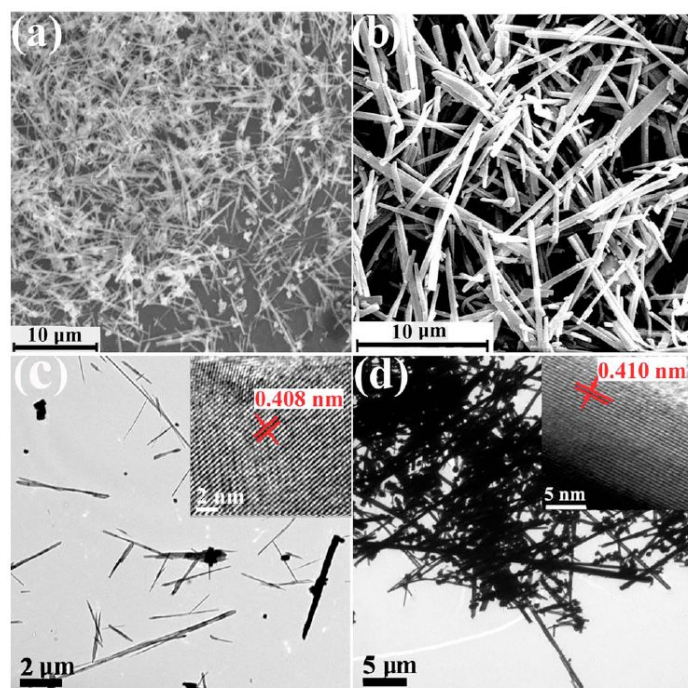


Figure 9. SEM images of (a) $\text{Na}_2\text{Ti}_3\text{O}_7$ nanowires and (b) $\text{K}_2\text{Ti}_4\text{O}_9$ nanowhiskers sacrificial templates for producing BaTiO_3 nanowires. (c) TEM image of hydrothermally prepared BaTiO_3 nanowires prepared using $\text{Na}_2\text{Ti}_3\text{O}_7$ nanowire templates (Inset: HRTEM image shows the lattice fringes of the templated BaTiO_3 nanowires); (d) TEM images of BaTiO_3 nanowires prepared using $\text{K}_2\text{Ti}_4\text{O}_9$ nanowhiskers as templates (Inset: HRTEM image showing the lattice fringes of BaTiO_3). Reproduced with permission.⁵² Copyright 2009, American Institute of Physics.

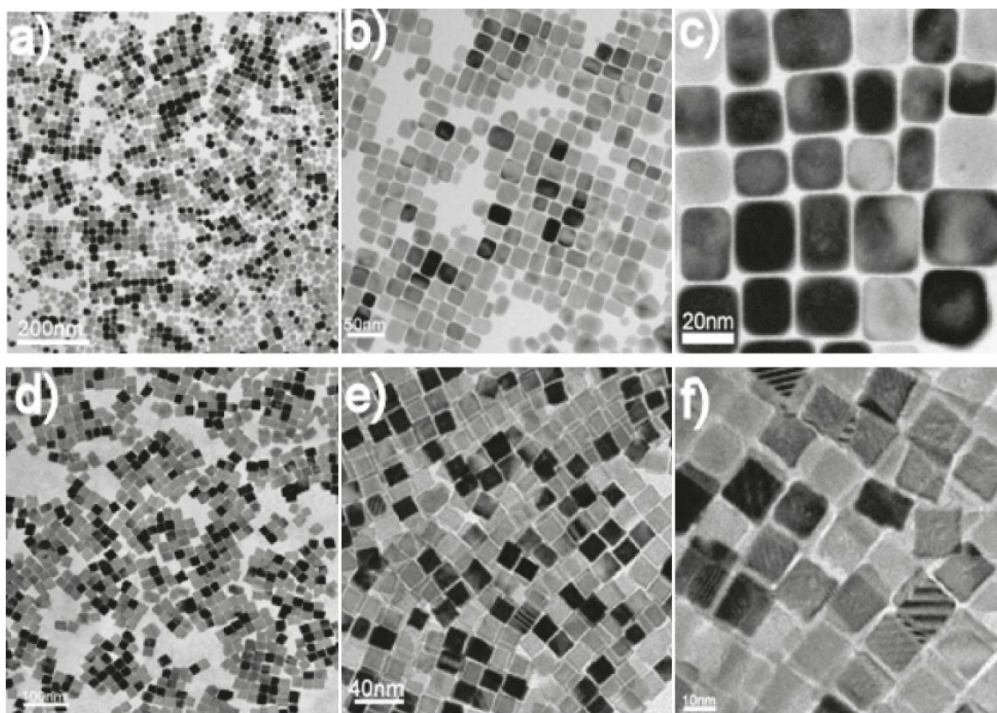


Figure 10. TEM images of (a-c) cubelike and (d) cubic BaTiO_3 nanoparticles with each forming monolayers due to the assembly of BaTiO_3 nanoparticles; (e-f) BaTiO_3 nanoparticles assembled into bilayer structures at different magnifications. Reproduced with permission.⁵³ Copyright 2010, American Chemical Society.

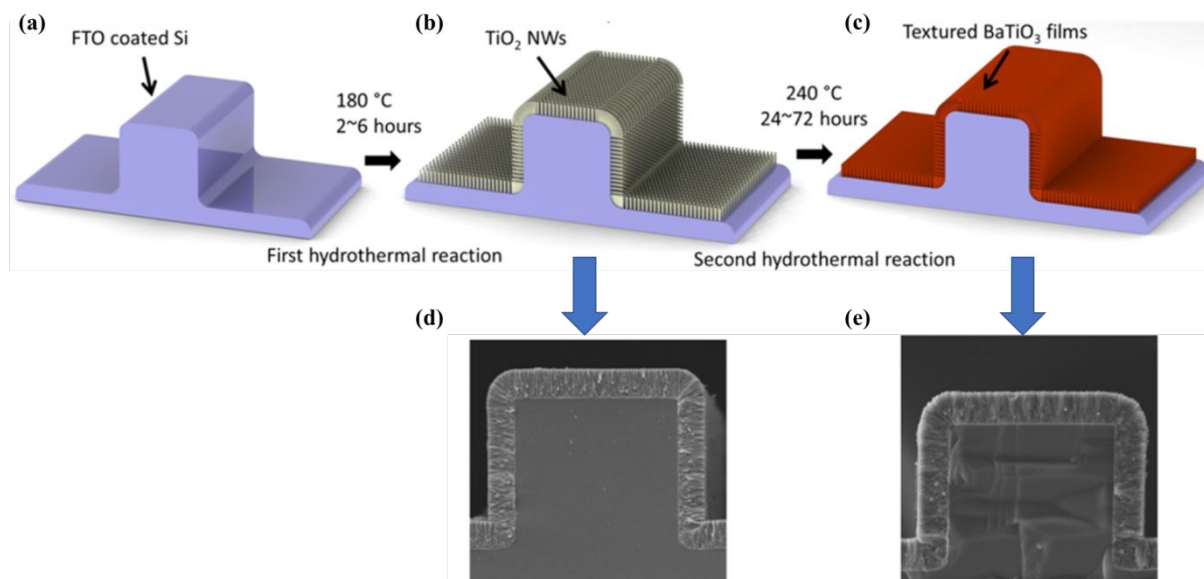


Figure 11. (a)-(c) Schematic illustration of the strategy to grow conformal BaTiO₃ films. SEM images of (d) conformal TiO₂ NW arrays on FTO coated silicon wafers and (e) conformal BaTiO₃ films.¹⁵⁸ Copyright 2016, American Chemical Society.

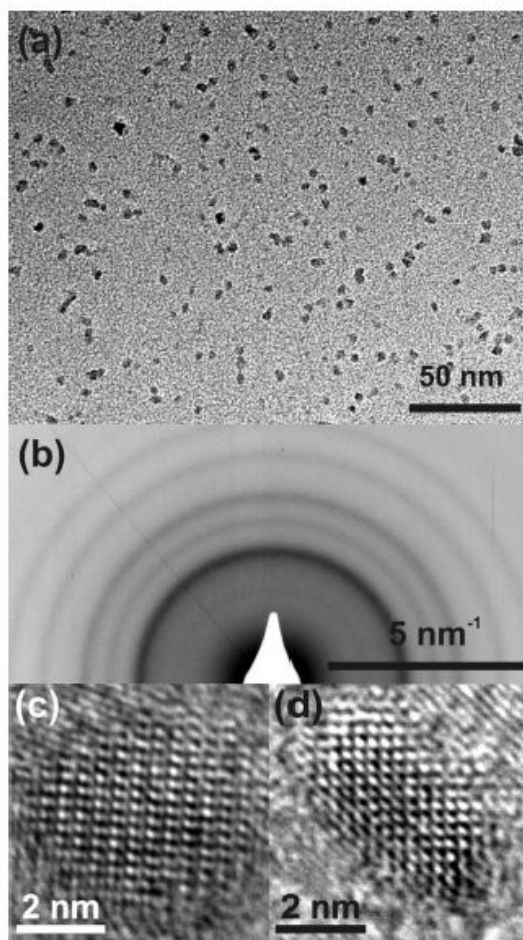


Figure 12. (a) TEM image of synthesized BaTiO_3 nanoparticles exhibiting good uniformity and no aggregation; (b) selected area electron diffraction (SAED) of synthesized BaTiO_3 nanoparticles; (c) and (d) HRTEM images of individual BaTiO_3 nanoparticles confirming that each isolated nanoparticle is a single crystal. Reproduced with permission.¹⁵⁹ Copyright 2004, American Chemical Society.

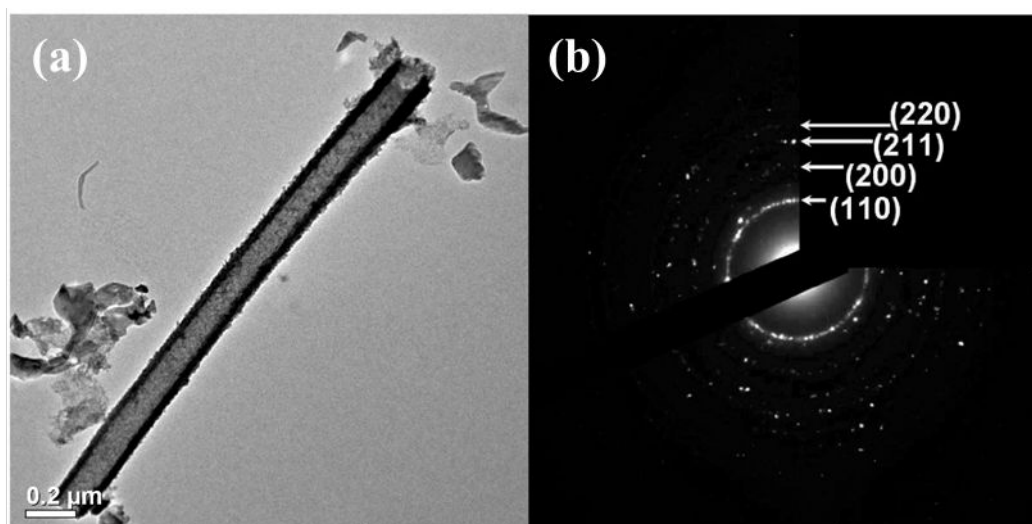


Figure 13. (a) Bright-field TEM image, and (b) selected area electron diffraction (SAED) of an isolated BaTiO₃ nanotube fabricated from an AAO template under near-ambient conditions. Reproduced with permission.¹⁷² Copyright 2009, American Chemical Society.

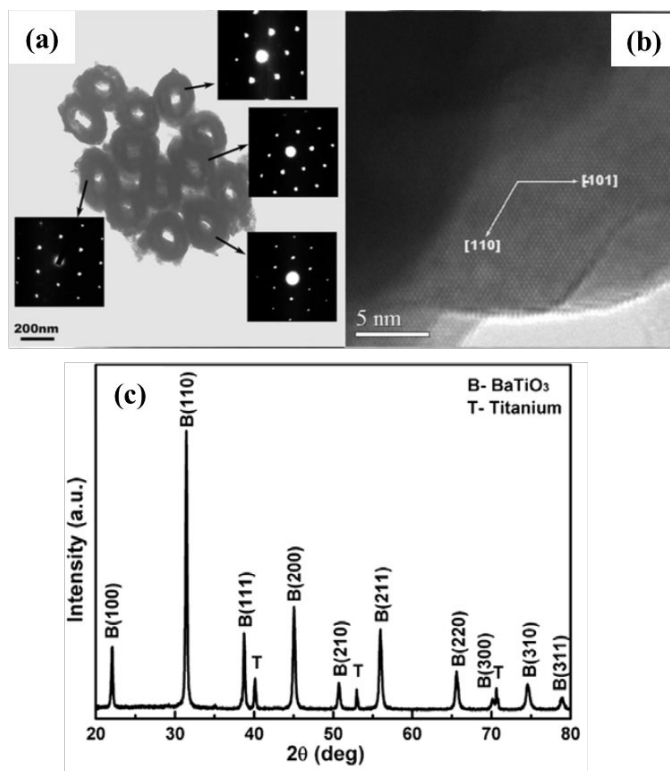


Figure 14. (a) top-view TEM images of BaTiO₃ nanotubes with SAED patterns in the insets; (b) HRTEM image of BaTiO₃ nanotube; (c) XRD pattern of BaTiO₃ nanotube arrays.⁹³ Copyright 2009, IOP science..

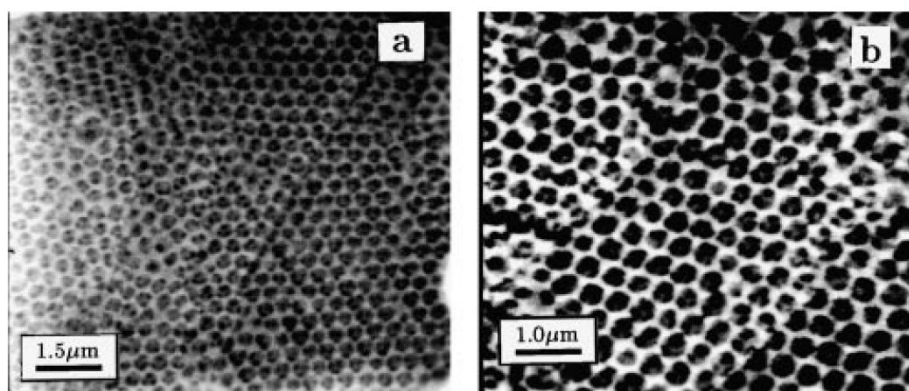


Figure 15. (a) and (b) SEM images of macroporous BaTiO₃ layers produced using ordered arrays of PS spheres as templates. Reproduced with permission.¹⁷⁶ Copyright 2000, Royal Society of Chemistry.

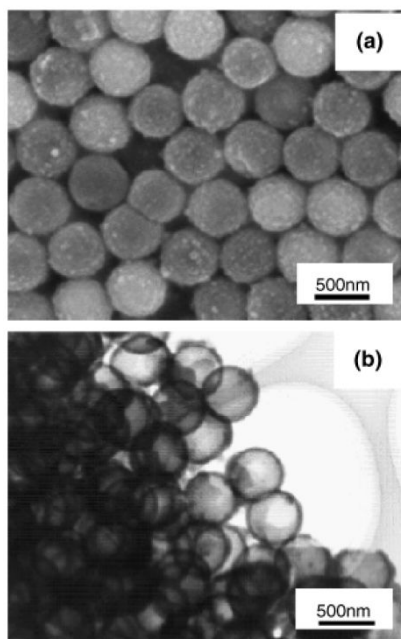


Figure 16. (a) TEM micrographs of PMMA spheres coated with titanate nanoparticles; (b) SEM image of hollow BaTiO₃ spheres. Reproduced with permission.⁵⁶ Copyright 2006, Wiley.

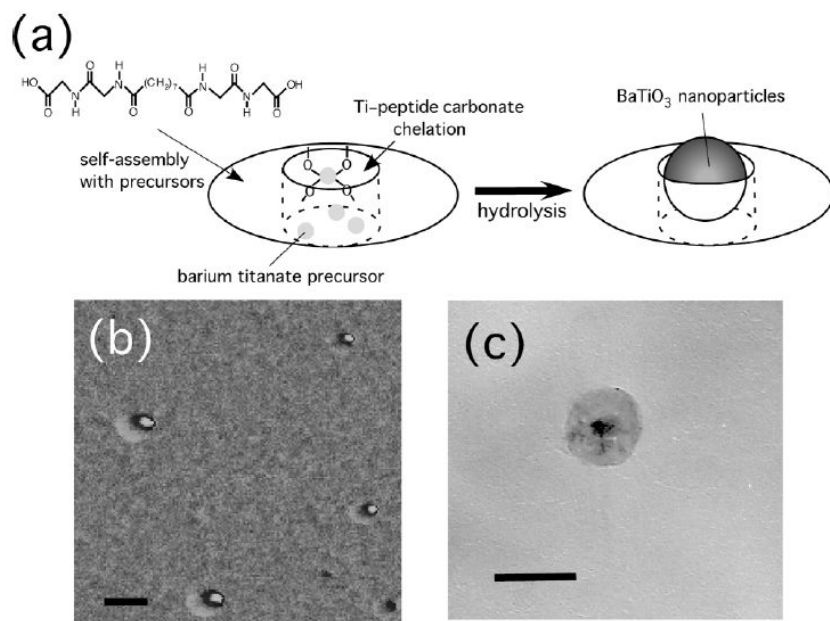


Figure 17. (a) Illustration of the growth process for BaTiO₃ nanoparticles using self-assembled peptide templates; (b) AFM and (c) TEM images showing BaTiO₃ nanoparticles inside the peptide nanoring template (scale bars for (b) and (c) are 50 nm and 60 nm, respectively). Reproduced with permission.⁵⁷ Copyright 2006, Wiley.

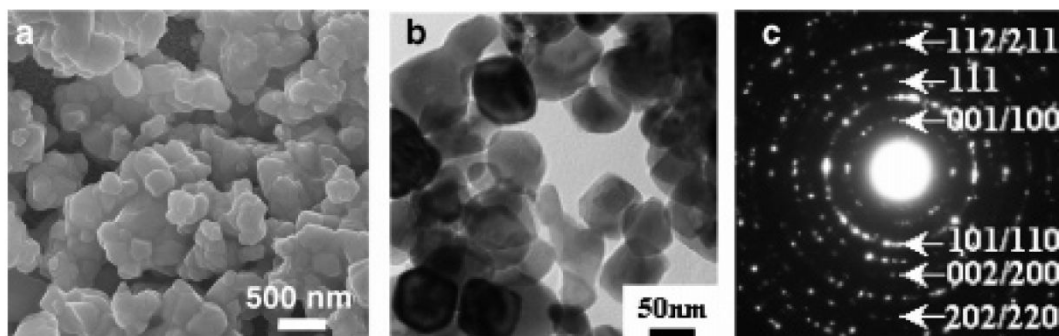


Figure 18. (a) SEM and (b) TEM images of BaTiO_3 nanoparticles, (c) SAED pattern of the precipitated BaTiO_3 nanoparticles. Reproduced with permission.²⁸ Copyright 2008, American Chemical Society.

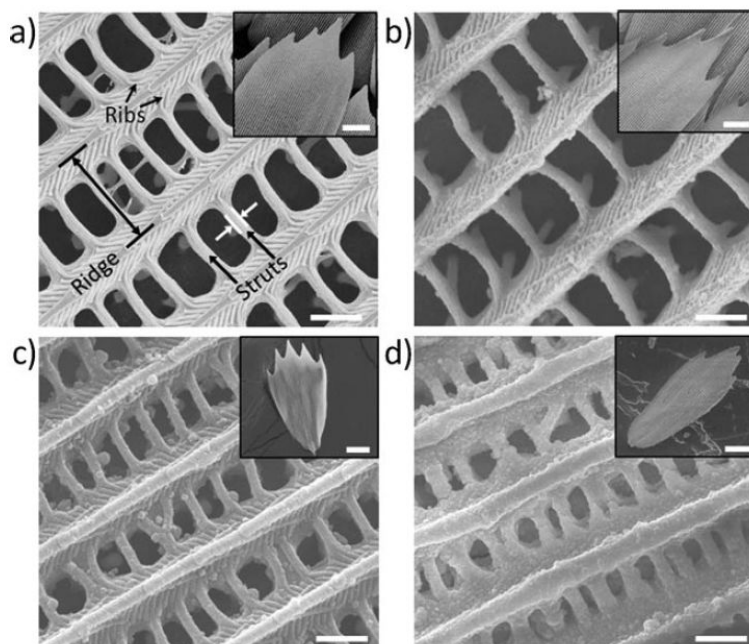


Figure 19. SEM images of the wing scales from the Morphohelenor butterfly wing at various stages of conversion: (a) the untreated Morphohelenor butterfly wing as the starting template, (b) the scale coated with titania-bearing precursors, (c) the coated scale after pyrolysis, and (d) the final BaTiO₃ scale obtained by hydrothermal reaction. The insets show the low magnification images of each corresponding scale. Scale bars represent 1 mm in (a-d) and 20 μm in the insets. Reproduced with permission.¹⁷⁷ Copyright 2010, Wiley.

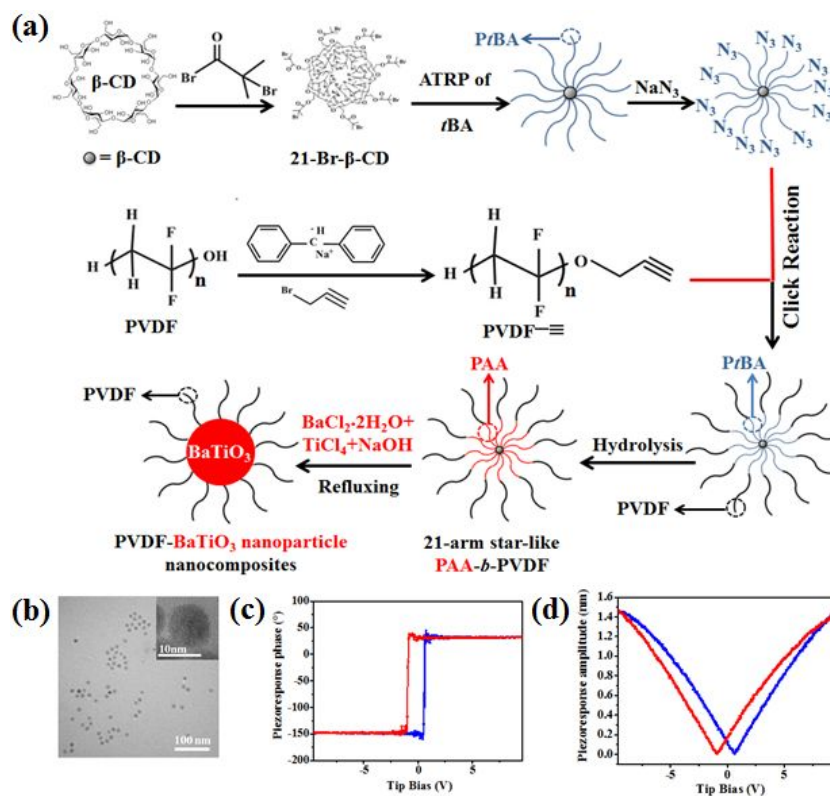


Figure 20. (a) Scheme of the synthetic strategy for preparing BaTiO₃ nanoparticles by the nanoreactor approach. The amphiphilic star-like PAA-*b*-PVDF copolymer serves as the nanoreactor. (b) TEM images of templated BaTiO₃ nanoparticles demonstrating good uniformity with average diameters of 10 nm; (c) and (d) PFM results of individual BaTiO₃ nanoparticles with measured hysteresis loops signifying the switching behavior of the ferroelectric BaTiO₃ nanoparticles.⁵⁰ Copyright 2015, American Chemical Society.

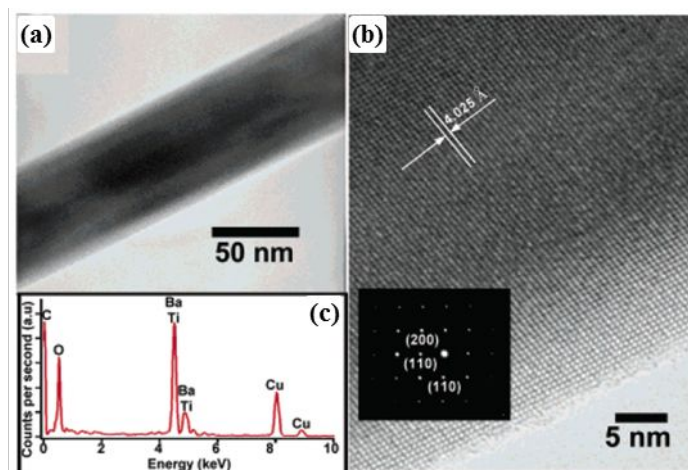


Figure 21. (a) TEM and (b) HRTEM images of a single BaTiO₃ nanowire, the inset in (b) displays the selected area electron diffraction (SAED) pattern of the BaTiO₃ nanowire; (c) EDS spectrum of the as-prepared BaTiO₃ nanowires. Reproduced with permission.¹⁸⁹ Copyright 2003, American Chemical Society.

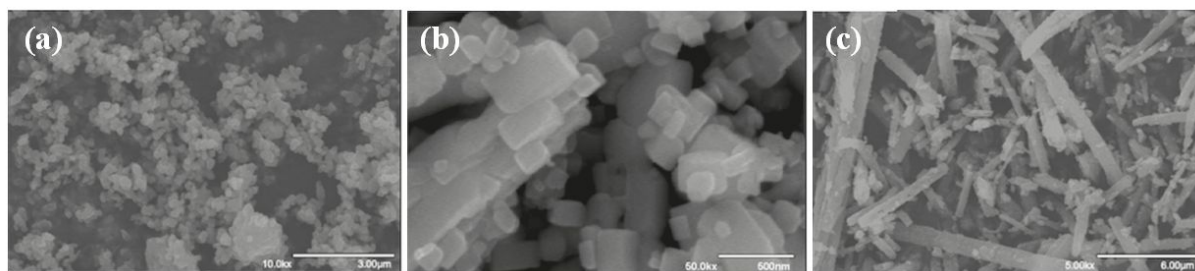


Figure 22. SEM images of three different products: (a) spherical, (b) cubic, and (c) rod shaped BaTiO₃ nanocrystals synthesized using a surfactant-free molten salt method. Reproduced with permission.⁵⁸ Copyright 2009, American Chemical Society.

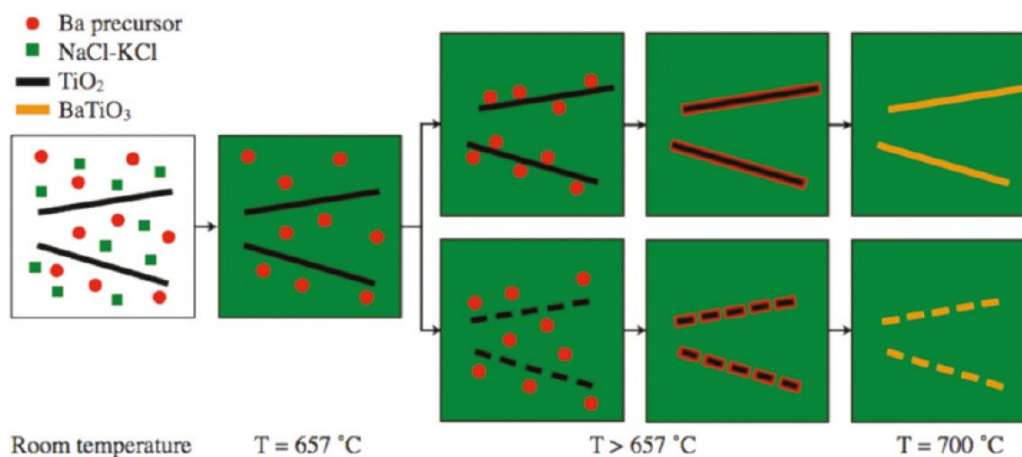


Figure 23. Proposed synthetic mechanism for rod-shaped and cube-shaped BaTiO₃ in a molten salt. The upper panels are for rod-shaped BaTiO₃, and the bottom panels are for cube-shaped BaTiO₃. The difference in the two mechanisms hinges on the relative rates of dissolution of the barium and titanium precursors. Reproduced with permission.⁵⁸ Copyright 2009, American Chemical Society.

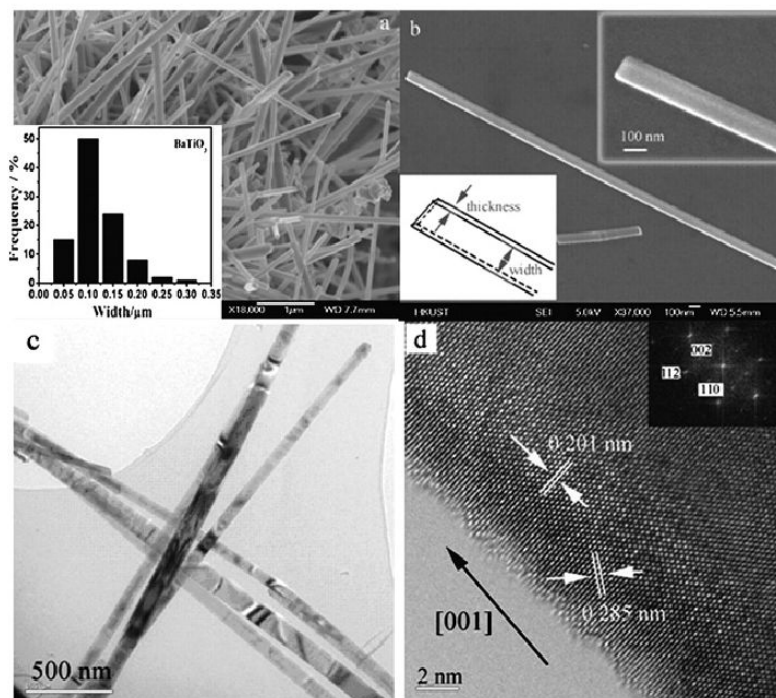


Figure 24. (a) Low and (b) high magnification SEM images of as-prepared BaTiO₃ nanostrips, (c) a typical TEM image of BaTiO₃ nanostrips, (d) HRTEM image of a single BaTiO₃ nanostrip. Reproduced with permission.¹⁹⁰ Copyright 2009, Royal Society of Chemistry.

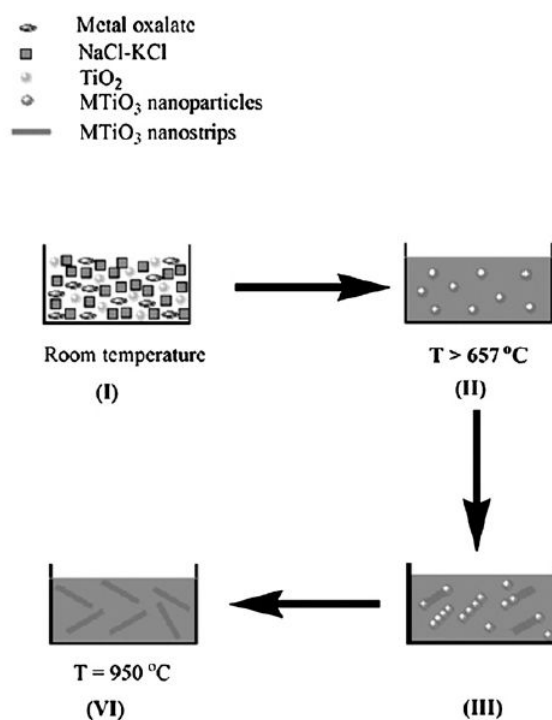


Figure 25. Growth mechanism for MTiO₃ nanostructures (M stands for metal): (I) mixtures are ground at room temperature; (II) NaCl/KCl is melted when the reaction temperature exceeds 657 °C; (III) Small crystal seeds aggregate along a polarization axis to form nanostructures; (VI) the perovskite nanostructures are formed at 950 °C. Reproduced with permission.¹⁹⁰ Copyright 2009, Royal Society of Chemistry.

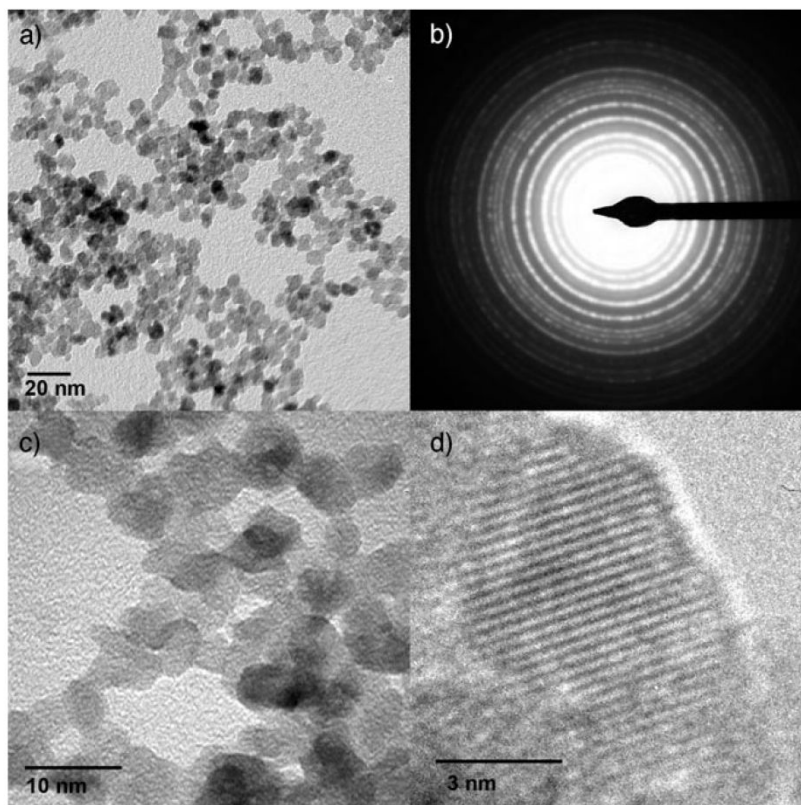


Figure 26. (a), (c) and (d) TEM images of BaTiO_3 nanoparticles formed by a sol-gel approach (different magnifications). (b) SAED pattern of BaTiO_3 nanoparticles. Reproduced with permission.⁶⁰ Copyright 2006, Wiley.

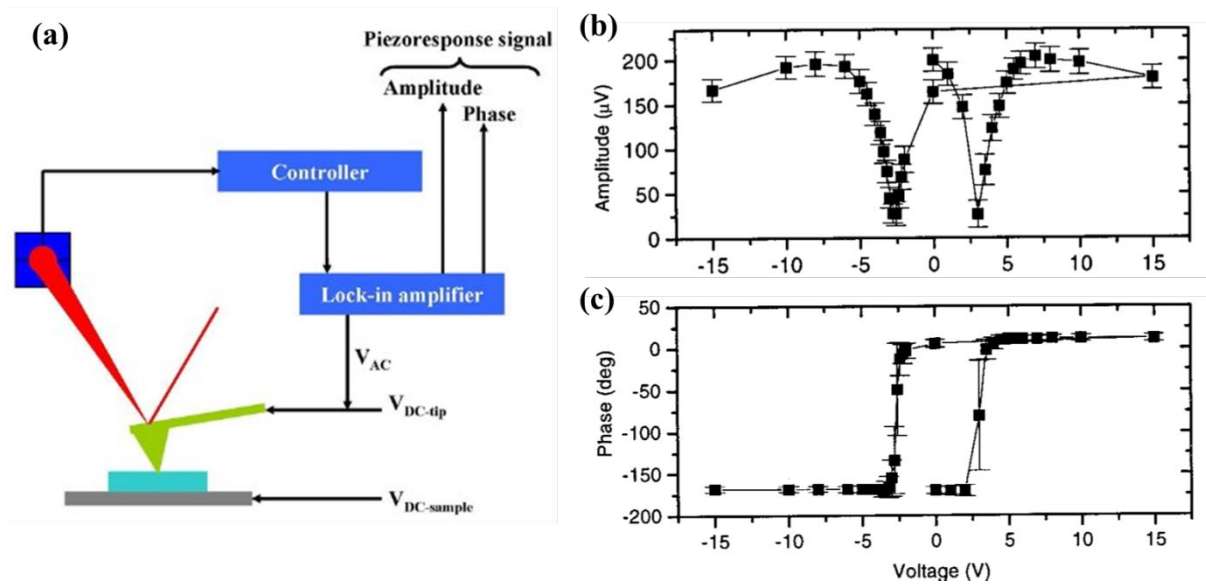


Figure 27. (a) Schematic representation of PFM setup. (b) Amplitude and (c) Phase signals. Reproduced with permission.²⁵⁷ Copyright 2001, American Institute of Physics.

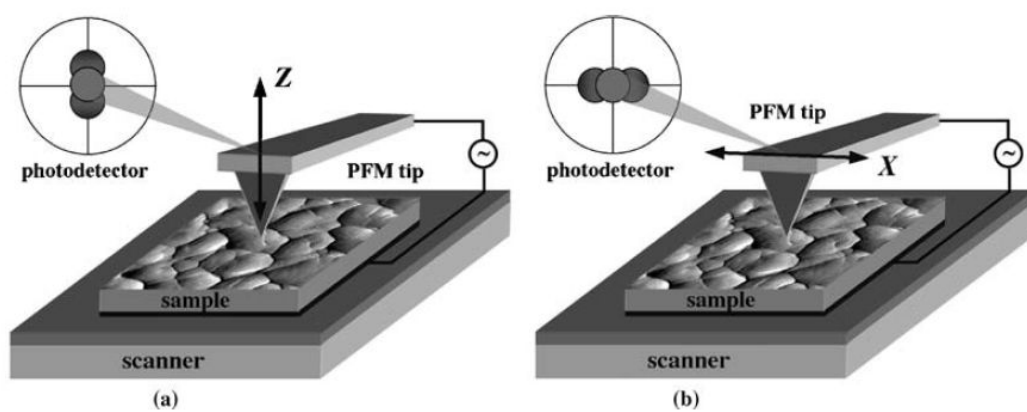


Figure 28. Schematic of piezoresponse force microscopy (PFM) signal detection in the (a) vertical and (b) lateral mode. Reproduced with permission.²⁰⁴ Copyright 2006, Springer.

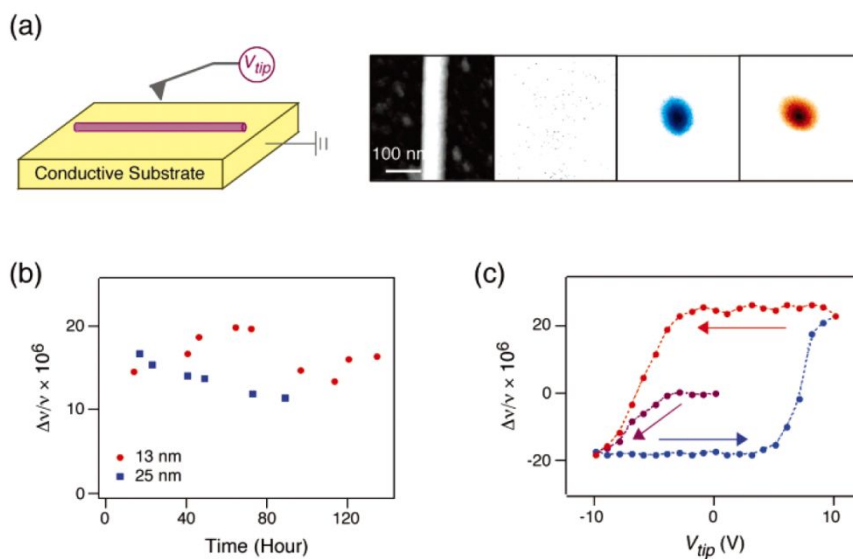


Figure 29. (a) Schematic diagram of the PFM tip and substrate setup. The panels on the right show a topographic image of a BaTiO₃ nanowire and electrostatic force microscopy (EFM) images obtained from the same wire. (b) Plot of the cantilever resonance frequency shift as a function of time for two nanowires with different diameters; 13 nm (circles) and 25 nm (squares). (c) Plot of resonance frequency shift as a function of the writing voltage for a BaTiO₃ nanowire with a 15 nm diameter. Reproduced with permission.²⁰⁶ Copyright 2002, American Chemical Society.

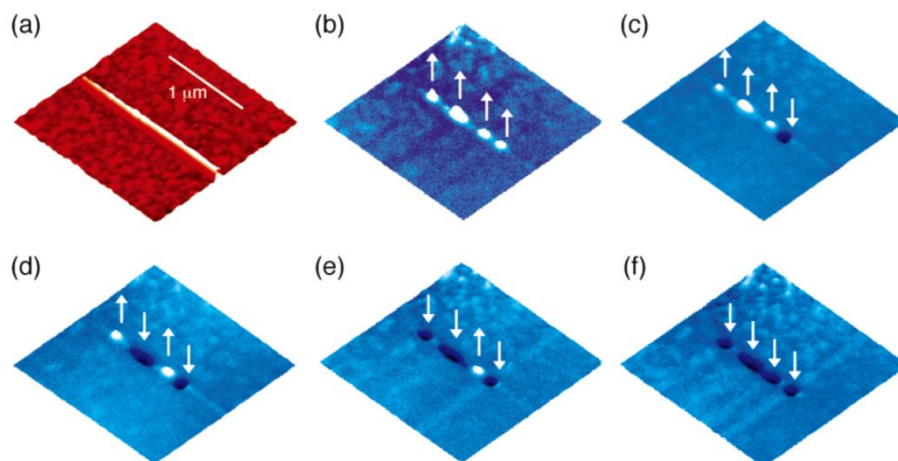


Figure 30. (a) Three-dimensional image of a single BaTiO₃ nanowire, and (b)-(f) successive EFM images showing four separate polarization domains that can be independently adjusted by an external electric field in a fashion analogous to binary. Reproduced with permission.²⁰⁶ Copyright 2002, American Chemical Society.

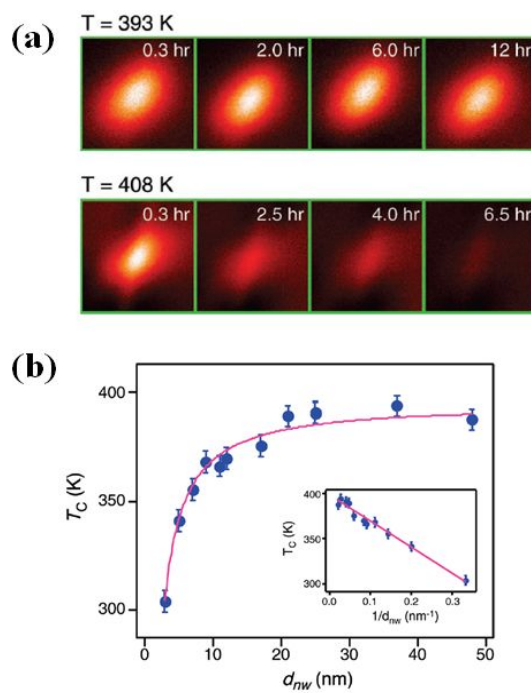


Figure 31. (a) EFM images over time (size: $300 \times 300\text{ nm}^2$) for a 25 nm diameter nanowire after polarization writing below (393 K) and above (408 K) the phase transition temperature; (b) ferroelectric phase transition temperature (T_c) as a function of nanowire diameter. Reproduced with permission.¹⁰⁵ Copyright 2006, American Chemical Society.

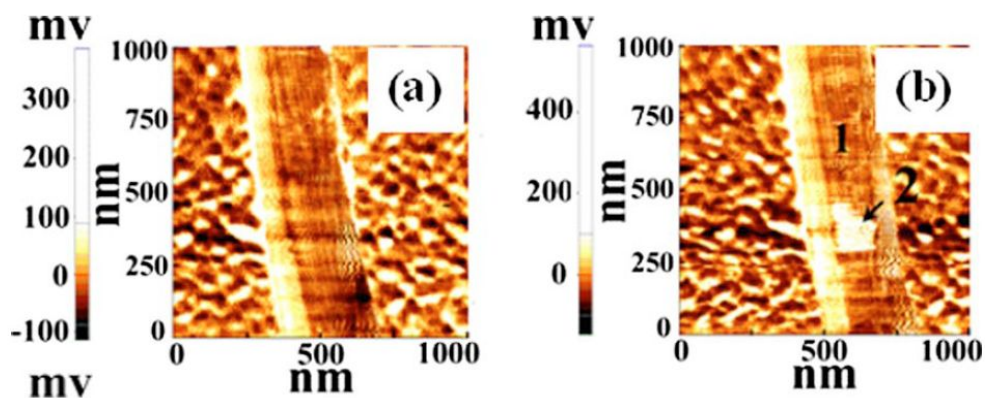


Figure 32. PFM images of a single BaTiO₃ nanowire before (a) and after (b) the poling process (i.e writing step). The PFM signals exhibit two different states with the as-grown state marked as “1” and the single-poled state marked as “2” indicating the presence of a local electric polarization normal to the wire axis. However, due to the existence of bulk hydroxyl defects and oxygen vacancies, the induced polarization slowly decays in air over 12-24 h. Reproduced with permission.⁵² Copyright 2009, American Institute of Physics.

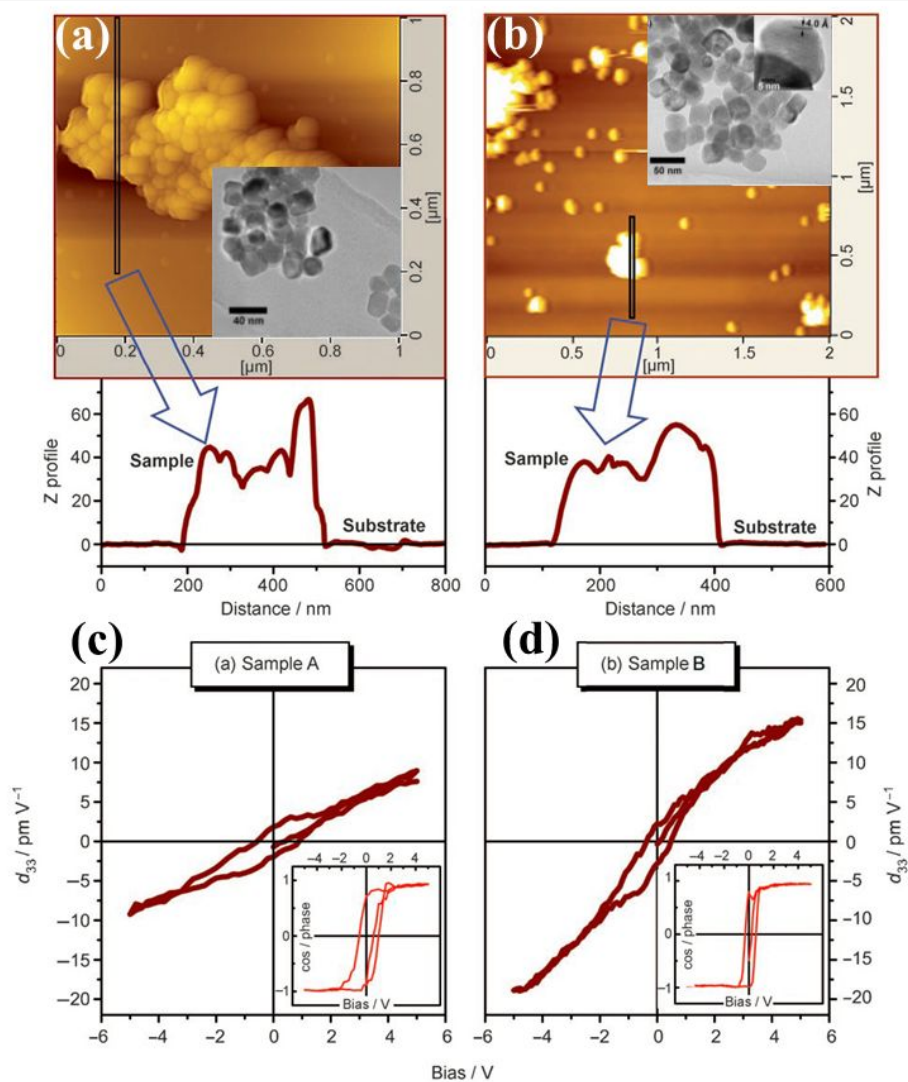


Figure 33. (a) and (b) large-area AFM images along with corresponding thickness profiles of the 25 nm (inset in (a)) and 35 nm (inset in (b)) deposits; (c) and (d) the piezoresponse versus bias voltage curves from the two samples with a clear hysteresis component.²⁰⁷ Copyright 2006, Wiley.

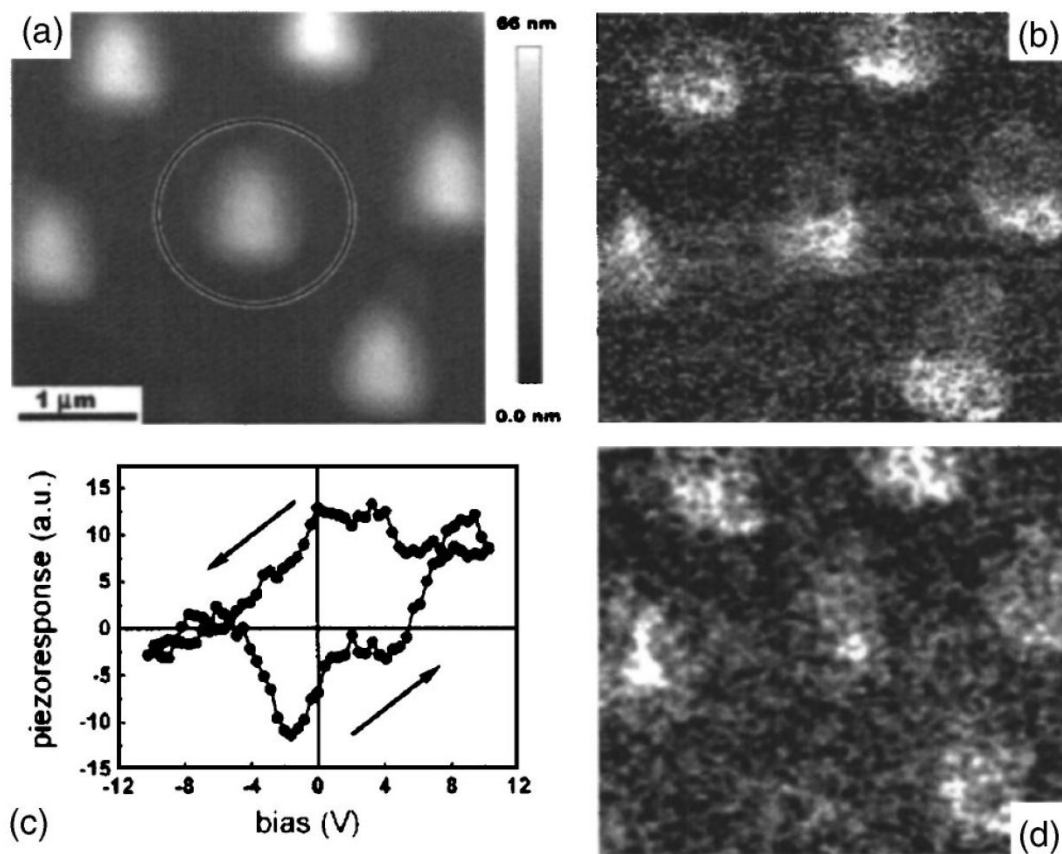


Figure 34. AFM and PFM characterization of a BaTiO₃ nanodot array: (a) topography, (b) ferroelectric domain structure prior to switching, (c) switching piezoresponse hysteresis loop, and (d) ferroelectric domain structure after switching. Reproduced with permission.²⁰⁸ Copyright 2005, American Institute of Physics.

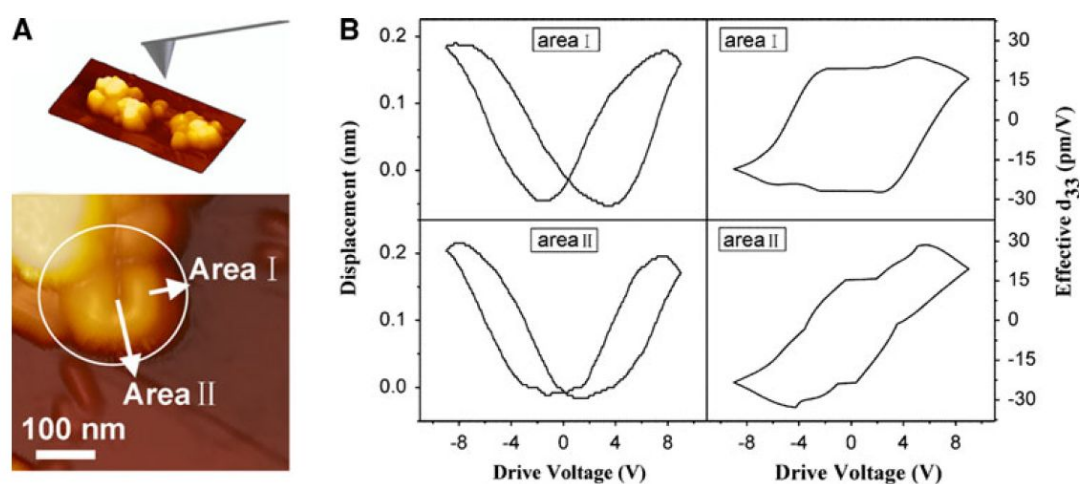


Figure 35. (A) AFM images of bowl-like BaTiO₃ nanoparticles; (B) local piezoelectric displacement-voltage loops and effective piezoelectric coefficient d_{33}^* of the bowl-like particles at the edge (area (I)) and in the central concave space (area (II)). Both areas show the characteristic butterfly loops and piezoelectric hysteresis loops. These results demonstrate that the polarization is switchable. Reproduced with permission.⁵¹ Copyright 2010, Springer.

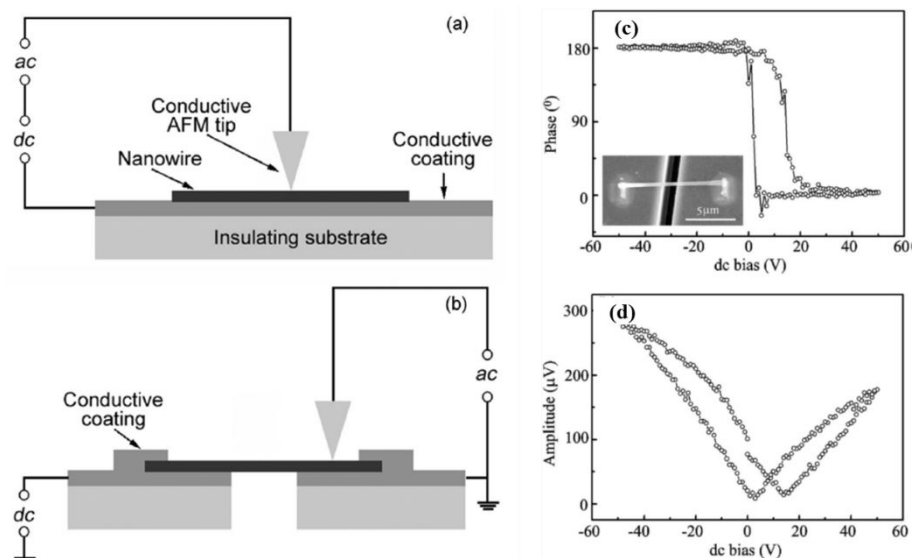


Figure 36. Schematic of the (a) biasing condition in conventional lateral PFM; (b) axial biasing setup proposed by Wang *et al*; (c) lateral PFM in-field hysteresis phase loop; (d) lateral PFM in-field hysteresis amplitude loop. Reproduced with permission.²⁰⁹ Copyright 2006, American Institute of Physics.

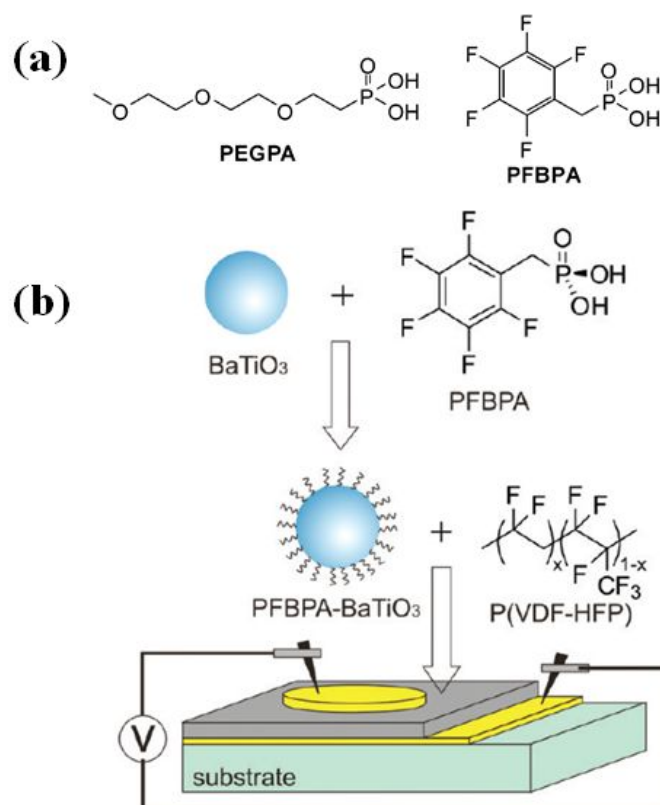


Figure 37. (a) Molecular structure of (2-[2-(2-methoxyethoxy)ethoxy]ethyl) phosphonic acid (PEGPA) and pentafluorobenzyl phosphonic acid (PFBPA) surface ligands; (b) schematic illustration of the nanocomposite fabrication process and the layout of the nanocomposite thin film capacitors. Reproduced with permission.¹⁰⁶ Copyright 2007, Wiley.

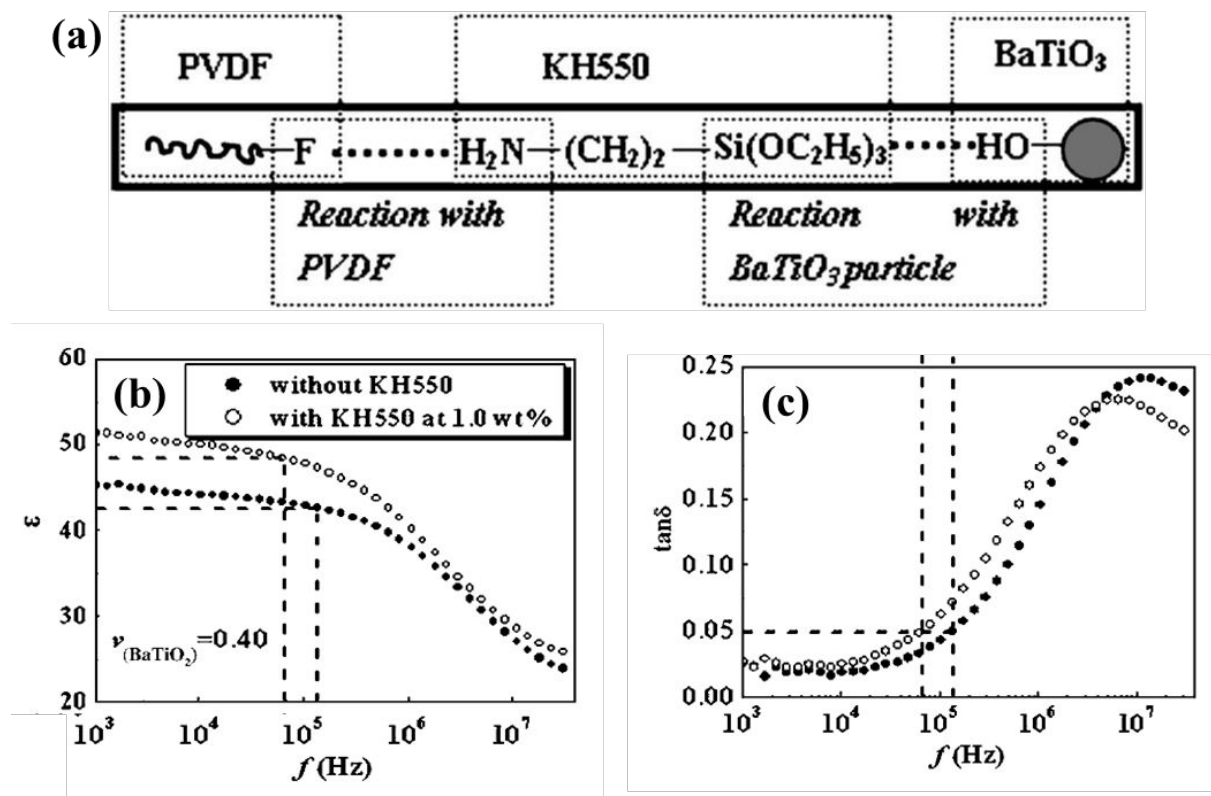


Figure 38. (a) Schematic illustration of the reaction process between KH550 and both the BaTiO₃ nanocrystal surfaces and PVDF matrix. Dependence of (b) the dielectric constant and (c) the loss tangent in the BaTiO₃/PVDF composites at 40.0 vol% BaTiO₃ on frequency at room temperature. Reproduced with permission.²¹⁹ Copyright 2006, American Institute of Physics.

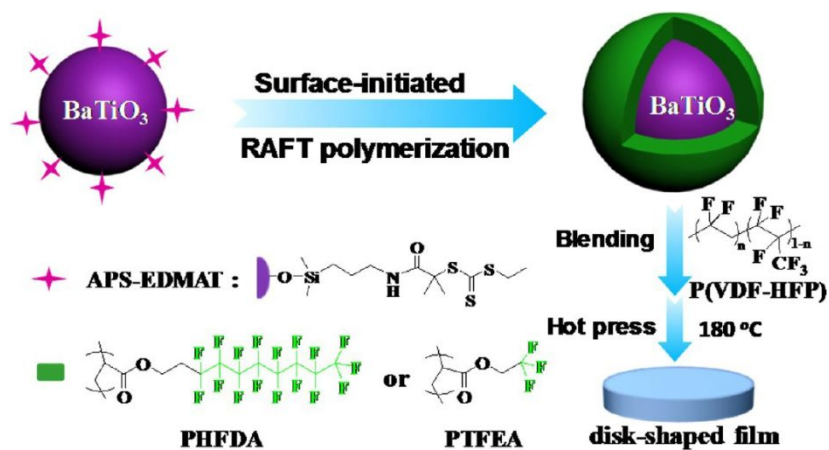


Figure 39. Schematic illustration of the preparation of fluoropolymer@BaTiO₃ core-shell nanoparticles via SI-RAFT and P(VDF-HFP) nanocomposite films via hot pressing of suspensions. Produced with permission.²²⁸ Copyright 2013, American Chemical Society.

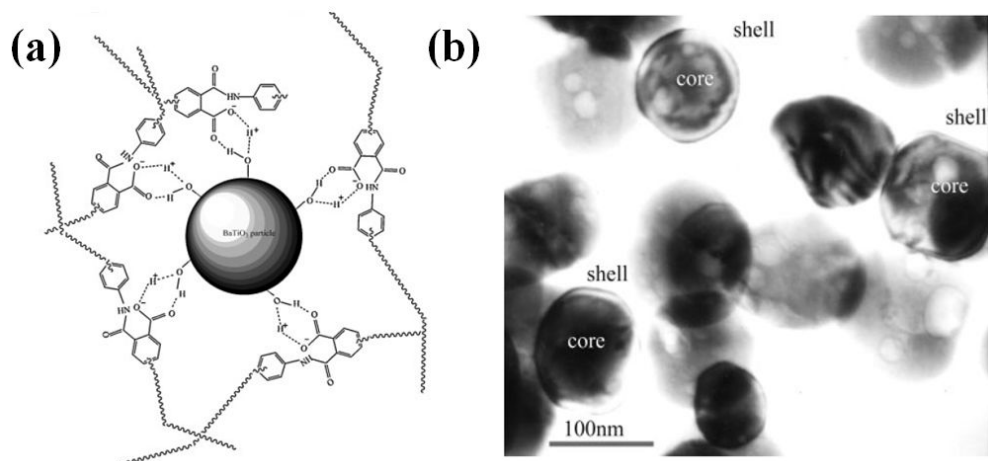


Figure 40. (a) Proposed mechanism of poly(amic acid) (PAmA) adsorption onto BaTiO₃ particles; (b) TEM image of a BaTiO₃/polyimide (PI) composite film cross-section obtained by in-situ polymerization. Reproduced with permission.²³⁵ Copyright 2008, Wiley.

References

1. D. N. Donahoe, M. Pecht, I. K. Lloyd and S. Ganesan, *Microelectron. Reliab.*, 2006, **46**, 400-408.
2. Y. Sakabe, Y. Takeshima and K. Tanaka, *J. Electroceram.*, 1999, **3**, 115-121.
3. F. Azough, R. Al-Saffar and R. Freer, *J. Eur. Ceram. Soc.*, 1998, **18**, 751-758.
4. H. J. McSkimin, *J. Acoust. Soc. Am.*, 1959, **31**, 1519-1522.
5. H. U. Kim, W. H. Lee, H. V. R. Dias and S. Priya, *IEEE Trans. Ultrason. Ferroelectr. Freq. Control*, 2009, **56**, 1555-1568.
6. G. H. Haertling, *J. Am. Ceram. Soc.*, 1999, **82**, 797-818.
7. T. F. Hueter and E. Dozois, *J. Am. Ceram. Soc.*, 1952, **24**, 85-86.
8. R. J. Meyer, R. E. Newnham, A. Amin and B. M. Kulwicki, *J. Am. Ceram. Soc.*, 2003, **86**, 934-938.
9. A. C. Dent, C. R. Bowen, R. Stevens, M. G. Cain and M. Stewart, *J. Eur. Ceram. Soc.*, 2007, **27**, 3739-3743.
10. C. M. Landis and R. M. McMeeking, *Ferroelectrics*, 2001, **255**, 13-34.
11. J. Liu, Z. J. Shen, W. L. Yao, Y. H. Zhao and A. K. Mukherjee, *Nanotechnology*, 2010, **21**.
12. P. T. Lin, Z. Liu and B. W. Wessels, *J. Opt. A: Pure Appl. Opt.*, 2009, **11**.
13. J. M. Marx, O. Eknayan, H. F. Taylor, Z. Tang and R. R. Neurgaonkar, *Appl. Phys. Lett.*, 1995, **67**, 1381-1383.
14. T. Takenaka, H. Nagata, Y. Hiruma, Y. Yoshii and K. Matumoto, *J. Electroceram.*, 2007, **19**, 259-265.
15. D. Liu and J. Y. Li, *Appl. Phys. Lett.*, 2003, **83**, 1193-1195.
16. R. Maranganti and P. Sharma, *Phys. Rev. B*, 2009, **80**.
17. J. L. Ruglovsky, J. Y. Li, K. Bhattacharya and H. A. Atwater, *Acta Mater.*, 2006, **54**, 3657-3663.
18. H. Z. Jin and J. Zhu, *J. Appl. Phys.*, 2002, **92**, 4594-4598.
19. S. Ezhilvalavan and T. Y. Tseng, *Mater. Chem. Phys.*, 2000, **65**, 227-248.
20. M. H. Yeh, Y. C. Liu, K. S. Liu, I. N. Lin, J. Y. M. Lee and H. F. Cheng, *J. Appl. Phys.*, 1993, **74**, 2143-2145.
21. D. E. Kotecki, J. D. Baniecki, H. Shen, R. B. Laibowitz, K. L. Saenger, J. J. Lian, T. M. Shaw, S. D. Athavale, C. Cabral, P. R. Duncombe, M. Gutsche, G. Kunkel, Y. J. Park, Y. Y. Wang and R. Wise, *IBM J. Res. Dev.*, 1999, **43**, 367-382.
22. A. Rasul, J. Zhang, D. Gamota, M. Singh and C. Takoudis, *Solid State Ionics*, 2010, **518**, 7024-7028.
23. Y. Jang, W. H. Lee, Y. D. Park, D. Kwak, J. H. Cho and K. Cho, *Appl. Phys. Lett.*, 2009, **94**.
24. Q. J. Cai, Y. Gan, M. B. Chan-Park, H. B. Yang, Z. S. Lu, C. M. Li, J. Guo and Z. L. Dong, *Chem. Mater.*, 2009, **21**, 3153-3161.
25. I. Salaoru and S. Paul, *J. Optoelectron. Adv. Mater.*, 2008, **10**, 3461-3464.
26. V. N. Shut, S. V. Kostomarov and A. V. Gavrilov, *Inorg. Chem.*, 2008, **44**, 905-910.
27. W. Preis and W. Sitte, *Solid State Ionics*, 2006, **177**, 3093-3098.
28. G. Ahmad, M. B. Dickerson, Y. Cai, S. E. Jones, E. M. Ernst, J. P. Vernon, M. S. Haluska, Y. Fang, J. Wang, G. Subramanyam, R. R. Naik and K. H. Sandhage, *J. Am. Ceram. Soc.*, 2008, **130**, 4-+.
29. D. S. Smith, N. Ghayoub, I. Charissou, O. Bellon, P. Abelard and A. H. Edwards, *J. Am. Ceram. Soc.*, 1998, **81**, 1789-1796.
30. G. H. Kwei, A. C. Lawson, S. J. L. Billinge and S. W. Cheong, *J Phys Chem-US*, 1993, **97**, 2368-2377.
31. W. P. Mason and B. T. Matthias, *Phys Rev*, 1948, **74**, 1622-1636.
32. J. C. Slater, *Phys Rev*, 1950, **78**, 748-761.

33. H. Takahasi, *J Phys Soc Jpn*, 1961, **16**, 1685-&.
34. J. F. Scott, *Ferroelectrics*, 2005, **316**, 13-21.
35. W. Borland and J. J. Felten, *2001 International Symposium on Microelectronics, Proceedings*, 2001, **4587**, 452-457.
36. V. K. Varadan, V. V. Varadan and K. A. Jose, *Electronics and Structures for Mems*, 1999, **3891**, 266-275.
37. K. Akamatsu, T. Tsuruoka and H. Nawafune, *J Am Chem Soc*, 2005, **127**, 1634-1635.
38. X. G. Peng, L. Manna, W. D. Yang, J. Wickham, E. Scher, A. Kadavanich and A. P. Alivisatos, *Nature*, 2000, **404**, 59-61.
39. C. B. Murray, D. J. Norris and M. G. Bawendi, *J Am Chem Soc*, 1993, **115**, 8706-8715.
40. Y. Yin and A. P. Alivisatos, *Nature*, 2005, **437**, 664-670.
41. S. H. Sun, C. B. Murray, D. Weller, L. Folks and A. Moser, *Science*, 2000, **287**, 1989-1992.
42. Q. Song and Z. J. Zhang, *J Am Chem Soc*, 2004, **126**, 6164-6168.
43. Y. W. Jun, Y. M. Huh, J. S. Choi, J. H. Lee, H. T. Song, S. Kim, S. Yoon, K. S. Kim, J. S. Shin, J. S. Suh and J. Cheon, *J Am Chem Soc*, 2005, **127**, 5732-5733.
44. M. H. Frey and D. A. Payne, *Phys. Rev. B*, 1996, **54**, 3158-3168.
45. T. M. Shaw, S. Trolrier-McKinstry and P. C. McIntyre, *Annu. Rev. Mater. Sci.*, 2000, **30**, 263-298.
46. Z. Zhao, V. Buscaglia, M. Viviani, M. T. Buscaglia, L. Mitoseriu, A. Testino, M. Nygren, M. Johnsson and P. Nanni, *Phys. Rev. B*, 2004, **70**.
47. M. P. McNeal, S. J. Jang and R. E. Newnham, *J. Appl. Phys.*, 1998, **83**, 3288-3297.
48. U. A. Joshi and J. S. Lee, *Small*, 2005, **1**, 1172-1176.
49. S. O'Brien, L. Brus and C. B. Murray, *J Am Chem Soc*, 2001, **123**, 12085-12086.
50. B. Jiang, X. Pang, B. Li and Z. Lin, *Journal of the American Chemical Society*, 2015, **137**, 11760-11767.
51. Z. Deng, Y. Dai, W. Chen, X. M. Pei and J. H. Liao, *Nanoscale Res. Lett.*, 2010, **5**, 1217-1221.
52. N. Z. Bao, L. M. Shen, A. Gupta, A. Tatarenko, G. Srinivasan and K. Yanagisawa, *Appl. Phys. Lett.*, 2009, **94**.
53. S. Adireddy, C. K. Lin, B. B. Cao, W. L. Zhou and G. Caruntu, *Chem. Mater.*, 2010, **22**, 1946-1948.
54. J. J. Urban, W. S. Yun, Q. Gu and H. Park, *J Am Chem Soc*, 2002, **124**, 1186-1187.
55. Y. B. Mao, S. Banerjee and S. S. Wong, *Chem Commun*, 2003, 408-409.
56. H. Nakano and H. Nakamura, *J. Am. Ceram. Soc.*, 2006, **89**, 1455-1457.
57. N. Nuraje, K. Su, A. Haboosheh, J. Samson, E. P. Manning, N. L. Yang and H. Matsui, *Adv. Mater.*, 2006, **18**, 807-+.
58. K. C. Huang, T. C. Huang and W. F. Hsieh, *Inorg. Chem.*, 2009, **48**, 9180-9184.
59. A. F. Demirors and A. Imhof, *Chem. Mater.*, 2009, **21**, 3002-3007.
60. R. L. Brutchey and D. E. Morse, *Angew Chem Int Edit*, 2006, **45**, 6564-6566.
61. G. A. Schneider, T. Scholz, J. Munoz-Saldana and M. V. Swain, *Appl. Phys. Lett.*, 2005, **86**.
62. F. Felten, G. A. Schneider, J. M. Saldana and S. V. Kalinin, *J. Appl. Phys.*, 2004, **96**, 563-568.
63. S. V. Kalinin and D. A. Bonnell, *Appl. Phys. Lett.*, 2001, **78**, 1116-1118.
64. J. L. Jones, *J. Electroceram.*, 2007, **19**, 67-79.
65. M. Yashima, T. Hoshina, D. Ishimura, S. Kobayashi, W. Nakamura, T. Tsurumi and S. Wada, *J. Appl. Phys.*, 2005, **98**.
66. Y. Noda, K. Akiyama, T. Shobu, Y. Kuroiwa, H. Nakao, Y. Morii and H. Yamaguchi, *Ferroelectrics*, 1998, **217**, 1-7.

67. A. Harrison, R. Ibberson, G. Robb, G. Whittaker, C. Wilson and D. Youngson, *Faraday Discuss.*, 2003, **122**, 363-379.
68. C. L. Jia and K. Urban, *Science*, 2004, **303**, 2001-2004.
69. C. L. Jia, S. B. Mi, K. Urban, I. Vrejoiu, M. Alexe and D. Hesse, *Nat. Mater.*, 2008, **7**, 57-61.
70. H. Blank and S. Amelinckx, *Appl. Phys. Lett.*, 1963, **2**, 140-142.
71. A. Schilling, T. B. Adams, R. M. Bowman, J. M. Gregg, G. Catalan and J. F. Scott, *Phys. Rev. B*, 2006, **74**.
72. C. Fang, D. X. Zhou and S. P. Gong, *Mod. Phys. Lett. B*, 2010, **24**, 2161-2170.
73. J. Petzelt, *Ferroelectrics*, 2010, **400**, 117-134.
74. Y. Dror, R. D. Levi, S. Baltianski and Y. Tsur, *J. Electrochem. Soc.*, 2006, **153**, F137-F143.
75. T. Hoshina, S. Wada, Y. Kuroiwa and T. Tsurumi, *Appl. Phys. Lett.*, 2008, **93**, -.
76. T. Tsurumi, T. Hoshina, H. Takeda, Y. Mizuno and H. Chazono, *IEEE Trans. Ultrason. Ferroelectr. Freq. Control*, 2009, **56**, 1513-1522.
77. N. Bao, L. Shen, G. Srinivasan, K. Yanagisawa and A. Gupta, *The Journal of Physical Chemistry C*, 2008, **112**, 8634-8642.
78. R. Buonsanti, V. Grillo, E. Carlino, C. Giannini, T. Kipp, R. Cingolani and P. D. Cozzoli, *Journal of the American Chemical Society*, 2008, **130**, 11223-11233.
79. K. Žagar, F. Hernandez-Ramirez, J. D. Prades, J. R. Morante, A. Rečnik and M. Čeh, *Nanotechnology*, 2011, **22**, 385501.
80. M. Teresa Buscaglia, C. Harnagea, M. Dapiaggi, V. Buscaglia, A. Pignolet and P. Nanni, *Chemistry of Materials*, 2009, **21**, 5058-5065.
81. T. W. Odom, J.-L. Huang, P. Kim and C. M. Lieber, *The Journal of Physical Chemistry B*, 2000, **104**, 2794-2809.
82. M. Bockrath, W. Liang, D. Bozovic, J. H. Hafner, C. M. Lieber, M. Tinkham and H. Park, *Science*, 2001, **291**, 283-285.
83. T. Thurn-Albrecht, J. Schotter, G. A. Kästle, N. Emley, T. Shibauchi, L. Krusin-Elbaum, K. Guarini, C. T. Black, M. T. Tuominen and T. P. Russell, *Science*, 2000, **290**, 2126-2129.
84. J. Hu, T. W. Odom and C. M. Lieber, *Accounts of Chemical Research*, 1999, **32**, 435-445.
85. Y. S. Zhao, H. Fu, A. Peng, Y. Ma, Q. Liao and J. Yao, *Accounts of Chemical Research*, 2010, **43**, 409-418.
86. J. J. Urban, J. E. Spanier, O. Y. Lian, W. S. Yun and H. Park, *Adv. Mater.*, 2003, **15**, 423-426.
87. Y. Cui and C. M. Lieber, *Science*, 2001, **291**, 851-853.
88. D. Damjanovic, *Reports on Progress in Physics*, 1998, **61**, 1267.
89. J. Hong and D. Fang, *Applied Physics Letters*, 2008, **92**, 012906.
90. Y. Huan, X. Wang, J. Fang and L. Li, *Journal of the European Ceramic Society*, 2014, **34**, 1445-1448.
91. D. McCauley, R. E. Newnham and C. A. Randall, *J. Am. Ceram. Soc.*, 1998, **81**, 979-987.
92. Y. Aikawa, Y. Iwazaki and T. Suzuki, *J. Ceram. Soc. Jpn.*, 2010, **118**, 1057-1061.
93. Y. Yang, X. H. Wang, C. K. Sun and L. T. Li, *Nanotechnology*, 2009, **20**, -.
94. A. D. Handoko and G. K. L. Goh, *Sci. Adv. Mater.*, 2010, **2**, 16-34.
95. S. Berger, *Trans. Indian Inst. Met.*, 2005, **58**, 1141-1156.
96. S. G. Lu, B. R. Li, C. L. Mak and K. H. Wong, *Int. J. Inorg. Mater.*, 2004, **19**, 1231-1239.
97. J. Kiat, C. Bogicevic, P. Gemeiner, A. Al-Zein, F. Karolak, N. Guiblin, F. Porcher, B. Hehlen, L. Yedra and S. Estradé, *Physical Review B*, 2013, **87**, 024106.

98. Z. Wang, J. Keith Nelson, H. Hillborg, S. Zhao and L. S. Schadler, *Composites Science and Technology*, 2013, **76**, 29-36.
99. R. R. Mehta, B. D. Silverman and J. T. Jacobs, *Journal of Applied Physics*, 1973, **44**, 3379-3385.
100. G. Zhang, D. Brannum, D. Dong, L. Tang, E. Allahyarov, S. Tang, K. Kodweis, J.-K. Lee and L. Zhu, *Chemistry of Materials*, 2016, **28**, 4646-4660.
101. S. V. Kalinin, C. Y. Johnson and D. A. Bonnell, *Journal of Applied Physics*, 2002, **91**, 3816-3823.
102. D. G. Popescu, M. A. Husanu, L. Trupin, L. Hrib, L. Pintilie, A. Barinov, S. Lizzit, P. Lacovig and C. M. Teodorescu, *Physical Chemistry Chemical Physics*, 2015, **17**, 509-520.
103. Y. Zhang, J. Hong, B. Liu and D. Fang, *Nanotechnology*, 2009, **21**, 015701.
104. C. W. Beier, M. A. Cuevas and R. L. Brutchey, *Langmuir*, 2010, **26**, 5067-5071.
105. J. E. Spanier, A. M. Kolpak, J. J. Urban, I. Grinberg, O. Y. Lian, W. S. Yun, A. M. Rappe and H. Park, *Nano Lett*, 2006, **6**, 735-739.
106. P. Kim, S. C. Jones, P. J. Hotchkiss, J. N. Haddock, B. Kippelen, S. R. Marder and J. W. Perry, *Adv. Mater.*, 2007, **19**, 1001-+.
107. M. B. Park and N. H. Cho, *Appl. Surf. Sci.*, 2005, **244**, 418-421.
108. F. D. Morrison, D. C. Sinclair and A. R. West, *J. Appl. Phys.*, 1999, **86**, 6355-6366.
109. H. F. Cheng, T. F. Lin, C. T. Hu and I. N. Lin, *J. Am. Ceram. Soc.*, 1993, **76**, 827-832.
110. M. T. Buscaglia, M. Bassoli and V. Buscaglia, *J. Am. Ceram. Soc.*, 2005, **88**, 2374-2379.
111. U. Manzoor and D. K. Kim, *J. Mater. Sci. Technol.*, 2007, **23**, 655-658.
112. V. V. Bhat, M. V. R. Rao and A. M. Umarji, *Mater. Res. Bull.*, 2003, **38**, 1081-1090.
113. A. Y. Fasasi, F. A. Balogun, M. K. Fasasi, P. O. Ogunleye, C. E. Mokobia and E. P. Inyang, *Sens. Actuators, A*, 2007, **135**, 598-604.
114. Z. Y. Wang, J. Hu and M. F. Yu, *Nanotechnology*, 2007, **18**.
115. A. Ianculescu, D. Berger, C. Matei, P. Budrugaec, L. Mitoseriu and E. Vasile, *J. Electroceram.*, 2010, **24**, 46-50.
116. S. O. Kang, B. H. Park and Y. I. Kim, *Cryst. Growth Des.*, 2008, **8**, 3180-3186.
117. J. Q. Qi, T. Peng, Y. M. Hu, L. Sun, Y. Wang, W. P. Chen, L. T. Li, C. W. Nan and H. L. W. Chan, *Nanoscale research letters*, 2011, **6**, 466.
118. T. Ould-Ely, M. Luger, L. Kaplan-Reinig, K. Niesz, M. Doherty and D. E. Morse, *nature protocols*, 2011, **6**, 97-104.
119. A. Testino, M. T. Buscaglia, V. Buscaglia, M. Viviani, C. Bottino and P. Nanni, *Chemistry of Materials*, 2004, **16**, 1536-1543.
120. N. T. K. Thanh, N. Maclean and S. Mahiddine, *Chemical Reviews*, 2014, **114**, 7610-7630.
121. H. Zhan, X. Yang, C. Wang, J. Chen, Y. Wen, C. Liang, H. F. Greer, M. Wu and W. Zhou, *Crystal Growth & Design*, 2012, **12**, 1247-1253.
122. V. K. LaMer and R. H. Dinegar, *Journal of the American Chemical Society*, 1950, **72**, 4847-4854.
123. S. Puri, *Phase Transitions*, 2004, **77**, 407-431.
124. W. Ostwald, *Z. Phys. Chem*, 1900, **34**, 495.
125. A. L. Rogach, D. V. Talapin, E. V. Shevchenko, A. Kornowski, M. Haase and H. Weller, *Adv Funct Mater*, 2002, **12**, 653-664.
126. D. S. Wang, T. Xie, Q. Peng, S. Y. Zhang, J. Chen and Y. D. Li, *Chem. Eur. J.*, 2008, **14**, 2507-2513.
127. M. Froba and A. Reller, *Prog. Solid State Chem.*, 1999, **27**, 1-27.
128. M. L. Steigerwald and L. E. Brus, *Accounts Chem Res*, 1990, **23**, 183-188.
129. C. D. Donega, P. Liljeroth and D. Vanmaekelbergh, *Small*, 2005, **1**, 1152-1162.

130. G. Demazeau, *C.R. Chim.*, 2009, **12**, 933-942.
131. G. Demazeau, A. Largeteau and S. Darracq, *Z. Naturforsch., B: Chem. Sci.*, 2010, **65**, 1007-1014.
132. M. Takesue, H. Hayashi and R. L. Smith, *Prog. Cryst. Growth Charact. Mater.*, 2009, **55**, 98-124.
133. S. J. Chen, X. T. Chen, Z. L. Xue, J. H. Zhou, J. Li, J. M. Hong and X. Z. You, *J. Mater. Chem.*, 2003, **13**, 1132-1135.
134. J. S. Lee and S. C. Choi, *J. Eur. Ceram. Soc.*, 2005, **25**, 3307-3314.
135. A. Cabanas and M. Poliakoff, *J. Mater. Chem.*, 2001, **11**, 1408-1416.
136. J. Libera and Y. Gogotsi, *Carbon*, 2001, **39**, 1307-1318.
137. J. O. Eckert, C. C. Hung - Houston, B. L. Gersten, M. M. Lencka and R. E. Riman, *Journal of the American Ceramic Society*, 1996, **79**, 2929-2939.
138. Y. Xie, Y. T. Qian, W. Z. Wang, S. Y. Zhang and Y. H. Zhang, *Science*, 1996, **272**, 1926-1927.
139. P. Praserthdam, M. Inoue, O. Mekasuvandumrong, W. Thanakulrangsarn and S. Phatanasri, *Inorg. Chem. Commun.*, 2000, **3**, 671-676.
140. S. Chaianansutcharit, O. Mekasuvandumrong and P. Praserthdam, *Cryst. Growth Des.*, 2006, **6**, 40-45.
141. C. H. Song, A. M. Stephan, S. K. Jeong, Y. J. Hwang, A. R. Kim and K. S. Nahm, *J. Electrochem. Soc.*, 2006, **153**, A390-A395.
142. S. Biswas, S. T. Kar and S. Chaudhuri, *Mater. Sci. Eng., B*, 2007, **142**, 69-77.
143. X. Y. Chen, L. M. Huang and Q. Z. Li, *J. Phys. Chem. B*, 1997, **101**, 8460-8467.
144. P. Justin, S. K. Meher and G. R. Rao, *J. Phys. Chem. C*, 2010, **114**, 5203-5210.
145. A. P. Moura, L. S. Cavalcante, J. C. Sczancoski, D. G. Stroppa, E. C. Paris, A. J. Ramirez, J. A. Varela and E. Longo, *Adv. Powder Technol.*, 2010, **21**, 197-202.
146. W. K. Tan, K. A. Razak, K. Ibrahim and Z. Lockman, *J. Alloys Compd.*, 2011, **509**, 820-826.
147. Z. Qin, Q. L. Liao, Y. H. Huang, L. D. Tang, X. H. Zhang and Y. Zhang, *Mater. Chem. Phys.*, 2010, **123**, 811-815.
148. J. A. Wang, M. Hojamberdiev, Y. H. Xua and J. H. Peng, *Mater. Chem. Phys.*, 2011, **125**, 82-86.
149. K. Ozeki, H. Aoki and T. Masuzawa, *Appl. Surf. Sci.*, 2010, **256**, 7027-7031.
150. K. Ding, W. E. Seyfried, N. Pester and E. Seyfried, *Geochim. Cosmochim. Acta*, 2010, **74**, A234-A234.
151. N. Sasirekha, B. Rajesh and Y.-W. Chen, *Industrial & Engineering Chemistry Research*, 2008, **47**, 1868-1875.
152. H. Hayashi, T. Noguchi, N. M. Islam, Y. Hakuta, Y. Imai and N. Ueno, *Journal of Crystal Growth*, 2010, **312**, 1968-1972.
153. X. Zhu, J. Zhu, S. Zhou, Z. Liu, N. Ming and D. Hesse, *Journal of Crystal Growth*, 2005, **283**, 553-562.
154. I. J. Clark, T. Takeuchi, N. Ohtori and D. C. Sinclair, *Journal of Materials Chemistry*, 1999, **9**, 83-91.
155. S. Wei Lu, B. I. Lee, Z. Lin Wang and W. D. Samuels, *Journal of Crystal Growth*, 2000, **219**, 269-276.
156. J.-M. Han, M.-R. Joung, J.-S. Kim, Y.-S. Lee, S. Nahm, Y.-K. Choi and J.-H. Paik, *Journal of the American Ceramic Society*, 2014, **97**, 346-349.
157. X. Wang, J. Zhuang, Q. Peng and Y. Li, *Nature*, 2005, **437**, 121-124.
158. Z. Zhou, C. C. Bowland, B. A. Patterson, M. H. Malakooti and H. A. Sodano, *ACS Applied Materials & Interfaces*, 2016, **8**, 21446-21453.
159. M. Niederberger, G. Garnweitner, N. Pinna and M. Antonietti, *J Am Chem Soc*, 2004, **126**, 9120-9126.

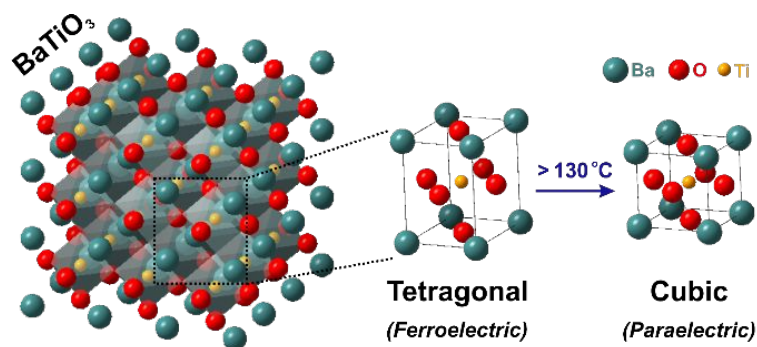
160. M. Niederberger, N. Pinna, J. Polleux and M. Antonietti, *Angew Chem Int Edit*, 2004, **43**, 2270-2273.
161. H.-W. Lee, S. Moon, C.-H. Choi and D. K. Kim, *Journal of the American Ceramic Society*, 2012, **95**, 2429-2434.
162. C. S. Chan, G. De Stasio, S. A. Welch, M. Girasole, B. H. Frazer, M. V. Nesterova, S. Fakra and J. F. Banfield, *Science*, 2004, **303**, 1656-1658.
163. A. E. Henkes and R. E. Schaak, *Inorg. Chem.*, 2008, **47**, 671-677.
164. Y. Y. Liang, M. G. Schwab, L. J. Zhi, E. Mugnaioli, U. Kolb, X. L. Feng and K. Mullen, *J Am Chem Soc*, 2010, **132**, 15030-15037.
165. F. Zhang and D. Y. Zhao, *Nano Res.*, 2009, **2**, 292-305.
166. A. Stein and R. C. Schrodin, *Curr. Opin. Solid State Mater. Sci.*, 2001, **5**, 553-564.
167. D. L. Li, H. S. Zhou and I. Honma, *Nat. Mater.*, 2004, **3**, 65-72.
168. D. H. Wang, H. M. Luo, R. Kou, M. P. Gil, S. G. Xiao, V. O. Golub, Z. Z. Yang, C. J. Brinker and Y. F. Lu, *Angew Chem Int Edit*, 2004, **43**, 6169-6173.
169. W. Y. Dong, Y. J. Sun, C. W. Lee, W. M. Hua, X. C. Lu, Y. F. Shi, S. C. Zhang, J. M. Chen and D. Y. Zhao, *J Am Chem Soc*, 2007, **129**, 13894-13904.
170. P. M. Rørvik, T. Grande and M.-A. Einarsrud, *Advanced Materials*, 2011, **23**, 4007-4034.
171. Y. Luo, I. Szafraniak, N. D. Zakharov, V. Nagarajan, M. Steinhart, R. B. Wehrspohn, J. H. Wendorff, R. Ramesh and M. Alexe, *Applied Physics Letters*, 2003, **83**, 440-442.
172. Y. Y. Chen, B. Y. Yu, J. H. Wang, R. E. Cochran and J. J. Shyue, *Inorg. Chem.*, 2009, **48**, 681-686.
173. S. J. Limmer, S. Seraji, Y. Wu, T. P. Chou, C. Nguyen and G. Z. Cao, *Advanced Functional Materials*, 2002, **12**, 59-64.
174. D. Chen, H. Zhang, R. Chen, X. Deng, J. Li, G. Zhang and L. Wang, *physica status solidi (a)*, 2012, **209**, 714-717.
175. Y. Yang, W. Xiaohui, S. Changku and L. Longtu, *Nanotechnology*, 2009, **20**, 055709.
176. Z. B. Lei, J. M. Li, Y. G. Zhang and S. M. Lu, *J. Mater. Chem.*, 2000, **10**, 2629-2631.
177. J. P. Vernon, Y. N. Fang, Y. Cai and K. H. Sandhage, *Angew. Chem. Int. Ed.*, 2010, **49**, 7765-7768.
178. N. Nuraje, X. Dang, J. Qi, M. A. Allen, Y. Lei and A. M. Belcher, *Advanced materials*, 2012, **24**, 2885-2889.
179. H. Liu, C. Hu and Z. L. Wang, *Nano Letters*, 2006, **6**, 1535-1540.
180. X. Pang, L. Zhao, W. Han, X. Xin and Z. Lin, *Nat Nano*, 2013, **8**, 426-431.
181. H. Xu, Y. Xu, X. Pang, Y. He, J. Jung, H. Xia and Z. Lin, *Science Advances*, 2015, **1**.
182. B. Li, C. Zhang, B. Jiang, W. Han and Z. Lin, *Angewandte Chemie International Edition*, 2015, **54**, 4250-4254.
183. B. Li, W. Han, B. Jiang and Z. Lin, *ACS nano*, 2014, **8**, 2936-2942.
184. B. Jiang, C. Han, B. Li, Y. He and Z. Lin, *ACS Nano*, 2016, **10**, 2728-2735.
185. M. He, X. Pang, X. Liu, B. Jiang, Y. He, H. Snaith and Z. Lin, *Angewandte Chemie*, 2016.
186. P. Setasuwon and S. Kijamnajsuk, *Smart Mater.*, 2008, **55-57**, 161-164.
187. B. Roy, S. P. Ahrenkiel and P. A. Fuierer, *J. Am. Ceram. Soc.*, 2008, **91**, 2455-2463.
188. Z. W. Song, J. F. Ma, H. Y. Sun, W. Wang, Y. Sun, L. J. Sun, Z. S. Liu and C. Gao, *Ceram. Int.*, 2009, **35**, 2675-2678.
189. Y. B. Mao, S. Banerjee and S. S. Wong, *J Am Chem Soc*, 2003, **125**, 15718-15719.
190. H. Deng, Y. C. Qiu and S. H. Yang, *J. Mater. Chem.*, 2009, **19**, 976-982.
191. I. U. Arachchige and S. L. Brock, *Accounts Chem Res*, 2007, **40**, 801-809.
192. M. Niederberger, *Accounts Chem Res*, 2007, **40**, 793-800.
193. S. C. Padmanabhan, S. C. Pillai, J. Colreavy, S. Balakrishnan, D. E. McCormack, T. S. Perova, Y. Gun'ko, S. J. Hinder and J. M. Kelly, *Chem. Mater.*, 2007, **19**, 4474-4481.

194. M. Veith, S. Mathur, N. Lecerf, V. Huch, T. Decker, H. P. Beck, W. Eiser and R. Haberkorn, *Journal of Sol-Gel Science and Technology*, 2000, **17**, 145-158.
195. M. C. Gust, N. D. Evans, L. A. Momoda and M. L. Mecartney, *Journal of the American Ceramic Society*, 1997, **80**, 2828-2836.
196. M. Kamalasanan, N. D. Kumar and S. Chandra, *Journal of applied physics*, 1994, **76**, 4603-4609.
197. M. Kamalasanan, N. D. Kumar and S. Chandra, *Journal of applied physics*, 1993, **74**, 5679-5686.
198. S. Liu, L. Huang, W. Li, X. Liu, S. Jing, J. Li and S. O'Brien, *Nanoscale*, 2015, **7**, 11766-11776.
199. Y. Hao, X. Wang, J. Kim and L. Li, *Journal of the American Ceramic Society*, 2014, **97**, 3434-3441.
200. F. A. Rabuffetti and R. L. Brutchey, *Journal of the American Chemical Society*, 2012, **134**, 9475-9487.
201. B. A. Hernandez, K. S. Chang, E. R. Fisher and P. K. Dorhout, *Chem. Mater.*, 2002, **14**, 480-482.
202. C. Ahn, K. Rabe and J.-M. Triscone, *Science*, 2004, **303**, 488-491.
203. K. Terabe, M. Nakamura, S. Takekawa, K. Kitamura, S. Higuchi, Y. Gotoh and Y. Cho, *Applied physics letters*, 2003, **82**, 433-435.
204. A. Gruverman and S. V. Kalinin, *J. Mater. Sci.*, 2006, **41**, 107-116.
205. J. Munoz-Saldana, M. J. Hoffmann and G. A. Schneider, *J. Mater. Chem.*, 2003, **18**, 1777-1786.
206. W. S. Yun, J. J. Urban, Q. Gu and H. Park, *Nano Lett*, 2002, **2**, 447-450.
207. S. Ray, Y. V. Kolen'ko, D. Fu, R. Gallage, N. Sakamoto, T. Watanabe, M. Yoshimura and M. Itoh, *Small*, 2006, **2**, 1427-1431.
208. C.-V. Cojocar, C. Harnagea, F. Rosei, A. Pignolet, M. A. F. Van den Boogaart and J. Brugger, *Applied Physics Letters*, 2005, **86**, 183107-183107-183103.
209. Z. Y. Wang, A. P. Suryavanshi and M. F. Yu, *Appl. Phys. Lett.*, 2006, **89**, -.
210. V. K. Thakur and R. K. Gupta, *Chemical reviews*, 2016, **116**, 4260-4317.
211. Z.-M. Dang, J.-K. Yuan, J.-W. Zha, T. Zhou, S.-T. Li and G.-H. Hu, *Progress in Materials Science*, 2012, **57**, 660-723.
212. E. Tuncer, S. M. Gubański and B. Nettelblad, *Journal of Applied Physics*, 2001, **89**, 8092-8100.
213. Z.-M. Dang, Y. Shen and C.-W. Nan, *Applied Physics Letters*, 2002, **81**, 4814-4816.
214. W. Lü, J. Dong and Z.-Y. Li, *Physical Review B*, 2000, **63**, 033401.
215. Y. Kobayashi, T. Tanase, T. Tabata, T. Miwa and M. Konno, *J. Eur. Ceram. Soc.*, 2008, **28**, 117-122.
216. P. Barber, S. Balasubramanian, Y. Anguchamy, S. Gong, A. Wibowo, H. Gao, H. J. Ploehn and H.-C. Zur Loye, *Materials*, 2009, **2**, 1697-1733.
217. J. J. Li, J. Claude, L. E. Norena-Franco, S. Il Seok and Q. Wang, *Chem. Mater.*, 2008, **20**, 6304-6306.
218. S. S. Tripathy and A. M. Raichur, *J Disper Sci Technol*, 2008, **29**, 230-239.
219. Z. M. Dang, H. Y. Wang and H. P. Xu, *Appl. Phys. Lett.*, 2006, **89**, -.
220. Z. M. Dang, J. K. Yuan, S. H. Yao and R. J. Liao, *Advanced Materials*, 2013, **25**, 6334-6365.
221. Z. Pan, L. Yao, J. Zhai, B. Shen and H. Wang, *Composites Science and Technology*, 2017, **147**, 30-38.
222. D. Kang, G. Wang, Y. Huang, P. Jiang and X. Huang, *ACS Applied Materials & Interfaces*, 2018, **10**, 4077-4085.
223. D. He, Y. Wang, X. Chen and Y. Deng, *Composites Part A: Applied Science and Manufacturing*, 2017, **93**, 137-143.

224. Z. Pan, L. Yao, J. Zhai, D. Fu, B. Shen and H. Wang, *ACS Applied Materials & Interfaces*, 2017, **9**, 4024-4033.
225. Y. Xie, Y. Yu, Y. Feng, W. Jiang and Z. Zhang, *ACS Applied Materials & Interfaces*, 2017, **9**, 2995-3005.
226. H. M. Jung, J. H. Kang, S. Y. Yang, J. C. Won and Y. S. Kim, *Chem. Mater.*, 2010, **22**, 450-456.
227. C. A. Grabowski, S. P. Fillery, H. Koerner, M. Tchoul, L. Drummy, C. W. Beier, R. L. Brutchey, M. F. Durstock and R. A. Vaia, *Nanocomposites*, 2016, **2**, 117-124.
228. K. Yang, X. Huang, Y. Huang, L. Xie and P. Jiang, *Chemistry of Materials*, 2013, **25**, 2327-2338.
229. Z. Li, L. A. Fredin, P. Tewari, S. A. DiBenedetto, M. T. Lanagan, M. A. Ratner and T. J. Marks, *Chemistry of Materials*, 2010, **22**, 5154-5164.
230. P. Kim, N. M. Doss, J. P. Tillotson, P. J. Hotchkiss, M. J. Pan, S. R. Marder, J. Y. Li, J. P. Calame and J. W. Perry, *Acs Nano*, 2009, **3**, 2581-2592.
231. R. Popielarz, C. K. Chiang, R. Nozaki and J. Obrzut, *Macromolecules*, 2001, **34**, 5910-5915.
232. A. Biswas, I. S. Bayer, P. C. Karulkar, A. Tripathi, D. K. Avasthi, M. G. Norton and J. B. Szczech, *Appl. Phys. Lett.*, 2007, **91**.
233. L. X. Gao, Q. P. Liu, Z. W. Gao and Y. Lin, *Polym. Compos.*, 2008, **29**, 1160-1164.
234. X. L. Dou, X. L. Liu, Y. Zhang, H. Feng, J. F. Chen and S. Du, *Appl. Phys. Lett.*, 2009, **95**.
235. Z. M. Dang, Y. Q. Lin, H. P. Xu, C. Y. Shi, S. T. Li and J. B. Bai, *Adv. Func. Mater.*, 2008, **18**, 1509-1517.
236. J. F. Scott, *Ferroelectrics*, 1998, **206**, 365-379.
237. J. T. Hu, T. W. Odom and C. M. Lieber, *Accounts Chem Res*, 1999, **32**, 435-445.
238. M. Ethayaraja and R. Bandyopadhyaya, *Langmuir*, 2007, **23**, 6418-6423.
239. R. L. Penn and J. F. Banfield, *Science*, 1998, **281**, 969-971.
240. J. Li, X. Hong, D. Li, K. Zhao, L. Wang, H. Z. Wang, Z. L. Du, J. H. Li, Y. B. Bai and T. J. Li, *Chem Commun*, 2004, 1740-1741.
241. F. D. Wang, A. G. Dong, J. W. Sun, R. Tang, H. Yu and W. E. Buhro, *Inorg. Chem.*, 2006, **45**, 7511-7521.
242. M. Kuno, *Phys. Chem. Chem. Phys.*, 2008, **10**, 620-639.
243. B. Q. Sun, E. Marx and N. C. Greenham, *Nano Letters*, 2003, **3**, 961-963.
244. I. Gur, N. A. Fromer and A. P. Alivisatos, *J. Phys. Chem. B*, 2006, **110**, 25543-25546.
245. Y. W. Jun, H. W. Chung, J. T. Jang and J. Cheon, *J. Mater. Chem.*, 2011, **21**, 10283-10286.
246. T. Kudernac, S. B. Lei, J. Elemans and S. De Feyter, *Chem. Soc. Rev.*, 2009, **38**, 402-421.
247. J. Kim and K. B. Song, *Micron*, 2007, **38**, 409-426.
248. J. Loos, *Adv. Mater.*, 2005, **17**, 1821-1833.
249. M. S. Dresselhaus, G. Dresselhaus, R. Saito and A. Jorio, *Phys. Rep.*, 2005, **409**, 47-99.
250. M. Liess, S. Jeglinski, Z. V. Vardeny, M. Ozaki, K. Yoshino, Y. Ding and T. Barton, *Phys. Rev. B*, 1997, **56**, 15712-15724.
251. Z. Q. Tian and B. Ren, *Annu. Rev. Phys. Chem.*, 2004, **55**, 197-229.
252. V. Myroshnychenko, J. Rodriguez-Fernandez, I. Pastoriza-Santos, A. M. Funston, C. Novo, P. Mulvaney, L. M. Liz-Marzan and F. J. G. de Abajo, *Chem. Soc. Rev.*, 2008, **37**, 1792-1805.
253. M. K. Miller and R. G. Forbes, *Mater. Charact.*, 2009, **60**, 461-469.
254. T. F. Kelly and M. K. Miller, *Rev. Sci. Instrum.*, 2007, **78**.

255. S. V. Kalinin, A. N. Morozovska, L. Q. Chen and B. J. Rodriguez, *Rep. Prog. Phys.*, 2010, **73**.
256. X. H. Ji, D. Copenhaver, C. Sigmeller and X. G. Peng, *J Am Chem Soc*, 2008, **130**, 5726-5735.
257. S. Hong, J. Woo, H. Shin, J. U. Jeon, Y. E. Pak, E. L. Colla, N. Setter, E. Kim and K. No, *Journal of Applied Physics*, 2001, **89**, 1377-1386.

Table of Content



The ferroelectric material barium titanate (BaTiO_3) has garnered considerable attention over the past decade because it exhibits both excellent dielectric and ferroelectric properties. The successful production of nanostructured BaTiO_3 enables theoretical and experimental studies into the intriguing yet complex dielectric properties of individual BaTiO_3 NCs (*i.e.*, size, surface defects and capping ligands, etc.). By combining BaTiO_3 nanocrystals and certain polymers, the resulting BaTiO_3 /polymer nanocomposites possess many advantages from both components; such as simple solution processibility, high breakdown strength and light weight afforded by the polymer component, and a high dielectric constant afforded by the BaTiO_3 component.

20-word summary:

This review introduces the fundamentals of nanostructured BaTiO_3 and summarizes various synthetic methods for producing BaTiO_3 nanocrystals with controlled properties for ferroelectric and dielectric applications.